ABSTRACT

Title of Dissertation: INVESTIGATION OF LOW TEMPERATURE CREEP DEFORMATION BEHAVIOR OF A METASTABLE BETA TITANIUM 14.8WT% VANADIUM ALLOY

Candi Monica Hudson, Doctor of Philosophy, 2004

Dissertation Directed by: Associate Professor Sreeramamurthy Ankem
Department of Materials Science and Engineering

This dissertation presents the results of investigated low temperature creep behavior of a metastable beta phase Ti-14.8Weight%V alloy (Ti-14.8V). It is the first such study which relates the activation energy and microstructure with low temperature creep deformation mechanisms in the temperature range of 298K to 800K. A Ti-14.8V alloy with a grain size of 350 μm was tensile and creep tested in the temperature range of 298 - 458 K; creep tests were conducted at 95% of the 0.2% yield stress. Activation energies were determined by utilizing strain rate models and resulting least squared Arrhenius plots, which were found to be in the range of 36.6-112.42 kJ/mole for the measured temperature range of 298 - 458K. The resulting activation energies plotted as a function of strain was found to be linear dependent. The determined activation energy values of 36.6 – 57.55

kJ/mole at the low end of the strain are within the range of activation energy values for dislocation motion. The higher activation energy value of 112.42 kJ/mole is within range of for activation energy value for diffusion of oxygen in beta titanium alloy. These activation energy values are consistent with SEM and TEM observations of deformation mechanisms as dislocations, slip, and stress induced plates (SIP) in the form of twinning were the dominant creep deformation mechanisms for this alloy. The deformation mechanisms changed from predominantly slip to SIP in the form of twins at the higher test temperatures. Further, these findings are consistent with observations, characterization by TEM analysis identified slip dislocations of the 1/2<111> type and twins of the {332}<113> type, which are consistent with time dependent twinning deformation. The results strongly support the mechanism of oxygen controlled time dependent twinning deformation as proposed earlier.

INVESTIGATION OF LOW TEMPERATURE CREEP DEFORMATION BEHAVIOR OF A METASTABLE BETA TITANIUM – 14.8WT%VANADIUM ALLOY

by

Candi Monica Hudson

Dissertation submitted to the Faculty of the Graduate School of the
University of Maryland, College Park in partial fulfillment
of the requirements for the degree of
Doctor of Philosophy

Advisory Committee:

Associate Professor Sreeramamurthy Ankem, Chair/Advisor
Associate Professor Mohamad Al-Sheikhly
Professor Aris Christou
Professor Lourdes Salamanca-Riba
Associate Professor Evanghelos Zafiriou

DEDICATION

I dedicate this dissertation to my mother, Darlene Joyce-Stewart-Hudson for her undying love, strong faith, tremendous strength, fervent prayers, the many sacrifices she made for me so I could pursue my dream, for always believing in me and most important for never accepting the word **NO**. Mommie you stayed with me even to the end of your last days here on earth supporting me, inspiring me, and constantly encouraging me to complete my goal. You always believed in me in spite of what the world said about me or did to me. I am ever so thankful that the Lord blessed me with an amazing woman with much class, dignity and strength for a mother. I will always remember you and I miss you terribly. Even though you are not here physically I know that you can still see me and that you are always with me in spirit. Je suis une meillure femme parce-que vous Maman, toujours votre fille, ta belle, Candi.

ACKNOWLEDGMENTS

Pursuit of this degree did not come easy for me, nor did it come quickly, hard to believe that over a decade has passed since I first began this endeavor. This journey has truly been a testament of my faith; I have been challenged in every way possible and imaginable, physically, mentally, emotionally, and spiritually. I have lost the most precious being to me on this earth during this pursuit and I will always cherish the times I had with my mother during my journey. Even though my mother was no longer with my physically towards the end, I know that she is still with me spiritually. Thank you Mommie.

I take this moment to thank God, the Lord, my saviour and salvation for providing me with this opportunity and seeing me through to the very end of this chapter of my life. There are many people that I have to thank and I am most appreciative that the Lord has brought these people in my path during my walk with God in the pursuit of this degree. I often heard that a person's character and accomplishments is an indication of the people behind them. I could not have completed my goal without their assistance, support, guidance, leadership, and belief in me. Furthermore, I am very thankful to the strong, spiritual, wise people who stand behind me and allowed me to stand on their shoulders.

I would like to especially thank the funding agencies for making pursuit of this research possible; Dr. K.L. Murty and the National Science Foundation for funding this research under award number DMR-0102320; as well as Dr. Francis J. Montegani, and NASA for funding this research under the NASA Graduate Student Researchers Program (GSRP) award number NGT3-52367.

University of Maryland – Maryland/DC

I honestly would have to say it is when I came to Maryland that I completely grew up. My experiences at the University of Maryland – College Park has prepared me for the world in so many ways, even my mother admitted to this fact as well. These experiences gave me much strength during my mother's last days; and provided me the insight to look at both science and life in a new perspective.

Dr. Ankem, thank you for being my advisor and "shepherding me to the completion of this degree." Some children don't appreciate what their parents teach them until they have children of their own; in my case I appreciate what my advisor has taught me now. Thank you. You demanded my best and that I pursue and follow through in my scientific research endeavors on my own; because of this, I am a far better scientist and engineer than I was before I came to Maryland, I can now stand on my own, because of this, I thank you. I would like to personally thank each of my committee members for always being available, their patience with me, answering my questions when I finally admitted that I needed help (in addition to my advisor) as well as their mentorship and guidance and providing me a strong example to follow: Dr. Mohamad Al-Sheikhly, Dr. Aris Christou, Dr. Lourdes Salamanca-Riba, and Dr. Evanghelos Zafiriou. I would like to also thank Dr. Carol Smidts for always keeping her door open, her wisdom and always having the right words. Dr. Yvonne D. Oslin, for being there in ways I could not imagine. Thank you for having my back when others would not!! Thanks for helping me come into my own as well as helping me grow in areas that I did not even know existed!! Ahmaad Nurriddin you have been a part of my graduate career ever since the beginning

and have been instrumental in both my personal and professional growth; thank you for your patience, wisdom and guidance during this journey. Julie Banner for being a wonderful mirror, mentor, friend, spending precious time with me, and helping me see through so many difficult situations that seemed so impossible. I would also like to thank Pamela A. Crockett, Esq. for helping me throughout my higher education career and assisting me during my journey at Maryland. Pam, I thank you for sharing your joy with me even though I had much sorrow with the loss of my mother. You have been with me ever since I first pursued my bachelor's, thanks for sticking by me and believing me. Chinmay Gowardhan and Alan Jaworski for being amazing fellow graduate students and their assistance, I am sincerely thankful. Julie Banner for being a wonderful mentor, friend and mirror, which enabled me to see through so many situations that appeared to be so bleak. Thank you for taking time out of your busy schedule to assist me. I am truly thankful. Mr. Tim Zhang, I will always cherish your coming to my rescue whenever the filament was burnt in the SEM and performing miracles with the TEM. I know now it is best to work when one is well rested, a hard lesson I had to learn, thank you for understanding me. Haimei Zheng, for the time spent, the scientific discussions, I have learned much about life during my time with both you and Tim and I became a microscopist who could stand on her own because of you. Mr. Thomas C. Loughran, you have stood by me without question and have been there with me and for me. Thank you for being by my side during my mother's last days here on this earth; for constantly calling me and never letting me quit.

My Chicago Family

Chicago is where I was born and raised and has help plant the seeds of who I am and who I have become. As I look to my home, my birthplace I am in awe of so many people who have also spent their childhood, developed their careers and made a difference in this world all from my "Sweet Home Chicago." I also like to thank those people who have inspired me who have come from Chicago, Dr. Mae Jemison, Dr. Percy L. Julian, Dr. Reggie Jones (a remarkable man who has honed my scientific skills for a kid and thank you so much for the Chicago Area Health and Medical Careers Program), Dr. Mildred "Millie" Dresselhaus, Dr. Richard Smalley (whom I thank as well as his post-docs for teaching me how to effectively purify nanotubes and a University of Chicago alum), the City of Chicago Police Department which continues to be a part of my career and support, the Chicago Park District, and the University of Chicago Laboratory Schools.

Dr. Reggie Jones "Pops" thank you for coming to my rescue; and making it possible for me to continue the pursuit and complete my doctorate you are truly the "Godfather!" You even helped me pick up the pieces when my mother passed, thank you Pops. Janet Grange, Esq. you have been the epitome of a mentor, a friend, and an example to emulate thank you for everything. I cannot thank you enough for being there since I was a kid, helping Mommie and I, and even more for helping see that there was a purpose to finishing even though Mommie is no longer here with me on earth. I thank you for always being available for me any time of day or night. I thank the Millers for being there every way possible and imaginable; words cannot express my gratitude. You have known me ever since I was a little girl and you have shaped me into the

woman I am today and stood by me during my journey, thank you. Fr. Anthony Vader for your profound wisdom, prayers and baptizing me. Fr. Gerald O'Reilly, you sent my Mommie home with dignity, grace, and class; and I thank the Lord for having someone like you in my path. You knew my beloved Uncle Vic/Fr. Victor Edward Stewart so you truly understood me in more ways imaginable. Thank you for your prayers, and being with me as I tried to pick up the pieces. Jonathan Lackland, you are truly my friend in deed. You have been there with me since we were teenagers, bright eyed at the world. I cannot thank you enough for always being there at any time of the day or night, for answering my calls and being there with me when it was MOST important, AFTER my mother was buried and helping me pick myself back up when the phone stopped ringing; I cannot thank you enough! Robert Lindsey, you stood by me all along ever since Bradley, thanks for the prayers, constant encouragement when I needed it and the kicks also! Carolyn Wyatt, hard to believe that so many years has passed since we were suitemates back at Bradley. Thanks for believing in me when I was at Bradley, and for believing in me now. Even more, thanks for being there when I really needed a friend and support without any strings or conditions. My mom trusted your friendship was sincere and true and I thank you for being my friend. I am even more appreciative to your friendship as you are STILL there for me after my mom is gone and are THERE for me when I am unable to take care of myself!! YOU ARE TRULY A FRIEND INDEED!! Thank you!! Monte Webb, thank you for your constant encouragement, many late night phone calls and belief in me. Charles and Lisa Hill, you were there when I first endeavored on this journey and before this journey even began. You knew me when I was a little Lab School girl and continued to remind me that I was indeed

groomed for this and that I am a Labbie. Thank you for your constant encouragement, love and being there during Mommie's last days. Myrtle Jones, I value your friendship and most appreciative for it. I am truly amazed how you were there for me during my loss of my mother and even more amazed that you have been there for me even more afterwards. Thank you for continuing to encourage me and reminding me to be the person that I am and the woman my mother wanted me to be. Dee Dee Hearns-Thomas, it is most disheartening that it took the death of my mother to bring you back into my life. I do not question why or how you have come back into my life, but I thank the Lord that we are reunited. We grew up together and you know me even better than I know myself at times. You have kicked me just like my Mommie would do and made me pick myself backup; yet at the same time, you give me love just like she would do when I needed it. Thank you for allowing me to lean on you when I was so tired. Even more, thank you for continuing to kick me in the end so I could finish as my mother would have wanted. Mr. Sanford Patlak, Dr. David MacGill, Ms. Hanna Goldschmidt and the faculty of the University of Chicago Laboratory Schools; you have molded me and shaped me into the intellectual I am today from the very beginning. It is because of that foundation I refuse to listen to the negative words I encountered during my journey because I learned being a "Labbie" that I could do!! Thank you!! Lab is the one place I am not afraid to show my true stuff!! Patlak, I would like to thank you being there during every SINGLE dark time of my life including my most recent, as well as thank you for being there during the happy times!!

My Cleveland Family

Judy Montford, for making it possible for me to continue the pursuit of my dream. Robert Lawrence, I learned so much from you; thank you for reminding me of the most important thing in life, faith.

My New England Family

Dr. Sheila Browne, our lives has paralleled in so many ways that are unbelievable. I thank the Lord for placing you in my path during my journey. You helped me find my way and supported me in my decisions without judgment. I thank you for helping me and enabling me to continue my pursuit of my degree. My mother is not here to thank you in person, I thank you on her behalf. God Bless you Sheila. Maronda Brown, it was a miracle that we met and I thank the Lord that our paths crossed. Thank you for standing by me throughout my journey. Lise Kaye and Dr. Joane Reed of the Harvard Biomedical Science Careers Program for providing me the much needed encouragement when I was knocked down.

My Texas Family

Strange that I never envisioned beginning my graduate studies in Texas, but somehow the Lord brought me there. I am most thankful that the Lord ordered my steps to Texas because that was where I gained strength, learned about myself and met the most beautiful people in my life who became my family and captured my heart. Every single one of you took me into your lives and welcomed me with open arms and continued to remain a positive force in my life, you continued to encourage me and support me even when I did not expect it and was there for me during my most recent darkest hour.

Dr. Houshang Masudi for your constant calls, continuous encouragement, amazing insight to situations and you would never let me quit. You were the first true mentor and friend I had in my graduate career and did a marvelous job in guiding me throughout this long haul. Thank you for providing me with a solid foundation. Dr. Marie Pontier-Johnson thank you for being there every single time I have called without any questions. You understood me when the world did not and allowed me to be the French girl that I was raised to be, and helped me to become the French woman my Mommie would have wanted me to be. You guided me and helped me to hone skills that I had, as well as acquire many more scientific skills and become an effective researcher which provided me the strong foundation for when I moved on to Maryland; thank you ma chere Marie. Jiles P. Daniels, Jr. I am most appreciative for your mentorship, patience, and being there during my mother's last days and even more, being there after she was gone. Thank you for kicking me back up so I could finish and face many unknowns, as well as for assisting me in understanding the seen and unseen. I cannot thank you enough for being there as I worked hard to grow over the years and for still being there by my side when so many have walked away wanting to see the finished product first. You have been there during both the struggle and the glory, thank you; even more thank you for believing in me when others did not! Dr. Fred Ling thank you for your sincere encouragement and letting me know that there are always options. Valeria C. Mitchell, wow, all I can say is thank you for being there after I surfaced again. You were there when I was an undergrad and was the first black female ME I ever met! I looked up to you when I was an undergrad and I still do now!! The Lord has blessed me to have you both in my life back in

Illinois and in Texas and thanks for welcoming back to your home in TX!! Trena Key for being so comforting as I was growing and always making sure that I look fabulous!! Thank you for your support and listening to me whine as you worked hard to make me look fabulous!! I love you and Val so dearly!! Paola Guerra, I still enjoy the spice of life and not ashamed of it thanks to you!! Thank you for welcoming to TX and back into your life!!

My European Family

Dr. Dave Wheeler, strange that we began our doctoral pursuit at the same time; it me longer than we planned. Thanks for continuing to encourage me and the many phone calls even while you were pursuing your doctorate at the University of South Hampton. I'm sorry that it took me longer than we planned. If I survive my next life challenge I will visit you personally in the UK!!

My Applied Physics Laboratory/ Johns Hopkins University Family

While I realize that I have said many clichés in my acknowledgments, there are many truths to them and are most appropriate for me. It has often been said, "that when the pupil is ready, the teacher will appear." Thank you for being my teacher and supporting me both professionally and academically. I am most appreciative to your support during the death of my mother as well as refusing to allow me to walk away. I could not have completed this journey without your help and support, thank you. I would like to take this moment to thank the inspirational people I have come to know at APL. Dr. David VanWie, you have shown me a strong example of a leader, I am most appreciative of your guidance and wisdom, and I most honored to be your fellow Maryland alum. Dale E. Clemons, P.E., I am most appreciative to your leadership, and keen

insight, the professional example you have shown me, thank you for your patience, support and encouragement. Dr. Joe Suter and Dr. John Sommerer for staying on me constantly. Dr. Dennis Nagle, I am amazed at watching science in action whenever I am near you; I have learned so much from you about both science and life. Dr. John Brupbacher, I deeply respect your diligence and dedication to science. Dr. Glen Gaddy, who have shown me that it's okay to be yourself in the name of science; and don't be afraid to write acknowledgements from the heart. Dr. Victor McCrary, amazing that our paths would cross at APL, thank you for kicking me. Lois Archibald, strange that I had to come all the way to Maryland to meet someone from Peoria who truly understands the solid foundation I gained from Bradley. Thank you for your wisdom, guidance and encouragement. Dr. James E. West, you are by no means last. I am most honored that a National Academy member made time for me on many occasions to assist me with the writing of my dissertation. I am also appreciative of the challenging scientific discussions we had about TEM's, charges, dipole moments and Curie temperature. I now see why the Curie-Weiss law is so important. Thank you for your support and showing me that a person who has accomplished so much in his life can also be humble.

They say that the struggles and adversities one experiences in life is an opportunity to grow, I have grown tremendously from this experience. Even more, I am much stronger, I have learned patience, humility and restored my faith during my pursuit.

To Whom Much is given, much is required.

I can do all things through Christ, which strengthens me. Phillipians 1:14.

TABLE OF CONTENTS

LIST OF ABBREVIATIONS AND SYMBOLS

α	Alpha phase
$\alpha + \beta$	Alpha plus beta phase
β	Beta phase
β'	Beta prime decomposition phase
β_c	Minimum critical point for beta stabilizing content
β_s	Beta phase stability point
α	Alpha phase
β	Beta phase of titanium
Δ	Delta, change
ε	Strain
$\dot{\varepsilon}$	Strain Rate
γ	Stacking fault energy
ρ	Density
π	Pi
σ	Stress
ω	Metastable omega phase
a	Sometimes used as creep exponent in the creep power law equation
A	Constant term in creep power law equation, creep constant, also units for Amperes (current)
A/D	Analog/Digital
Al	Aluminum
Ar	Argon
ATS	Applied Test Systems
b	Burgers vector
BCC	Body centered cubic
BCT	Body centered tetragonal
C	Coulombs
Cr	Chromium
Cu	Copper
d	grain size
EDM	Electron Discharge Machining
Fe	Iron
H	Hydrogen
HCP	Hexagonal close packed
i	Beam Current
kV	kilovolts (10^3)
K	Strength Parameter
lb	pound
lb/in^2	pounds per square inch
LVC	Linear Voltage Capacitor
m	Hollomon Constant for strain rate sensitivity
mm	millimeter(s), 10^{-3} meters
μm	micron(s), 10^{-6} meters
M	Magnification Setting
Mg	Magnesium

Mn	Manganese
Mo	Molybdenum
MoE	Molybdenum Equivalency
MPa	Megapascals
MRF	Materials Research Furnace
ms	millisecond, 10^{-3} seconds
M_s	Martensite start temperature
n	Hollomon Constant for strain hardening exponent
n	Time exponent in creep power law equation
Nb	Niobium
Ni	Nickel
nm	nanometers, 10^{-9} meters
Q	Activation energy
RMI	Reactive Metals Incorporated
s	Second
SAD	Selected Area Diffraction
SEM	Scanning Electron Microscopy
SIP	Stress Induced Plate
SPM	Scanning Probe Microscope
TEM	Transmission Electron Microscopy
Ti	Titanium
Ti-9.4Mn	Titanium + 9.4 weight percent manganese alloy
Ti-14.8V	Titanium + 14.8 weight percent vanadium alloy
T_m	Melt Temperature
V	Vanadium
Wt	Weight
XRD	X-ray Diffraction
YS	Yield Stress, Yield Strength
Zr	Zirconium

LIST OF TABLES

LIST OF FIGURES

CHAPTER 1

INTRODUCTION

Background and Research Need

Beta titanium (β Ti) alloys are used in several applications including those where low temperature creep deformation behavior is important; some of these applications include: aerospace/aeronautical (aircraft landing gear), automotive (springs), biomedical (hip & joint implants, prosthesis), computer, geothermal – oil exploration (structural piping components), power generation (storage tanks), just to outline several [1-6]. In many of these applications, components are subjected to continuous loading over extended time periods at low temperatures (in the range of 298 K to 800K) and therefore require materials with ideal low temperature creep resistant properties for long term, reliable service. Processing conditions, alloy composition and microstructure are all factors that affect the low temperature creep behavior of beta titanium alloys, and therefore significantly impact the resulting component performance.

Ambient temperature creep deformation mechanisms of beta titanium alloys include: slip, twinning, slip accompanied by twinning and twinning consisting of stress induced plates (SIP) in the form of ω phase particles. Activation energies of these mechanisms, which identify the rate-determining step, i.e., the mechanisms most responsible for creep deformation have not been determined for Ti-14.8weight%Vanadium (Ti-14.8V) alloy. Fundamental understanding of the low temperature creep deformation mechanisms is

essential to the design of new alloys and optimization of current existing alloys microstructure.

β Titanium Creep Deformation Behavior

Numerous ambient temperature creep studies on β Ti alloys have shown that microstructure is a significant variable that influences ambient creep deformation behavior in β Ti alloys [7-19]. Moreover, it has been observed that the alloy composition with respect to phase stability also has an effect on the ambient temperature creep deformation behavior [7, 8] (phase stability in β Ti alloys can generally be defined as the stability of the alloy with respect to the retainment of complete BCC β phase content, i.e. a more stable β Ti alloy is one that has a larger content of alloying element, a less stable β Ti alloy is one that has small amounts of alloying elements to be further expounded upon in chapter 2). Fundamental ambient temperature creep investigations in various alloy β Ti alloys have observed creep deformation mechanisms to be: slip, twinning, slip accompanied by twinning, and twinning in the form of stress-induced plates consisting of ω phase particles (depending on phase stability) [7].

More stable alloys respond to ambient temperature creep by deforming only by slip, whereas lesser stable alloys respond to creep by twinning, or slip accompanied by twinning depending on alloy composition (i.e. phase stability) [7, 8]. Deformation twins of the {112}<111> type has been frequently observed at ambient temperature deformation in Ti-V, Ti-Mo, and Ti-Mo-Zr alloy systems [7-18]. These twins have been observed in both highly stable and less phase stability alloys. Ankem et. al. observed [112]<111> in a metastable beta Ti-

14.8Weight%Vanadium (Ti-14.8V) alloy [8]. {112}<111> twins were also observed by Paris et. al. in more stable Ti-V alloys consisting of larger alloy content ranging from 20 to 40 weight percent [15]. Paris suggested that the amount of twinning is controlled by the amount of ω phase present in the material (note: the amount of β and ω phase present in a material depends on the alloying content which affects the phase stability as well as the heat treatment conditions, discussed in detail in chapter 2 and appendix) [15]. Furthermore, Paris observed that the deformation behavior changed from twinning to slip when the volume fraction of ω phase present exceeded a value of 0.6 (corresponding to a vanadium content of 20 weight percent). Twins of the {112}<111> type were also observed by Ling et. al. in deformation studies conducted on Ti-V alloys consisting of various alloying content [19]. It was also observed by Ling et. al. that the deformation behavior changed from {112}<111> twins to slip as the alloying content increased, i.e. as the β phase stability was increased (i.e. the amount of ω phase content was decreased) [19].

In addition to observation of {112}<111> twins in β phase Ti alloys, {332}<113> type twins have also been observed in Ti-V, Ti-Mo, and Ti-Mo-Zr alloys [7-19]. In ambient temperature creep deformation studies conducted by Ramesh and Ankem on Ti-14.8V alloy consisting of various grain sizes (18, 25, 35, 350 μm), twins of the {332}<113> type were observed [8]. Accordingly, stress induced plate formation (SIP) in the form of ω phase and twinning and slip were observed in all grain sizes, however, the extent to which these deformation modes were formed depended on the grain size. This deformation behavior was more readily observed in the larger 350 μm grain size, as compared to the smaller

grain sizes of 18, 25, and 35 μm where the observed {332}<113> twins were less pronounced [8]. In an ambient temperature creep study conducted by Hanada and Izumi on Ti-V alloys with vanadium contents ranging from 18-50 weight percent, it was observed that alloys with the lowest amount of alloying content deformed by {332}<113> twinning which consisted of stress induced ω phase [12]. In deformation studies performed on Ti-Cr alloys with Cr contents ranging from 8 to 20 weight percent by Hanada and Izumi, {332}<113> twins were present in all alloys, however, slip behavior was observed in alloys consisting of higher Cr content [13]. Stress induced ω phase was also observed within the twins; in addition, anisotropy of the ω phase decreased with the increase in stability of the β phase. Thus, alloys with medium stability deformed by {332}<113> twins, however, there was an absence of stress assisted ω phase deformation products [12]. High stability alloys (alloys that consisted of large amounts of alloying content) deformed only by slip.

Creep Behavior

Low temperature creep behavior ($< 0.4T_m$, where T_m is melt temperature) under constant applied loading is of the transient type, essentially reaches creep exhaustion during stage one, where primary creep is typically the dominant mechanism [20, 21]. Strains exhibited in the primary creep regime are typically small and are usually on the order of less than one percent [19, 20]. Alloys that experience a large accumulation of primary creep strains can be described by a power law equation as a function of creep strain with time, given by the following equation [7, 8, 20-22]:

$$\varepsilon = At^a \quad (1)$$

where A is the creep coefficient, t is time and a is the time exponent which indicates the exhaustion rate during creep. Smaller a values indicate rapid exhaustion rate during creep, and a value of a = 1/3 is the classic Andrade creep behavior [22]. Creep exponent values for titanium alloys have been found to range from values of 0.03 to 1 [22].

Activation Energy

Activation energies for low temperature creep behavior of metal alloys can be determined based on the power law creep behavior. Odegard and Thompson determined the activation energies for non-steady state creep behavior at constant stresses for an α Ti, Ti-5Al-2.5Sn alloy for the strain rate as a function of strain by using the time derivative of the creep power law equation (equation 1) which is given by equation 2 [23]. This equation is the following:

$$\dot{\varepsilon}(\varepsilon) = aA^{\frac{1}{a}}(\varepsilon)^{1-\frac{1}{a}} \quad (2)$$

The activation energy, Q(ε) at a given uniaxial stress σ, was determined from the following equation:

$$Q(\varepsilon) = -R\left[\frac{\Delta \ln \dot{\varepsilon}(\varepsilon)}{\Delta(1/T)}\right]_{const.\sigma,\varepsilon} \quad (3)$$

where T is temperature, R is the universal gas constant, σ is constant uniaxial

normalized stress (with respect to the corresponding yield stress at a given temperature), and ε is the selected strain level at which Q(ε) is determined. The activation energy Q(ε) in equation 3 may vary depending on the strain level ε chosen for non-steady state primary creep. To address this variation, Odegard and Thompson calculated Q(ε) value for different strain levels and calculated an average Q(ε) value [24]. The variations of Q(ε) with strains were determined to be very small, therefore suggesting that determination of an average value is acceptable for calculation of Q. Deformation mechanisms observed by Odegard and Thompson were mostly slip and twins. Although Odegard and Thompson's study was conducted on an α Ti alloy, their equation was effective for calculating the activation energy for microstructure as a function of power law creep behavior. Furthermore, several scientists have used Odegard and Thompson's equation in determining the activation energies for creep deformation mechanisms in beta titanium alloys [25, 26].

Prior to Odegard and Thompson's study, Cuddy used a similar procedure to determine the activation energies at different strain levels for 304 stainless steel samples, in which it was discovered that the activation energies did not vary significantly with strains [26]. For steady-state conditions, Cuddy determined that for a given strain level, the strain rate is proportional to σ^n (see equation 4) [26].

$$\dot{\varepsilon} \alpha \left[\sigma^n\right]_{const.T,\varepsilon} \tag{4}$$

Therefore, based on the results of Odegard and Thompson and Cuddy, the following equation 5 can be used to determine the activation energy Q for non-

steady state conditions, considering that the average Q may have to be determined if it changes significantly with the strain level ε [26].

$$\dot{\varepsilon}(\varepsilon) = \left[A\sigma^{n} \exp\left(\frac{-Q(\varepsilon)}{RT} \right) \right] \tag{5}$$

Knowledge of activation energy Q values is essential to establishing the deformation mechanisms responsible for low temperature primary creep behavior in beta titanium alloys.

Hollomon Constants

Primary creep flow behavior can be predicted based on a few tensile tests and use of the Hollomon equation. In their 1947 General Electric Review Part I paper, J. H. Hollomon and J. D. Lubahn proposed that tedious, time-consuming creep tests do not have to be performed to observe long term deformation behavior [27]. Instead, the authors suggested that it is possible to predict flow behavior of metals based on a few stress-strain tests (tensile tests) and use of a fundamental equation relating stress, strain rate and temperature and determination of relevant constants.

Hollomon proposed that based on measurements of several strain-stain curves of metals at constant temperature and strain rate, that stress at a constant strain rate and temperature increases with strain according to the following equation:

$$\sigma = B_1 \varepsilon^{m} \tag{6}$$

where: constants are B_1, the strength coefficient and m is the strain-hardening exponent [27]. The strain hardening exponent, m can be determined from the slope of the natural log stress versus natural log strain plot:

$$m = \frac{d\ln\sigma}{d\ln\varepsilon} \tag{7}$$

Subsequent to Hollomon and Lubahn's initial report, several scientists attempted to correlate the creep and constant strain rate behavior in metals; including Lubahn himself who followed up in 1952 with an equation which related the materials constants, the strain hardening exponent, n, the strain rate sensitivity, m, and the creep deceleration rate p, where p = -n/m and the creep rate is defined as [28]:

$$\dot{\varepsilon} = C\varepsilon^{p} \tag{8}$$

Although the introduced equation was a unique attempt at developing a relationship, Lubahn, however, did not derive a precise relationship for the creep constant C [28, 29]. Lubahn followed up again in 1961 with R.P. Felgar in a book entitled, *Plasticity and Creep of Metals*, where they attempted to predict the constant strain rate law from a family of creep curves, however, they instead provided several examples correlating constant strain rate and creep behavior [28, 29].

Recently, Neeraj et. al. [22] showed that the Hollomon (strain rate sensitive) equation for flow stress behavior can reasonably predict low temperature creep deformation behavior from a limited set of constant strain rate data for a titanium alloy. An explicit analytical equation, which related the creep power law equation and Hollomon strain rate sensitive law was developed. This analytical result (see equation 5) was used to predict long-term creep

deformation behavior of titanium alloys. The strain-rate sensitive Hollomon flow equation (flow stress is a function of both strain and strain rate) is the following [22]:

$$\sigma = K\varepsilon^{n}\dot{\varepsilon}^{m} \tag{9}$$

σ is the true stress, ε is the true plastic strain, $\dot{\varepsilon}$ is the plastic strain rate, K is the strength parameter, n is the strain hardening exponent and m is the strain rate sensitivity. When this equation is rearranged, it can be directly related to the creep power law equation given in equation 1.

Reviewing briefly Neeraj's analytical derivation, from equation 5 the strain rate during plastic flow is determined by the following equation:

$$\dot{\varepsilon} = \frac{d\varepsilon}{dt} = \left(\frac{\sigma}{K}\right)^{\frac{1}{m}} \cdot \varepsilon^{\frac{-n}{m}} \tag{10}$$

Integrating equation 10 the following equation is obtained:

$$\int \varepsilon^{\frac{n}{m}} d\varepsilon = \int \left(\frac{\sigma}{K}\right)^{\frac{1}{m}} dt \tag{11}$$

Integrating equation 11 and assuming that K is independent of time, gives:

$$\varepsilon = \left(\frac{\sigma}{K}\right)^{\frac{1}{m+n}} \cdot \left(\frac{m+n}{m}\right)^{\frac{m}{m+n}} \cdot t^{\frac{m}{m+n}} \tag{12}$$

As can be observed, equation 12 has the same form as equation 1. From direct comparison of equations 1 and 12 the creep constants a and A can be obtained, which are the following:

$$a = \left(\frac{m}{m+n}\right) \tag{13}$$

$$A = \left(\frac{\sigma}{K}\right)^{\frac{1}{m+n}} \cdot \left(\frac{m+n}{m}\right)^{\frac{m}{m+n}} \tag{14}$$

Therefore, as described by Neeraj, the Hollomon equation suggests a directly power law form for the time dependence of creep [22]. As a result, the quantities K, n, and m can be directly measured from constant strain rate, tensile experiments; and the power law creep behavior of a material can be predicted based on equations 1, 9, and 12 - 14.

Further elaborating on Mill's work, stress, σ can be directly obtained as a function of time, strain and the Hollomon constants n and m by rearranging equation (12), which results in the following form:

$$\sigma = K\varepsilon^{n+m}\left(\frac{m}{m+n}\right)^{m} t^{-m} \tag{15}$$

equation (15) is feasible when one solves equation (12) for the stress, σ.

It should be noted that the Hollomon equation suggests a power law form for the time dependence of creep [22, 26-29]. In addition, the strain hardening exponent n, can have values ranging from n = 0 (which is indicative of a perfectly plastic solid) to n = 1 (an elastic solid) [22]. Furthermore, as the strain hardening exponent n approaches zero, the creep time exponent a, approaches a value of 1, which is indicative of steady state creep flow behavior [22, 26-29]. Considering these conditions, the Hollomon equation can be an effective method to assess the creep flow behavior of a material. Futhermore, determination of Hollomon constants can be an effective means to predict low temperature creep behavior of metal alloys. These constants can be determined directly from constant strain rate tensile experiments and can be correlated directly to the creep power law equation which fits reasonably well with low temperature creep behavior.

Uniqueness of Study

There has been a significant amount of research on understanding the ambient temperature creep deformation behavior of beta titanium alloys, as well as several studies performed on understanding the intermediate and high temperature creep deformation behavior of such alloys [30-36, 7-19]. Accordingly, these studies were devoted to understanding the nature of the ambient temperature creep deformation behavior and the diffusive behavior of solute elements and corresponding activation energies responsible for diffusion at ambient, intermediate and high temperatures [30-36]. Furthermore, these studies were focused on determination of the diffusive coefficient, D for impurity diffusion and the corresponding activation energy value based on diffusive behavior and not activation energy based on creep behavior. The alloys investigated were Ti-H, Ti-Al-38Nb beta + orthorhombic phase alloy, Ti-5Al-2Sn-4Zr-4Mo-2Cr-1Fe, Ti-Cr, Ti-Fe, Ti-Mo.

Minimal research has been conducted on understanding the exact mechanisms responsible for low temperature (in the range of 298 to 873K) creep deformation behavior in large grained beta titanium alloys, most of the studies have been devoted to ambient temperature deformation behavior [7, 8, 37, 38]. There has been a significant amount of research performed on comprehending ambient temperature creep deformation behavior of beta Ti-V alloys, however, no research has been conducted on understanding the low temperature (in regards to temperature testing of metals, the temperature range of 298K to 873K is considered to be low temperature, 873-1173K is considered intermediate temperature and above 1173K is considered to be high temperature) creep

deformation mechanisms responsible for creep behavior of Ti-V alloys and corresponding activation energies.

Hollmon constants have been determined for $\alpha + \beta$ alloys [22], however, they have not been determined for β Ti alloys in particular for Ti-14.8V. This is the first determination of Hollomon constants for different grain sizes for β Ti.

Research Objectives and Approach

In order to contribute to the understanding of low temperature creep deformation mechanisms and how they are affected by microstructure and alloying of beta phase titanium alloys (phase stability), this study investigated the low temperature creep deformation behavior in the range of 298-458K (25-185^{o}C) of a large grained, 350 μm Ti-14.8V alloy, determined the activation energies of primary creep deformation mechanisms and developed a predictive deformation model for beta titanium alloys. Understanding the deformation mechanisms responsible for low temperature creep behavior of beta phase titanium is essential to the design and development of titanium alloys with optimal microstructures and ideal mechanical creep resistance properties for low temperature applications like the aerospace, biomedical and nuclear industries where low temperature creep resistance is vital. Furthermore, the microstructure is an important variable that influences creep strain in titanium alloys.

Determination of activation energies of deformation mechanisms responsible for low temperature creep deformation behavior in large grained 350 μm beta Ti-14.8V alloy and development of predictive deformation model is the focus of this study. Investigation was pursued by conducting low temperature mechanical testing, tensile and creep, analytical examination of resulting

activation energies and Hollomon constants flow behavior, identification and determination of responsible deformation mechanisms by microscopy, and development of predictive deformation model for designed beta titanium alloys.

Tensile tests were performed in vacuum to minimize the amount of oxidation at constant strain rate at five temperatures, 298, 338, 378, 418 and 458K (25, 65, 105, 145, 185°C). 95% yield stress (YS) values were determined from the resulting stress versus strain tensile plots and respective loading conditions were determined for creep tests. Creep tests were performed in argon at the determined loading conditions based on calculated 95% YS values at the same five test temperatures. The apparent activation energies of the responsible creep deformation mechanism for Ti-14.8V were determined. Hollomon constants for predicting creep flow behavior were determined and were compared with Hollomon constant values determined for α phase titanium alloys. Resulting creep deformed samples were visually inspected by scanning electron microscopy (SEM) and transmission electron microscopy (TEM) images for identification of low temperature primary creep deformation mechanisms. Fundamental theoretical evaluations and experimental results were used to develop low temperature creep deformation predictive model for beta titanium alloys.

Prior to presenting the materials, experimental procedure and characterization methods implemented for this research (chapter 3), a technical foundation for understanding metastable beta titanium alloys, the Ti-V alloy system, and the nature of creep deformation mechanisms in beta titanium is detailed in chapter 2. Experimental results and analytical results – determined

activation energies for creep deformation mechanisms, Hollomon constants and predictive deformation model are presented in chapter 4.

CHAPTER 2

TECHNICAL BACKGROUND

The purpose of this chapter is to review the phase stability of beta phase titanium, beta phase titanium's metastable decomposition products (ω phase and martensite), how the decomposition products affect low temperature creep deformation behavior and corresponding deformation mechanisms to understand the activation energies responsible for low temperature creep behavior; as well as provide foundation for the theoretical predictive model for beta phase titanium alloys. Creep deformation behavior of beta titanium alloys is governed by its phase stability, which is a factor of the alloy composition. A literature overview of low temperature creep deformation studies of beta titanium alloys in general as well as beta titanium alloys consisting of different grain sizes and phase stabilities, as well as previous investigative studies of activation energies determination of beta titanium alloys to illustrate how phase stability and alloy type effect the creep deformation behavior.

Beta Titanium Alloys

It should be noted that the subject of beta titanium alloys is very broad and the reader should refer to references (1-6, 39-42) for further detailed information. Beta (β) titanium alloys are alloys that contain a sufficient amount of alloying elements (from here on referred to as β stabilizers) to retain virtually 100% beta phase, body centered cubic (BCC) structure upon quenching from above the beta transient temperature (also referred to as beta transus

temperature, 883°C, the boundary between single phase beta region and two phase alpha + beta region, alpha (α) phase is hexagonal close packed (HCP)) to room temperature after heat treatment. Therefore, in order to have ideally 100% β phase, an alloy must consist of enough β stabilizer i.e., a critical minimum level of β stabilizing content (β_c) to prevent passing through the martensitic start temperature (M_s) and the formation of α phase and resulting decomposition metastable products like martensite, ω and β' phases (detailed in the appendix) see figure 1. β stabilizing elements are typically transition metals and some noble metals and are those elements located to the right of titanium on the periodic table, e.g., metals from groups VA, VIA, VIIA, VIIIA. These elements are significantly more soluble in the β field than in α and therefore stabilizes the β phase [43].

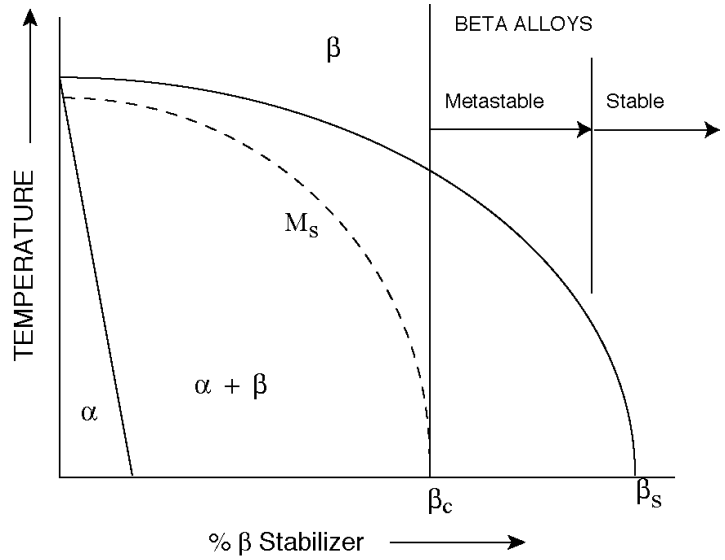

Figure 1 - Pseudo isomorphous binary phase diagram indicating martensitic start temperature [5]

Phase Stability

As mentioned in the previous section, a significant amount of β stabilizing elements must be added to avoid the M_s, martensitic start temperature and prevent the formation of metastable decomposition products like martensite, ω and β′ phase; however, these metastable decomposition products form during quenching as well as during further aging (details regarding both martensite and ω phase are highlighted in the following sections; a brief synopsis is given in the appendix regarding the β′ phase as its occurrence is rare and was not observed in this study). Alloys that lie between the critical minimum level for beta stabilizer content, β_c, and the complete stable β phase β_s point are still within the region that can result in the β phase and some decomposition metastable product. Therefore, although theoretically it is possible to quench from the β transus temperature and retain 100% beta phase, in such alloys the beta phase is metastable and will most likely precipitate some metastable decomposition product during quenching and/or during further aging [1,41]. These alloys that lie between β_c and β_s are therefore termed metastable β titanium alloys because they consist of some metastable decomposition product. While, alloys that are to the right of β_s are considered to be completely stable beta alloys, which, theoretically means that there is no precipitation of any metastable decomposition products. Figures 1-3 are schematics of pseudo phase diagrams and time-temperature-transformation diagram indicating the M_s temperature, regions for metastable decomposition products of ω, and β′. As can be viewed, alloys quenched to the right of both the M_s temperature and β_c point but to the

left of β_s can consist of both ω and β phase. It can also be viewed that such alloys quenched in between the M_s, β_c and β_s region may also contain ω, β and β′ phases (as mentioned previously, this occurrence is very rare).

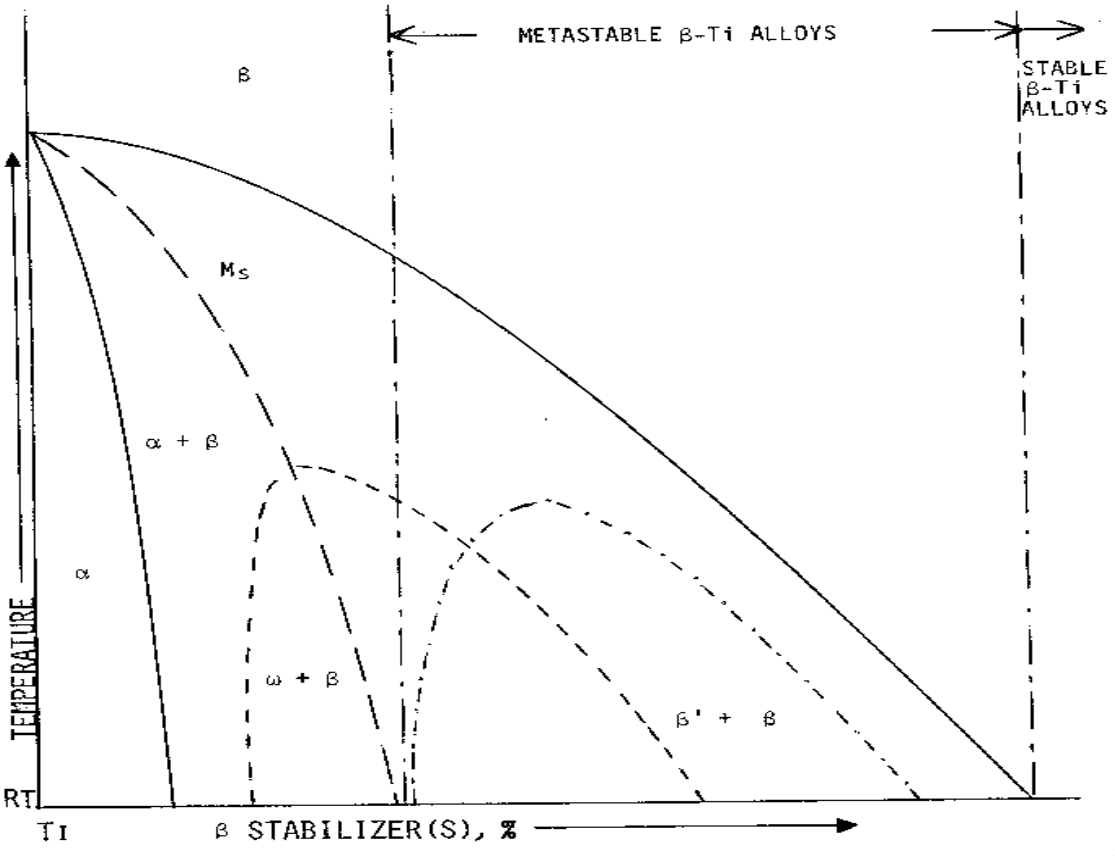

Figure 2 - Schematic of pseudo binary equilibrium diagram indicating metastable decomposition products ω and β′ phase region [57].

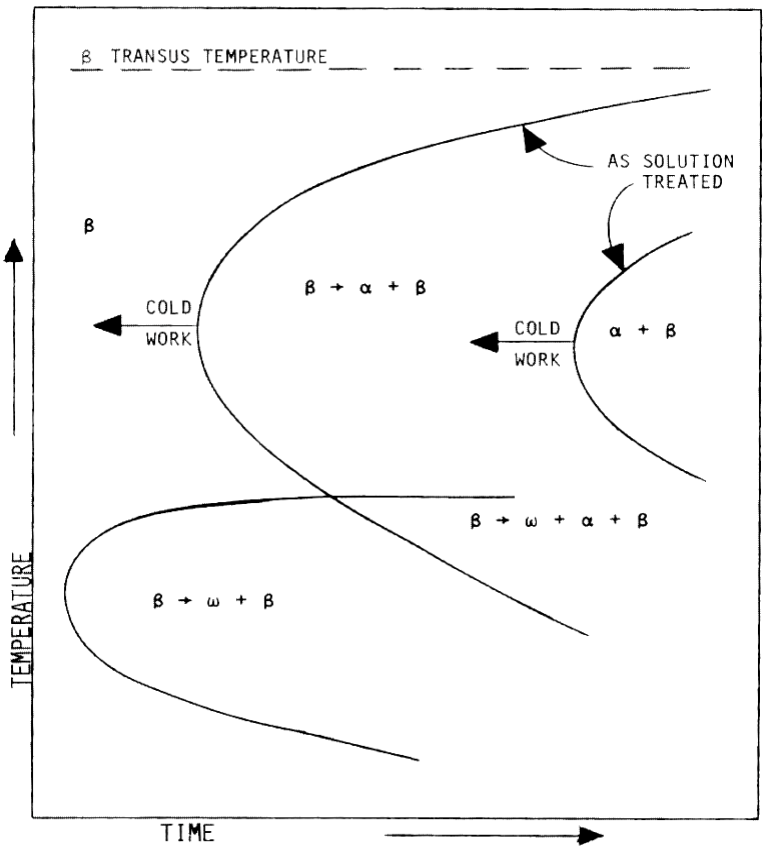

Figure 3 – Time-Temperature-Transformation Diagram of Solute Lean Metastable β Titanium Alloys [57]

The overall phase stability of a beta titanium alloy consisting of various alloying additions can be determined by a term known as the Molybdenum Equivalency (MoE) [41]. This term utilizes molybdenum (Mo) as a baseline with respect to the alloying additions to stabilize the beta phase and other possible beta stabilizing elements minus aluminum (Al), which stabilizes the α phase. The MoE is defined by the following equation:

MoE = 1.0 (Wt% Mo) + 0.67 (Wt% V) + 0.44 (Wt% W) + 0.28 (Wt% Nb)

+ 0.22 (Wt% Ta) + 2.9 (Wt% Fe) + 1.6 (Wt% Cr) … - 1.0 (Wt% Al) (16)

In equation 16, the value before each alloying element is the ratio amount of β_c for the Mo baseline (which is 10%) divided by the β_c value for the specific β

stabilizing alloying element. Basically, a MoE value of approximately ten percent is needed to stabilize the β phase upon quenching to room temperature [41]. The negative value for Al reflects its opposite ability to stabilize the α phase. Therefore, the amount of element required to stabilize β phase titanium is determined from the MoE value. Furthermore, an increase in the amount of β phase stabilizer added will result in a more stable β phase titanium alloy; likewise, a decreased amount of stabilizer will result in a less stable alloy. Accordingly, the stability of an alloy has an effect on its mechanical (deformation) properties. A MoE value of approximately 10.0 is required to stabilize the beta phase upon quenching [41]. Table 1 lists the various beta stabilizing elements and the approximate weight percentages required to retain 100% beta phase when quenched [41]. It is still however, unclear as to what MoE value is required to produce a truly completely stable beta alloy since metastable decomposition products has been observed in Ti-30Mo alloy (MoE = 30) and is unstable at elevated temperatures and under applied stress [41].

Table 1 – β Stabilizing Elements Critical Values [41]

β Stabilizer	Type	β_c(Wt%)	β temp suppression (°C)
Mo	Isomorphous	10.0	63
V	Isomorphous	15.0	72
W	Isomorphous	22.5	45
Cr	Isomorphous	36.0	55
Ta	Isomorphous	45.0	39
Fe	Eutectoid	3.5	90
Cr	Eutectoid	6.5	81
Cu	Eutectoid	13.0	72
Ni	Eutectoid	9.0	104
Co	Eutectoid	7.0	100
Mn	Eutectoid	6.5	104
Si	Eutectoid	-	158

The phase diagram for the isomorphous Ti-V system is given in figure 4 [44]. As can be observed in figure 4, addition of V at amounts greater that 14.5 Wt% lowers the beta transus temperature and increases the potential for retained beta phase BCC structure; this corresponds to the β_c value of 15% listed in table 1. Any values less than 14.5%, increases the potential for formation of martensite and ω phase metastable decomposition products when quenched to 800°C. It can also be observed that alloying contents in the range of 2-14.5Wt% results in a two-phase α+β alloy when quenched at approximately 720°C. Alloying contents in the range of 0-2Wt% results in an α phase alloy. The alloy investigated in this study was a metastable titanium-vanadium alloy, consisting of 14.8 weight percent vanadium (Ti-14.8V) with a MoE value of 9.9. The resulting quenched alloy consisted of both β phase and metastable decomposition product ω phase; metastable β' phase was not observed. Further discussion regarding the processing, microstructure and analysis of this alloy is given in chapter 3: the experimental procedure and materials and chapter 4: results. As well as the

deformed metastable decomposition products observed after deformation (tensile and creep testing).

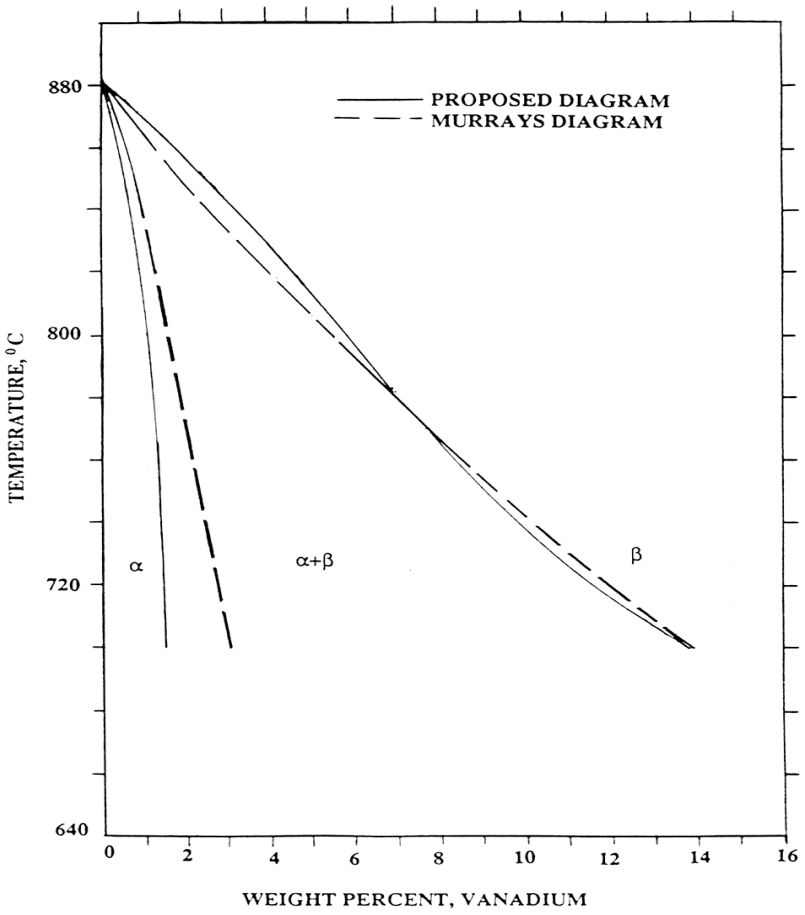

Figure 4 – Partial Ti-rich end of Ti-V phase diagram [44]

Metastable Decomposition Phases

Martensite transformation is a term that may be defined as a diffusionless shear transformation, which occurs as a result of quenching an alloy to room temperature [1, 39-42]. Martensitic transformation occurs as a result of cooperative movement of atoms which results in the homogeneous transformation from one crystal lattice structure to another [1]. Two types of martensite decomposition products have been frequently observed to for in beta titanium alloys, they are α' and α''; the crystal structure of α' is HCP, where as α" crystal structure is orthorhombic. The temperature at which martensite begins to form during quenching, the M_s temperature, depends on the alloy content, i.e. composition (see figures 1 and 2 for schematic phase diagram showing the dependence of composition of the martensitic start temperature) [5].

The goal of alloying metals in one aspect is to inhibit the movement of atomic planes which thereby reduces the distance over which atomic regions can cooperate and therefore perturbs the microstructure of the transformation product and also reduces the speed of the transformation and therefore causes it to be in competition with the nucleation and growth (kinetic) mechanism [1]. In transmission electron microscope (TEM) cooling stage experiments performed by Jepson, Brown and Gray on Ti-Nb alloys consisting of various concentrations, it was shown that the critical cooling rate (quenching at temperatures at a faster rate greater than the Ms temperature) decreased with increasing Nb concentration [45]. Thus, the presence of quenched martensitic decomposition products decreased with the increase of beta stabilizers, i.e. the presence of martensite decreases with the increase in alloy phase stability.

Martensite

Martensite has also been observed as stress-induced deformation products; Williams [46], Suzuki and Wuttig [47], Oka and Taniguchi, and Duerig [49.50], on occasion stress induced martensite has been observed to be accompanied by twins in Ti-Mo, Ti-10V, Ti-15.5V alloys (twinning will be mentioned in this section, however, it will be discussed in further detail in subsequent sections). Stress induced martensite is martensite when forms as a result of applied stresses. Beta titanium alloys that have been quenched close to the M_s temperature respond to applied stresses by martensitic formation, whereas, alloys that are further away from the M_s temperature respond to applied stress by deforming only twinning; which was the observed behavior of Ti-14.8V alloy previously investigated by Ankem et. al. [8,10]. Twinning as well as stress-induced martensite, has been observed by Oka and Taniguchi in Ti-Mo alloys [48]. Duerig et. al. also observed martensite plates accompanied by twins of the {112}<111> type in a Ti-10V-2Fe-3Al alloy [49]. In Duerig's observations, it was recognized that the martensitic plates did not often terminate within a grain, instead, the plates proceeded across the length of the grain until another plate or grain boundary was encountered [49]. Duerig evaluated the lattice constants of this phase and determined them to be: a = 3.01 Å, b = 4.83 Å, c = 4.62 Å; he also proposed a schematic (see figure 5) that relates the β phase BCC structure to the orthorhombic α" phase [49]. There has been a considerable amount of controversy as to the actual nature of these observed plates, through TEM observations made by Ankem et. al. on a Ti-14.8V alloy, it was evidenced that these plates were twins and not martensite [10].

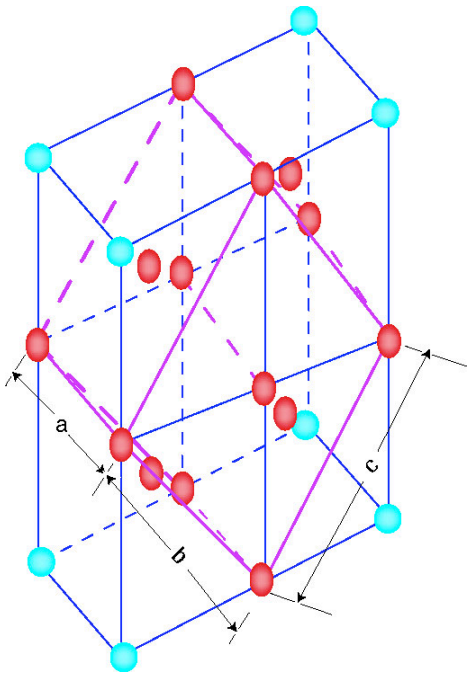

Figure 5 – Schematic relationship between β phase and orthorhombic α″ phase [49]

ω Phase

A considerable amount of interest has been devoted as well as investigative research performed over the past five decades by many scientists in understanding the overall nature of the metastable ω phase [1]. This interest is chiefly due to in part to the unusual mode of transformation from the parent β phase (BCC) structure to the hexagonal close packed (HCP) ω phase and its remarkable effect on the resulting mechanical properties of the alloy; the presence of the ω phase promotes increased strength and reduced ductility (to be discussed in detail in the following section on observed deformation behavior and deformation products). As discussed in the previous section, the ω phase is a metastable decomposition product of β titanium; this phase precipitates as two distinct types, athermal ω and isothermal ω phase. Athermal ω phase forms during quenching as a result of diffusionless martensitic process; whereas

isothermal ω phase forms as a result of diffusion controlled process during tempering, i.e., subsequent ageing of the alloy. Focus in this study is devoted to athermal ω phase as the alloy investigated was rapidly quenched and was not subjected to further ageing.

The ω phase forms in metastable beta Ti alloys that are stabilized with transition elements like V (also Mn, Cr). As can be observed in figures 2-3, quenching rapidly from the beta transus temperature results in the formation of the ω phase as a crystalline precipitate and a fluctuating component; this occurs in a narrow composition regime, which overlaps the boundary of the martensite phase formation [1]. Furthermore, since the ω phase forms at the threshold of the martensite start temperature, the formation of the ω phase is a similar mechanism [1]. The ω phase forms as a result of shearing of the lattice planes in the BCC lattice which results in a reduction of volume of ~3% [1,51,52]. This shearing has been proposed by Bargariatskii et. al. in a linear fault model to occur along the slip planes in the BCC lattice, i.e. {110} (see appendix for further details) [51,52]. The relationship between the parent BCC β phase and the HCP ω phase has been well established based in the initial studies of Frost, Bagariatskii and several others [51-55]. This relationship is based on the following plane relations:

1) $(0001)_{\omega} \| (111)_{\beta}$

2) $(11\bar{2}0)_{\omega} \| (1\bar{1}0)_{\beta}$

3) $(11\bar{2}0)_{\omega} \| (110)_{\beta}$

4) $(0001)_{\omega} \| (001)_{\beta}$

5) $(1\bar{2}10)_{\omega} \| (110)_{\beta}$

6) $(2\bar{1}\,\bar{1}0)_{\omega} \| (1\bar{1}0)_{\beta}$

The presence of the ω phase can be clearly seen in TEM diffraction patterns, it is typically observed as diffuse streaking or clear distinct spots contained within the BCC lattice. The intensity of the ω phase spots increases as the alloying content decreases. The more stable the alloy, i.e., the greater the β phase content, (the more alloying content), the ω phase is present as faint diffuse streaking in diffraction patterns. Whereas, the less alloying content, the presence of ω phase is increased giving rise to clear distinct spots in the resulting diffraction patterns.

It should be noted that ω phase has been observed in Ti-V alloys with alloying contents from 11-50wt% [56]. The effect of interstitial impurities on the ω phase formation in beta titanium has been investigated [16,56,57]. Titanium has a high affinity for oxygen as it readily occupies interstitial sites [1]. The presence of oxygen lowers the temperature at which the ω phase begins to form in Ti-V alloys [56,57]. Thus, the greater amount of oxygen interstitials the larger the amount of ω phase present upon quenching. Other investigative studies have reported that the addition of oxygen retards stress induced ω phase transformation and makes twinning difficult [12]. Essentially, the presence of oxygen in the interstitial sites makes it difficult for the shifting of atoms, thereby creating a blocked site.

Creep Behavior

Creep behavior of materials may be defined as time dependent deformation (strain) under constant stress (or constant loading) conditions. The duration of creep testing may vary depending upon the scope and nature of the investigation, some creep tests have been known to last as long as 10 years [20]. There are essentially three stages of creep these are primary, secondary and tertiary creep. Creep behavior at low temperatures $< 0.4T_m$ is usually of the transient type, essentially reaching creep exhaustion during stage one, primary creep is typically the predominant behavior [20,21].

Stage one, primary creep as can be viewed in the typical creep curve displayed in figure 6, in this stage creep rate is high and gradually decreases with time until the region of secondary or steady state creep is reached. Strains exhibited during the primary creep region are typically small, about less than one percent (< 1%), and are more comparable to acceptable engineering strains than the strain behavior exhibited in the secondary creep region [20,21]. Furthermore, creep behavior at low temperatures is generally of the transient type and typically achieves creep exhaustion during stage one and never reaches stage two, secondary creep [20].

Secondary creep, the second stage of creep behavior is a period of nearly constant creep rate, which is a result from a balance between strain hardening and recovery behavior; thus, secondary creep is usually referred to as steady-state creep [20,21]. In other words, stage 2, secondary creep is also called steady state creep because of the dynamic recovery processes, maintains a constant strain rate. Third stage, tertiary creep typically results from constant load creep tests at high stresses at high temperatures [20, 21]. Tertiary creep occurs when

there is a significant reduction in the test specimen's cross-sectional area either because of necking or internal void formation. Third stage creep behavior is usually associated with metallurgical changes in the material such as coarsening of particle precipitates, recrystallization or differential changes in the phases [20].

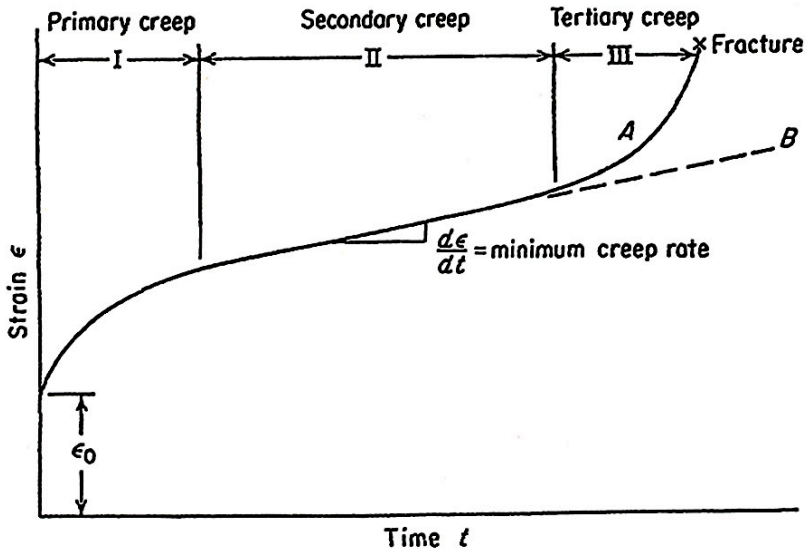

Figure 6 – Typical creep curve displaying three stages of creep leading to fracture [20,21].

In titanium alloys, ambient temperature creep behavior is typically in the primary creep region of the creep curve, which usually displays creep saturation [21]. Transient creep theory was initially proposed by Nabarro to describe the mechanism of low temperature logarithmic creep behavior; this theory considers the "exhaustion" of dislocation sources as the rate controlling mechanism [21]. This study examines the low creep behavior beta titanium alloys, in particular the deformation mechanisms responsible for low temperature creep behavior. Low temperature creep behavior is best described by a logarithmic fit, where as high temperature creep behavior is best fit by a power law curve [21]. At low temperatures and low stresses, the dependence of creep rate on time in the primary creep regime may be expressed as the following equation [21]:

$$\dot{\varepsilon} = \frac{\varepsilon_1}{t + t_0} \tag{17}$$

where ε_1 and t_0 are constants. Integrating equation 17, the following equation is obtained:

$$\varepsilon = \varepsilon_0 + \varepsilon_1 \ln(t + t_0) \tag{18}$$

In addition to being described by equations 17 and 18, low temperature primary creep behavior of many metals and alloys at low creep stresses and creep strains ($< 2 \times 10^{-3}$) has been described by a logarithmic creep law of the form:

$$\varepsilon = A(\ln t) + B \tag{19}$$

the constant A provides an idea of time dependence, B provides approximately the obtained strain during the first few minutes of creep testing, and t is time [7,8,10]. In cases where there is a large accumulation of primary creep strains, the deformation behavior is often described by a power law function of creep strain with time, which in equation 1. Smaller a values in equation 1 indicate rapid exhaustion rate during creep, where a value of a = 1/3 is the classic Andrade creep behavior [22]. Creep exponent values for titanium alloys have been found to range from values of 0.03 to 1 [22]. Accordingly, the creep power law equation 1 has been well described for many titanium materials [7-10,22,37,38].

Beta Titanium Deformation Mechanisms

Ambient temperature creep deformation behavior of beta titanium has been studied extensively in Ti-V, Ti-Mn, Ti-Cr, Ti-Mo, Ti-Mo-Zr alloys. Deformation mechanisms have been observed to be slip, slip accompanied by stress induced plates (SIP) in the form of twinning, and twinning depending on

alloy phase stability. Deformation occurs by slip in more stable alloys, i.e. alloys consisting of large alloying contents and high MoE values (as mentioned previously, alloys with high MoE values are more stable alloys) [7,13,14,16,18,58]. As the phase stability decreases, the observed deformation behavior is slip accompanied by twinning, and accordingly, in the least stable alloys respond to applied loading by deforming only by twinning [7,13,14,16,18,57,58].

Ambient temperature creep deformation in the more stable alloys has been observed to be fine, wavy slip to coarse slip as the alloying content decreases [14, 56]. As phase stability increases the deformation mechanisms changes to slip accompanied by SIP plates in the form of twinning to just twinning deformation. Slip is typically observed in more stable alloys whereas, slip and twinning as well as just twinning are observed in metastable beta titanium alloys. As mentioned in chapter 1, twins of the type {112}<111> and {332}<113> have been observed in metastable beta titanium. In particular twins of the type {332}<113> have been observed in Ti-14.8V. Figures 7 and 8 are schematics of diffraction patterns for {112}<111> and {332}<113> type twins observed in Ti-14.8V [8].

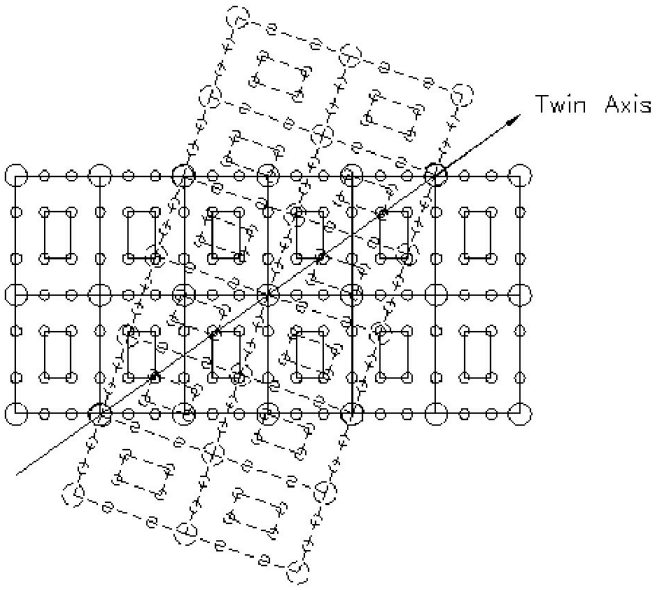

Figure 7 – Schematic of diffraction pattern of a {112}<111> type twin in a b Titanium alloy with athermal w phase. Smaller circles represent the w phase, the dashed lines represent the twin [8].

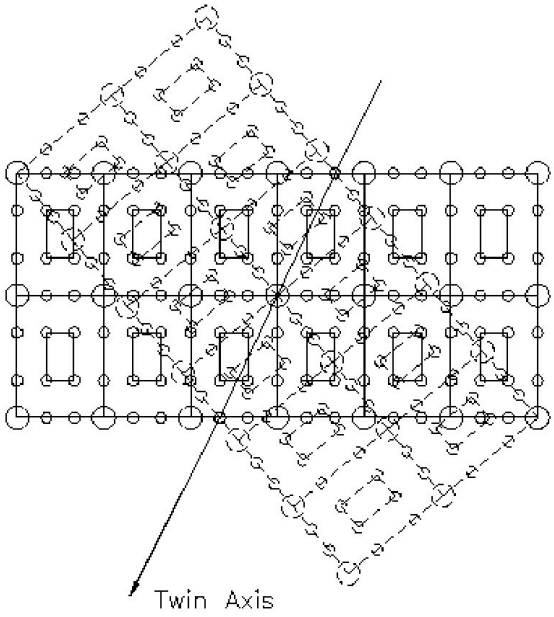

Figure 8 – Schematic of Diffraction Pattern of {332}<113> type twin in a beta titanium alloy with athermal w phase. The smaller circles represent the ω phase, the dashed lines represent the twin [10].

Deformation twins of the {112}<111> type has been frequently observed in Ti-V, Ti-Mo, and Ti-Mo-Zr alloy systems [8,10,16-19,37,52,58].

{112}<111> twins were observed by Paris et. al. in Ti-V alloys consisting of alloying content ranging from 20 to 40 weight percent [16]. Paris suggested that the amount of twinning is controlled by the amount of ω phase present in the material (note: the amount of β and ω phase present in a material depends on the alloying content as well as the heat treatment conditions) [16]. Paris observed that the deformation behavior changed from twinning to slip when the volume fraction of w phase present exceeded a value of 0.6 (corresponding to a vanadium content of 20 weight percent) [16]. Twins of the {112}<111> type were also observed by Ling et. al. in deformation studies conducted on Ti-V alloys consisting of various alloying content [19]. It was also observed by Ling et. al. that the deformation behavior changed from {112}<111> twins to slip as the alloying content increased, i.e. as the β phase stability was increased [19].

In addition to observation of {112}<111> twins in β phase Ti alloys, {332}<113> type twins have also been observed in Ti-V, Ti-Mo, and Ti-Mo-Zr alloys [8,10, 16-19,52,58]. In studies conducted by Ramesh and Ankem on a Ti-14.8Weight%V (Ti-14.8V) alloy consisting of various grain sizes (18, 25, 35, 350 μm) {332}<113> type twins were observed. Accordingly, stress induced plate formation (SIP) in the form of ω phase and twinning and slip were observed in all grain sizes, however, the extent to which these deformation modes were formed depended on the grain size. This deformation behavior was more readily observed in the larger 350 μm grain size, as compared to the smaller grain sizes of 18, 25, and 35 μm where the observed {332}<113> twins were less pronounced [8]. Figures 7 and 8 are schematics which depict the diffraction patterns that are

generated by the interface region between the {112}<111> and {332}<113> type twins and the parent matrix as developed by Ramesh [8,10,37].

In deformation studies performed on Ti-Cr alloys with Cr contents ranging from 8 to 20 weight percent by Hanada and Izumi, {332}<113> twins were present in all alloys, however, slip behavior was observed in alloys consisting of higher Cr content [13]. Stress induced ω phase was also observed within the twins; in addition, anisotropy of the ω phase decreased with the increase in stability of the β phase. As mentioned in the ω phase section, in another study conducted by Hanada and Izumi on Ti-V alloys with vanadium contents ranging from 18-50 weight percent, it was observed that alloys with the lowest amount of alloying content deformed by {332}<113> twinning which consisted of stress induced ω phase [12]. Thus, alloys with medium stability deformed by {332}<113> twins, however, there was an absence of stress assisted ω phase deformation products [12]. High stability alloys (alloys consisting of large amounts of alloying content) deformed only by slip. An interesting concept emerged as a result of their work, which was the determination of the effect of oxygen atoms on twinning. The addition of oxygen to the β phase materials tends to retard the ω phase transformation, therefore making it difficult for {332}<113> twins to form in oxygen doped β Ti alloys [17,60].

In another study conducted by Oka and Taniguchi observed on a Ti-15.5V alloy did not show ω phase cannot be present without the formation of twins as a result of deformation [15]. There has been however, reports of the absence of the ω phase in titanium alloys subjected to deformation by Hanada and Izumi in their examination of Ti-Nb and Ti-Mo alloys, which have stabilities comparable

to Ti-V alloys, where the ω phase has been observed after deformation [11]. What is also interesting is that Doraiswamy and Ankem reported observations of athermal ω phase present in Ti-9.4Mn alloy before and after deformation [7]. Therefore, the amount of ω phase present in an alloy depends on the phase stability and controls the amount of deformation as a result of its presence.

CHAPTER 3

EXPERIMENTAL PROCEDURE

Specimen Preparation

Material, Processing, Heat Treatment

The material used for this study was a metastable β phase Ti-14.8 weight% Vanadium (Ti-14.8V) alloy, which has a MoE value of 9.9; its elemental composition was determined after processing by wet chemistry at Reactive Metals Incorporated (RMI), located in Niles, Ohio and is listed as specified by the vendor in table 2. The actual hydrogen content of the test specimens is slightly less than the listed value, as the test samples were subjected to additional vacuum heat treatment after processing. Initial processing of the alloy was performed at RMI where it was melted into 13.6 kg ingots, then forged and rolled into the final as-received 1.74 cm (0.685 inch) diameter bars. Final processing of the bars was conducted in the α + β phase field at a temperature of 973K, which yields an area reduction of approximately 60%. Processing the alloy in this manner yields a final microstructure consisting of elongated grains and second phase particles. In addition, the material is in a fairly cold worked condition, which will reconstruct upon additional heat treatment to retain the β phase.

Table 2 – Compositional Analysis of β Phase Ti-14.8V Alloy

Alloying Element	Weight Percentage
Vanadium (V)	14.8
Iron (Fe)	0.01
Oxygen (O)	0.092
Nitrogen (N)	0.021
Carbon (C)	0.02
Hydrogen (H)	147 ppm
Titanium (Ti)	Balance

The as-received rods were cut into 8.89 cm (3.5 inches) in length and vacuum encapsulated (2 samples per tube) in quartz glass tubes at a pressure of 10^{-4} to 10^{-5} Pa (see figure 9) to prevent additional oxidation. The quartz tubes were heat treated in a Lindberg box furnace at a temperature of 1173K (900°C) for 2 hours, which was followed by furnace cooling to 963K (690°C) and then annealed at 963K for 200 hours (see table 3 for heat treatment furnace parameters). There were some fluctuations of ± 20°C at different times during the annealing period due to instability of the furnace. Precipitation of α flakes at the grain boundaries of the β matrix can result from the fluctuations in the furnace. Upon completion of annealing, the quartz tubes were cracked opened and the samples were water quenched to room temperature. This heat treatment yielded approximately a 100% β phase alloy with some coarse α flakes at the grain boundaries and grain sizes of ~350 μm.

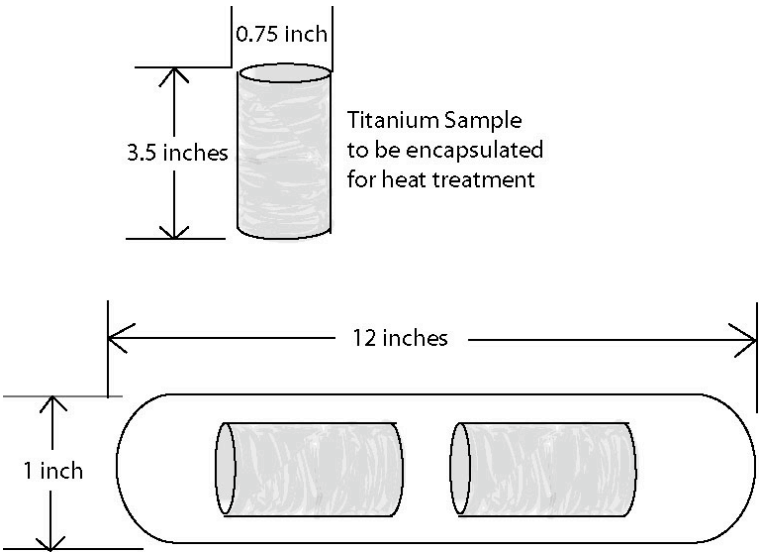

Figure 9 – Schematic of Vacuum Quartz Encapsulated Sample

Table 3 – Furnace Parameters for Heat Treatment

Parameter	Value
Alarm 1, A_1	0
Alarm 2, A_2	0
Proportional Band, P_b	35
Integral Time, t_1	15
Differential Time, t_d	10
Approach Control, A_P	1.0
Heat Cycle, H_C	0.3
Maximum Power, H_L	100

Tensile and Creep Specimens

Machining, Hand & Electro-Polishing, Etching

The heat-treated samples were machined into specific dimensions for tensile and creep test specimens at the University of Maryland. Tensile specimens were machined using a both lathe and mill machines into the following dimensions in order to fit into the grips of a Materials Research Furnace High Temperature tensile testing instrument (see figure 10 for schematic of tensile specimen): 8.89 cm (3.5 inches, ±0.005) in length, a gauge length of 4.318 cm (1.7 inches, ±0.005), a diameter of 1.5675 cm (0.625 inches, ± 0.005), holes were

drilled at both ends of specimen which had a diameter of 0.625 cm (0.25 inch ± 0.005). Machining the samples took a considerable amount of time to complete, as titanium is one of the hardest alloys, aside from nickel and cobalt, which makes it a challenge to machine. In addition, although the samples are heat treated, there is still a thin oxide layer on the surface, which is the most difficult layer to remove. It is essential that the oxide layer is removed to minimize the amount of oxygen present in the alloy. Machining of the specimens took a considerable amount of time as small amounts of material were removed at a time in order to minimize the amount of surface deformation during machining. Drilling and lathing one tensile sample took 16+ hours, in addition to the initial 12 hours to set up the lathe. Five samples were used for tensile testing, for a total machine time of approximately 92 hours.

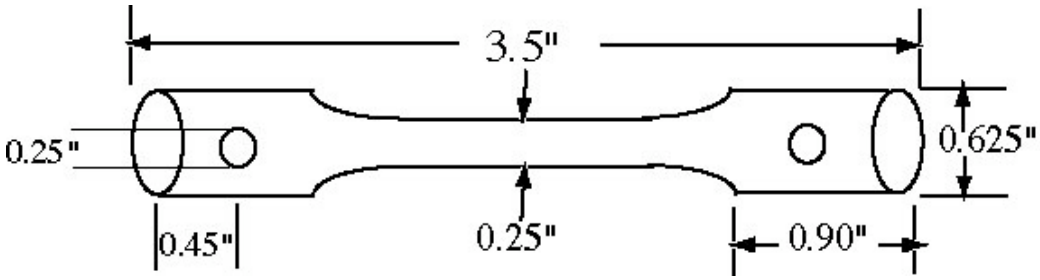

Figure 10 – Tensile Specimen

Creep specimens were also 8.89 cm (3.5 inches, ± 0.005) long, 1.23 cm in diameter (0.485 inch, ± 0.005), however, the gauge section was flat and was 2.86 cm (1.125 inches, ± 0.005) long. Flats were machined on the gauge sections by electron discharge machining (EDM) with the assistance of a Robofil wire cutter. Multiple passes and small cut depths were made during machining of the flats,

in order to minimize the strain induced on the specimen to a final thickness of 0.0492 cm (0.125 inch, ± 0.005). The purpose of the flats is to provide an area for observation of deformation mechanism. The creep samples were threaded on both ends with 13 threads per 1.27 cm (0.5 inch, ± 0.005) to fit into the threaded grips of the creep tester instrument; a schematic of the creep specimen is displayed in figure 11. It should be noted that during creep testing the threaded ends of the specimen experience negligible strain because they are held static in the pull rod grips, however, the gauge length section of the specimen experiences strain from the applied load.

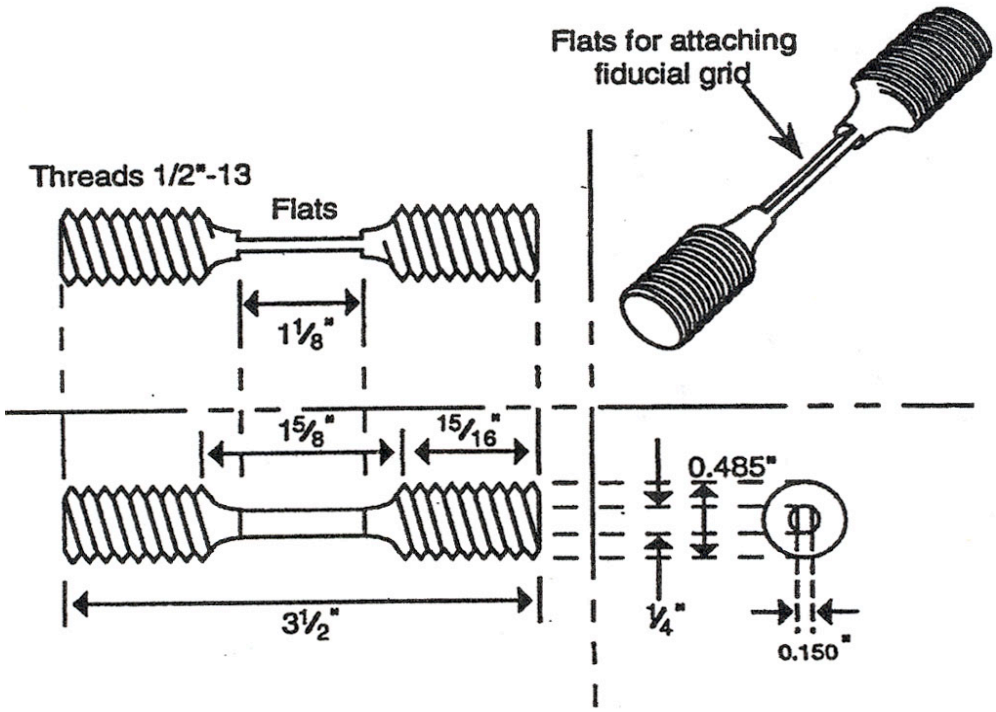

Figure 11 – Creep Specimen Schematic [61]

Machining creep specimens' flats by EDM processing results in a slightly rough surface consisting of an oxide layer, therefore the surfaces require additional processing like mechanical hand polishing in order to obtain a smooth surface. The flat portion of the specimens is initially hand polished with silicon carbide grit paper, which was supplied by Buehler Corporation, Lake Forest, IL. A relatively coarse 400 μm size silicon carbide grade grit paper was initially used to polish the flat surface for a period of approximately 6 hours on each side. Once the surface was completely smooth and removed of all scratches, a finer grit grade, 600 μm size paper was used for to polish for a duration of approximately 10-12 hours on each side. Once the flat had a smooth even sheen polish and was free of all scratches, a finer grade paper was used, 800 μm size for additional hand polishing. Polishing at the 800 μm size was performed for a duration of approximately 10-12 hours also. Polishing times varied as it depends highly on the initial surface condition of the flat. The sample is rotated 90° several times during polishing to ensure an even polish. In addition, each grit grade must be initially polished perpendicular to the direction of the previous grade until there are no scratches visible to the naked eye. Also, the sample is periodically rinsed with water and air dried during polishing to reduce abrasion by residual particles left on the surface from the grit paper during polishing. If scratching occurs, polishing must be performed at the lower grit size for removal before going to the larger grit size. Provided that there are no surface scratches during hand-polishing, a successful hand polish of one sample takes approximately 60 hours to complete.

After hand polishing, the creep samples were electropolished to yield a mirror like surface finish. The goal of this procedure is to remove any surface deformation products that may be induced during hand polishing; furthermore, electropolishing removes dirt and debris from the surface, as well as removes the thin oxide layer and yields a highly smooth, reflective mirror-like surface. Each creep sample was electropolished for approximately 30-45 minutes at a temperature of ~213K (-60°C) or lower in an electrolytic bath solution (best results were observed at temperatures lower than 193K (–80°C), see table 4 for solution composition). Cryogenic temperatures are achieved by using a solution mixture consisting of dry ice and methanol, which is kept in as a surrounding bath in a lined beaker in around the electrolytic bath. Ti specimen is placed inside of a beaker lined with a pure Ti sheet, which acts as the anode; the electropolished sample acts as the cathode in which Ti cations are released during the electropolishing process (see figure 12 for set up). The electrolytic bath is stirred continuously with the aid of a magnetic stir bar, which creates a small vortex in the solution in which the electrolytes moves continuously as the dirt is removed from the sample's surface. During electropolishing, a few thousandths of an inch of material is removed from the sample's surface, which eliminates most of the deformation caused by mechanical hand polishing, in addition to the removal of dirt, debris, as well as the thin oxide layer.

A Buehler electropolishing unit was used for applying direct current and electropolishing of the titanium specimen. The main controlling parameters in this process are both voltage and current. Ideally, a current of ~0.7 amperes is required to produce the desired current density in the specimen for a clean, smooth electropolished surface finish. Given a current of 0.7 A, the

corresponding voltage is in the range of 25-27 volts on the electropolishing unit; however, the unit used for this procedure has not been calibrated for several years, as the respective current for a voltage of 25-27 volts varied quite often and deviated from the value of 0.7A. Therefore, the applied current must be increased until a voltage of 25-27 is reached on the unit. An initial voltage of approximately ~50 volts is applied for about 20 seconds, to remove the thin oxide layer from the sample's surface. This oxide layer is typically formed when titanium is exposed in atmosphere (oxygen occupies octahedral sites easily in β Ti). Any deviation from these parameters is highly detrimental to the specimen's surface, as there could be electrochemical etching or even pitting on the specimen's surface. This process must be closely monitored by continuous visual inspection to ensure that the sample's surface is highly reflective. Reflecting light from a flashlight onto the immersed specimen aids in monitoring the electropolishing progress. The electropolishing procedure is complete when one can see their reflection completely on the mirrored specimen's flat surface. After the electropolishing process is completed, the sample is thoroughly rinsed with methanol and dried to room temperature.

Major challenges that were faced during electropolishing include a sudden jump in the current, which therefore increases the current and resulted in severe pitting of the sample's surface. As mentioned in the previously once pitting occurs on the sample, the electropolishing process must be stopped, and the sample must be hand polished all over again. This occurred several times and the entire hand polishing procedure had to be repeated, which took an additional 60 hours. One preventive measure is to carefully watch the electropolishing unit, if the current suddenly increases (i.e. if there is a sudden

increase in current value for example from an initial current value of 0.7 to 2.5) immediately decrease the voltage so that the current is respectively decreased. Another challenge faced during electropolishing was the magnetic stir bar losing its balance and thereby causing an inhomogeneous stir in the solution, which contain electrolytes and therefore also causes pitting on the sample. One preventive measure of this occurrence is not to set the stir too high, set the stir at a smooth, even paced spin. The electrolytes can be clearly observed from the reflectance of a flashlight. There were situations when the sample was completely electropolished prior to the designated electropolish time. As a result of the sample being electropolished, severe pitting occurred and handpolishing had to be repeated. To prevent over polishing, the sample must be removed immediately when electropolishing is complete.

Table 4 – Electropolish Solution

Chemical	Amount
Methanol (CH_3OH)	560 ml
Hydrofluoric Acid (HF)	15 ml
Sulfuric Acid (H_2SO_4)	25 ml

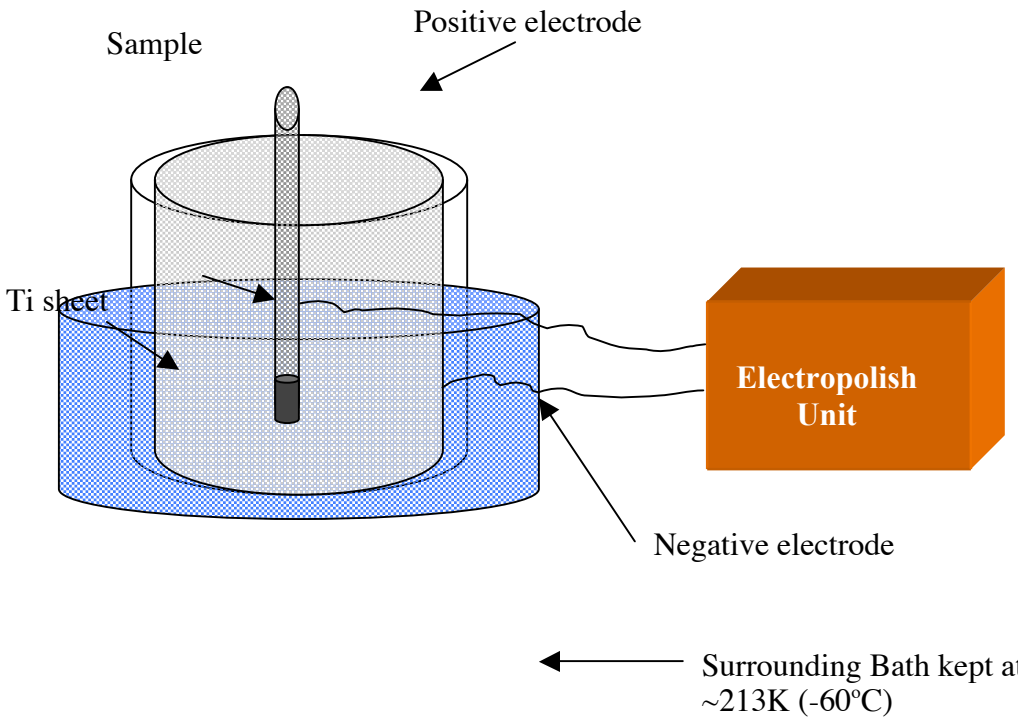

Figure 12 – Schematic of Electropolishing Set Up

Chemical etching is performed to reveal the specimen's grain structure, i.e. grain boundaries, once etched grain boundary lines are highly visible. Furthermore, etching the specimen's surface enables observation of deformation mechanisms such as slip lines to be more visible by optical and scanning electron microscopy (SEM). The samples surface was etched with R-etch solution (see table 5 for R-etch solution composition). Extreme safety precautions must be taken when preparing the R-etch solution as well as during etching of the sample as the solution is not only hazardous to one's health, but also flammable. The sample's surface is swabbed with R-etchant for approximately 90 seconds per side, then thoroughly rinsed with water and dried to room temperature. The sample is then inspected under an optical microscope to ensure that there are no etch pits on the surface and the grain boundaries are highly visible. There were a

few occasions where etch pits were pronounced, as a result the samples were handpolished and electropolished to remove the pits and etched again.

Table 5 – R-Etch Solution

Chemical	Amount
Ethanol	35 ml
Glycerin	40 ml
49% Hydrofluoric Acid (HF)	25 ml
Benzalkonium Chloride	17 ml

Once etching revealed the grain boundaries, grain size measurements were made by the line intercept (linear intercept) method. This method involves counting the number of grain boundaries intercepted by a 10 mm length scale and recording. Ten measurements are made and the average of these measurements are used for determination of grain sizes.

Fiducial Grid Attachment by Electron Lithography Technique

Fiducial grid lines have been used by several scientists in conjunction with optical microscopy to observe a metal alloy's deformation behavior, in particular, detection of slip lines, bulk shape changes and offsets at grain boundaries resulting sliding during plastic flow [62, 63]. Most observed deformation behavior in metal alloys has been on the order of one micron or less, therefore, developing a grid pattern technique that can be observed by scanning electron microscopy (SEM), can be a useful reference tool for observing small deformation mechanisms. In this research study, fiducial grid lines were patterned onto Ti-14.8V beta phase creep samples by photolithographic processes (techniques

utilized in the semiconductor industry) for observations of the deformation mechanisms responsible for creep deformation behavior. By obtaining images of specific areas of the grid pattern before and after creep deformation, the active deformation mechanisms can be observed in a specific referenced area. For example, if slip occurs, the grid lines are typically distorted. Accordingly, creep deformation behavior such as slip and twinning can also distort the grid pattern. In addition, the nucleation and growth of stress-induced plates (SIP) (in the form of twins, i.e. twinning behavior) can also be monitored.

The goal of this photolithographic process was to develop a fiducial grid pattern on a cross-sectional area of approximately 3 mm x 3 mm to establish an initial reference area prior to deformation (i.e. prior to creep testing). The grid pattern was achieved by the following measures: the sample's flat surface was initially cleaned by rinsing first with acetone, methanol, isopropyl alcohol and deionized water, then purged with nitrogen and subjected to a dehydration bake in a vacuum furnace oven at 443K (170^{o}C) for 6-8 hours. The purpose of initial cleaning is to remove any dust particles and/or debris that are not visible to the naked eye and to ensure a clean substrate surface for optimal resist adhesion (before subjecting to photolithography). After the dehydration bake, the sample is cooled to room temperature; then under a yellow safelight in a class 100 clean room, the sample is attached to a vacuum spinner chuck (supplied by Headway Research Inc.) and flooded with 5-6 drops of positive photo-resist Nano PMMA (polymethyl methacrylate, this photo-resist was supplied by the MicroChem company, Newton, MA) and spun at 3,500 rpm for 45 seconds (see figure 13 for schematic). PMMA was selected because of its high temperature robust and metallic adhesive properties. It should be noted that the resist thickness is

directly proportional to the speed at which the resist is spun/deposited. For PMMA, a spin speed of 3500 rpm yields a resist thickness of ~1100 Å (110 nm) thick. Spinning at a slower speed results in a thicker resist layer, for example a spin speed of 1000 rpm yields a resist thickness of ~1800 Å (180 nm). The sample is then baked (soft baked) in a vacuum furnace oven at 443K (170°C) for 30 minutes to harden the resist.

After completion of softbake, the sample is removed from the oven and cooled to room temperature under a yellow safe light and then placed in a black film bag to avoid direct exposure to normal light. It is imperative that the sample is cooled to room temperature before the next procedure so as to avoid cracking of the resist. The next step is to expose the resist by drawing the grid line pattern onto the resist; this was achieved by performing electron beam writing (electron beam lithography, e^- beam writing) with the use of a JEOL 840 Scanning Electron Microscope . Essentially, two reactions can possibly occur after irradiation of the positive photoresist with electrons from the SEM, first, the molecules of the resist (which is a polymer) may be cross-linked together to form one large molecule (essentially a thermoset polymer), thereby becoming a negative resist as opposed to remaining its original composition of a positive resist. This occurs if the resist is irradiated with to high of an energy dosage. Second, the molecules may be broken down to form smaller molecules, thus maintaining the capability as a positive resist. The exposure index required for writing with SPM can be determined as the product of the beam current i, line time t (i.e. exposure time), and the magnification setting, M (see equation 21) [62].

$$\text{Exposure index} = i\ M\ t \quad \text{(coulombs, C)} \tag{21}$$

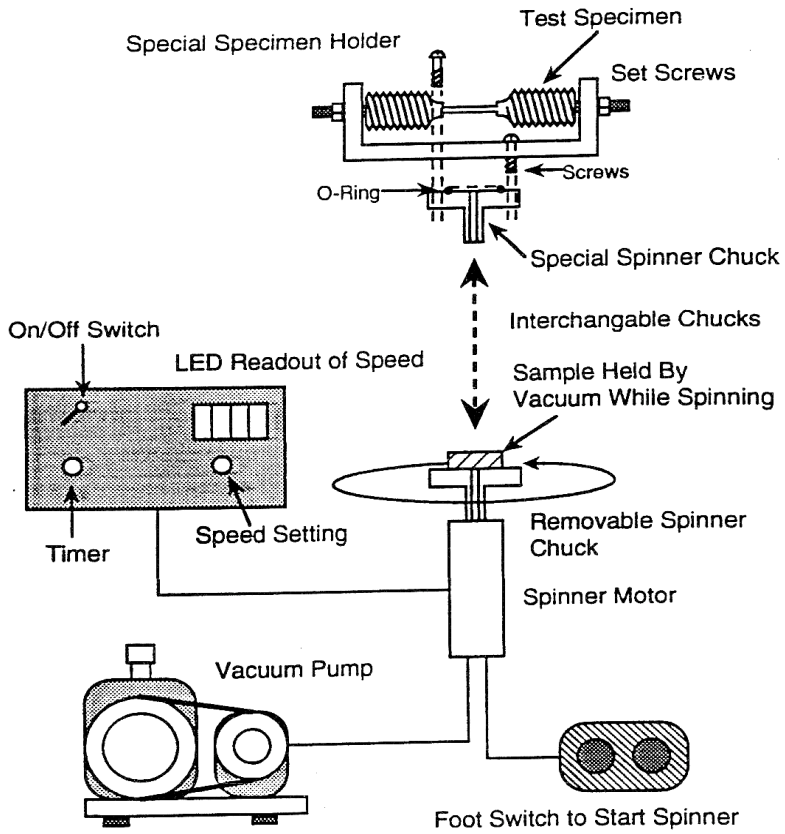

Figure 13 – Schematic of Vacuum Spin Coater for Resist Application [37]

During the grid-patterning portion of this process (photolithography), the SPM is essentially "tricked" into perceiving that it is performing a quantitative line analysis of the sample. Given this condition, the electron beam scans the sample along a straight line, providing that it does not rastor. (Rastoring occurs often during imaging analysis and typically results in thick, fuzzy lines. It is critical that the specimen is optically examined prior to development to ensure straight, clear lines.) As a result of the quantitative line analysis, the positive photoresist is exposed at several specific line intervals, which are predetermined and stored as a point table through the use of a computer program entitled PC Task. The first step in this process involves the development and storage of a set

of point tables, so they can be recalled whenever fiducial lines need to be drawn on a sample; this procedure only needs to be performed once. Development of point tables involves input values of x, y, and z coordinates of the reference starting point, the stop point and the total number of desired points. Entering the correct coordinate input values, the x and z coordinates are held constant and the y coordinate value increases by 20 μm with each increment. Thus, once the point tables are created, they only need to be recalled to draw a grid pattern (refer to references 37 and 38 for specific SPM grid pattern operation instructions). A dummy sample is used to obtain accurate electron beam writing conditions. This specimen is used to locate the center coordinates of the specimen and creation of the point tables. Accordingly, the dummy sample is also used to set the conditions for electron beam lithography, i.e. beam current, magnification, accelerating voltage, exposure time, these conditions effect the line resolution.

Once the conditions are optimized, the actual specimen is removed from the black film bag in complete darkness and is secured in the sample holder. The sample is placed in the specimen holder in darkness as a precautionary measure because the photoresist (resist) is sensitive to light for long periods of time. Once the sample is placed inside the instrument chamber the point tables are then executed by the computer program. The program automatically ensures that the lines are drawn according to point table set. During the line drawing process, the electron beam exposes the photoresist, when the stage moves from one point to the next point, the Faraday Cup blocks the beam. Once the lines are drawn in one direction, the sample is rotated 90° perpendicular to the initial drawn line set and the next set of lines are drawn which completes the grid pattern. When the

process is performed correctly, the resulting grid pattern should be a set of 150 x 150 lines at a distance of 20 μm apart and approximately 0.5 μm thick (see figure 15 for sample grid pattern).

Several parameters affect the quality of the lines drawn, in regards to the SPM instrument, these parameters include: accelerating voltage, the vacuum used, filament current, beam current, exposure time, magnification, and the objective aperture. In all cases, the accelerating voltage should be held constant at 30kV and optimum vacuum should be around 10^{-6} Torr (an even lower vacuum is optimal). Longer exposure times and higher beam current result in thicker grid lines. For example, an exposure time of approximately 10 seconds and a beam current of 0.6 nA, will result in grid lines that are approximately 4 μm thick. It should be noted that the length of the grid lines is determined by the magnification of the microscope on the instrument, i.e., as the magnification increases, the length of the lines decreases. A magnification of 12X produces lines approximately 6-8 μm long. See the table 6 for grid pattern conditions.

Table 6 – Grid Pattern Conditions

Accelerating Voltage (kV)	Beam Current (nA)	Exposure Time (sec)	Magnification	Aperture Size
30	0.5	7	100X	4

After resist exposure the sample is then baked in a vacuum furnace oven at a temperature of 393K (120ºC) for 20 minutes to harden the exposed resist (this step is called post exposure bake, or post bake). The sample is then cooled to room temperature and then developed. Prior to developing, the sample is optically inspected in a safelight optical microscope for clarity. Developing takes place in a clean room where there is no UV light. The sample is completely

immersed in MIBK:IPA (1:3) developer solution (this developer is specifically for PMMA positive photo-resist and is also supplied by MicroChem company) for 1 minute to develop the exposed resist. Since the resist used in this investigation is a positive resist, the exposed area of the resist dissolves immediately upon submersion in the solution. After developing, the sample is again optically inspected to ensure that the resist is completely developed; if not, the sample is immersed in developer for another 30 seconds and inspected again. Occasionally samples require longer development times, some samples in this study were developed for durations as long as 5 minutes. Longer developing times can be attributed to several factors, writing conditions (exposure conditions), resist deposition conditions, and age of resist. Once developed, the sample can be exposed to normal light. The grid quality is visually examined again under an optical microscope at a magnification of 10X for total cross-sectional area examination and a magnification of 100X for close visual inspection. When the lines drawn are too thick or too thin, or if the grid pattern is incomplete, the resist layer is removed by submersing the sample in Nano PG Remover (also supplied by the MicroChem company) for approximately a half hour and the entire procedure is repeated. There are occasions where 30 minutes is insufficient for complete resist removal, successful resist removals have been observed at time periods of 8 hours or more. If the grid is drawn as desired, the specimen is etched with dilute etchant (see table 7 for dilute etchant chemical composition) for 60 seconds and then rinsed in deionzed water. The purpose of etching is twofold, first, it enables for good adhesion of the metal deposited to the substrate surface, and second, it enables the easy removal of the resist easier after vacuum sputtering of the metal layer.

Table 7 – Dilute Titanium Etch Solution

Chemical	Amount
Water	194 ml
69-70% Nitric Acid (HNO_3)	4 ml
49% Hydrofluoric Acid (HF)	2 ml

The last step in this photolithographic process is to vacuum sputter coat the sample's surface a 50 nm layer of Gold-Palladium (Au-Pd) (refer to references 37 and 38 for vacuum sputter instrument operation). This Au-Pd layer adheres to the titanium substrate's exposed etched surface and the remaining resist. The sample is then submersed in Nano PG Remover for several hours (this can be as short as 30 minutes to as long as 10 days) after sputtering. The purpose of submersing the sample in Nano PG Remover at this juncture of the process is to strip the photo-resist, which leaves the grid pattern outlined in Au-Pd remaining on the titanium specimen. There are methods for faster resist removal such as using an ultrasonic agitator with resist remover, however, use of a sonicator for too long of a time period (> 2 minutes) can result in the complete removal of the grid pattern. Therefore, the sonicator was used in moderation when submersion in resist stripper for 10 days was insufficient. After the photoresist is completely stripped and the metallic grid pattern is left, the sample is then rinsed with deionized water and dried. At this point, the sample preparation is now complete and the result should yield Au-Pd grid lines approximately 0.5 μm thick and 20 μm apart on the titanium specimen surface (see figures 14 and 15 for photoresist application/photolithography procedure and example of final resist grid line pattern).

It should be noted that during the photolithographic process several challenges are faced in the successful development of a grid pattern on the specimen's flat surface. For example, if the energy, voltage condition of the instrument is too high, the result would cause the positive photo-resist to cross-link and therefore become a negative photo-resist, which would not develop successfully, or the resist would develop successfully, however, there would be poor metal adhesion and the entire grid pattern would completely lift off during the resist stripping process. Conversely if there is not enough energy during the resist exposure (i.e. line drawing portion), the entire grid pattern will completely lift off during resist stripping. Therefore, it is critical that there is sufficient energy to expose through the entire resist layer so that the metal deposited can adhere to the substrate's surface.

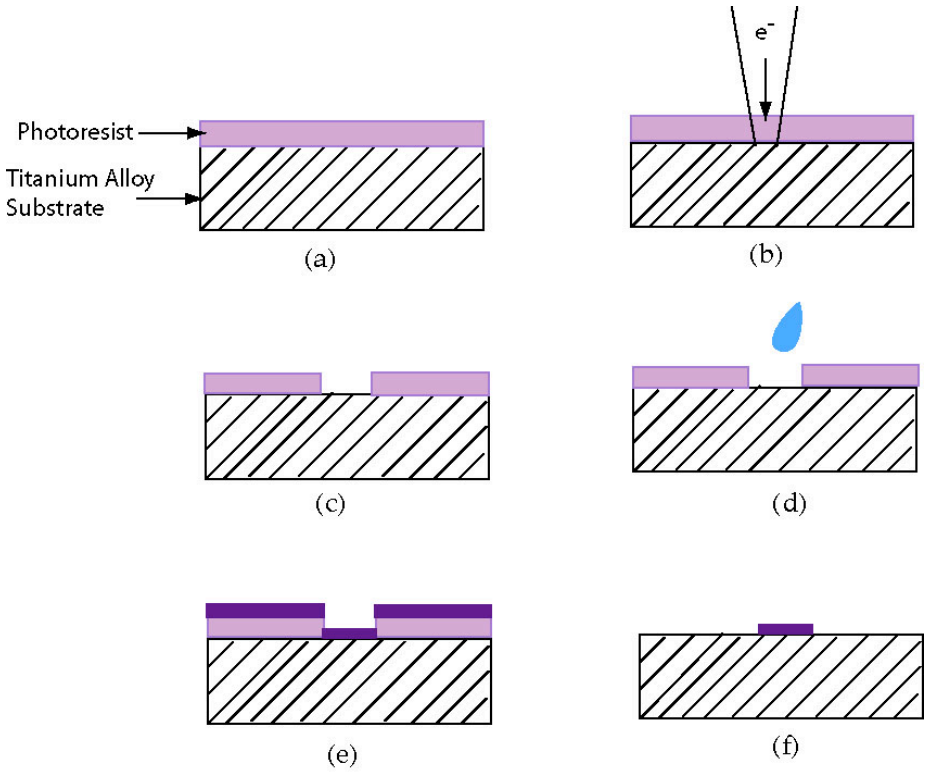

Figure 14 - Photoresist Application Process [62-66]: a) sample is spin coated with a layer of positive photoresist, b) grid lines are drawn with electron beam by SPM, c) sample is immersed in developer for removal of exposed photoresist, d) sample is etched with dilute etch e) surface is sputter coated with 50 nm of Au-Pd metal, f) remaining photoresist and deposited metal is stripped leaving resulting metal grid pattern.

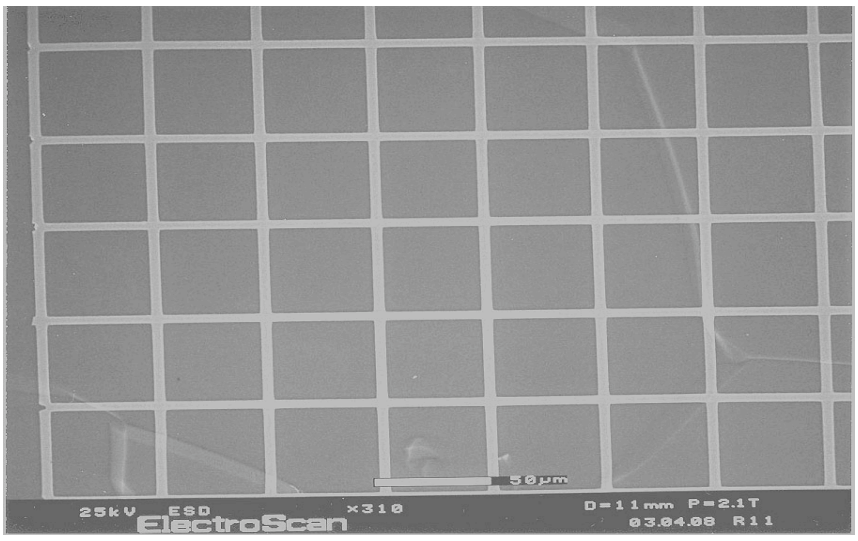

Figure 15 – Sample Grid Pattern

One issue faced during the photolithography process was poor development of the exposed resist. Underdevelopment of the resist can pose a challenge in adhesion of metal deposition after lift off. Successful etching after development of the exposed resist is also critical, if the exposed resist is not sufficiently etched, it is difficult for the metal to adhere, "stick" to the surface, which would also yield complete lift off during resist stripping. This therefore results in delamination of the Au-Pd metal layer, which occurred several times and the entire photolithographic process had to be repeated. Other issues faced with the grid pattern in this study included the disappearance of the grid pattern during creep testing (which was performed at elevated temperatures, to be discussed in the subsequent discussion of results section), which may have had some adverse effect on testing results, including measurement issues.

Mechanical Testing

Tensile Testing

Tensile tests were performed in vacuum at five test temperatures 298 K (25°C), 338 K (65°C), 378K (105°C), 418K (145°C), and 458 K (185°C) for determination of respective yield strength (YS) values for subsequent creep testing. The YS was determined from 0.2% proof stress of the resulting stress versus strain plot, since there was not a sharp yield point. A Materials Research Furnace (MRF) floor model Instron type instrument was used for variant temperature tensile tests**.** Tensile tests were conducted in vacuum at a constant strain rate of 3.28×10^{-5}/sec at 298K (25°C), 2.36×10^{-5}/sec at 338K (65°C), 2.58×10^{-5}/sec at 378K (105°C), 418K (145°C) and 458K (185°C); all samples were strained to a maximum strain of 3% and then unloaded (see chapter 4 for resulting strain-

strain plots). One sample each was used as they were only strained to 3% and were not strained to failure, there was no reduction in cross-sectional area or necking. The decrease in strain rates for each increased temperature is due to the increased ductility of the material at elevated temperature. Samples were heated for a period of at least 90 minutes or more prior to actual testing at test temperatures 378-418K (105-185°C) to ensure that specimen was at the actual test temperature.

Creep Testing

Creep Furnace Assembly, Set Up, Furnace Calibration

An Applied Test Systems (ATS) series 2330 creep instrument, with a lever arm ratio of 20:1 rated at 20,000 lbs, with a creep furnace for variant temperature creep testing. A series 3210 split tube furnace with a series 3910 retort assembly for controlled gas environment was installed in the center of the existing ATS creep tester frame with bracket attachments (see figures 17 - 19). Heating elements were aligned in series inside the split tube furnace to prevent shorting during furnace heating [67]. Power was supplied to the creep furnace directly from a direct current terminal source block; both the furnace and control system panels were grounded and wired according to national and local FCC electrical code requirements (208/240V). Temperature measurements of the split tube furnace were made with the use of K type thermocouples.

Prior to initial operation of the creep tester with the attached split tube furnace, a "bake-out" procedure must be performed on the creep furnace. The purpose of the bake out process is to eliminate any traces of water vapor contained with the furnace prior to actual operation of the unit. This bake-out

process consists of initially heating the furnace to a temperature 478K (205°C) for approximately 2 hours until virtually all traces of water vapor and gases are removed. Once all traces of water vapor and gases were dissipated, the furnace temperature was increased to 810K (537°C) and continued to bake until both the smoke and odor were eliminated from the furnace. The temperature was then increased to the maximum furnace operating temperature of 1373K (1100°C), once the set temperature was reached (this took 6.5 hours), the power was then turned off and the furnace was cooled for 24 hours. After the bake-out procedure, a Series 3910 Inconel Retort with cross type accessory chamber and bellows type pull rod seal, was positioned inside the split tube furnace against the heating elements (see figures 16 and 18 for retort design and position assembly). The purpose of the retort is to test specimens in a controlled enclosed gas atmosphere (in this study Argon (Ar) gas was used).

Swagelok stainless steel hosing and fittings were attached to the creep furnace for water flow throughout the creep furnace. Rubber hosing was used for the incoming and exit water flow from the furnace, which was attached with the use of Swagelok stainless steel fittings. A Swagelok turn control valve was attached to the incoming water line for control of water flow to the "water cooled" pull-rods (see figure 17 for diagram of water flow). The purpose of the water supply is to cool the "water-cooled" pull-rods, which consists of bellows for strain displacement and contains the linear voltage capacitor (LVC) transducer during creep testing (see figure 19 for water cool pull rod assembly). Swagelok fittings were also attached to the inlets and outlets of the side and top of the furnace for incoming and exit of gas to the retort of the furnace; rubber hosing was used for the gas line.

Several challenges were encountered during the installation of the water and gas lines of the creep furnace. Some of the major challenges faced involved obtaining proper fittings from the water source to the hose attachment, fittings from the water hose to the incoming water port of the creep furnace, fittings from the exiting steel water hose to return water hose, fittings for incoming and exit of gas line, as well as the design and installation of the exit gas line to the exhaust fume hood. All fittings, with the exception of the fitting that was directly attached to the water source, were stainless-steel Swagelok fittings which were 1/4 inch unions, elbows, water valves, and reducers (reducers were used for attachments from the incoming water hose to the incoming water port of the furnace and for the exit stainless steel water hose to the return water flow rubber hose). In addition, a water control regulator was attached to the bottom portion of the water cool rod to control the incoming water flow.

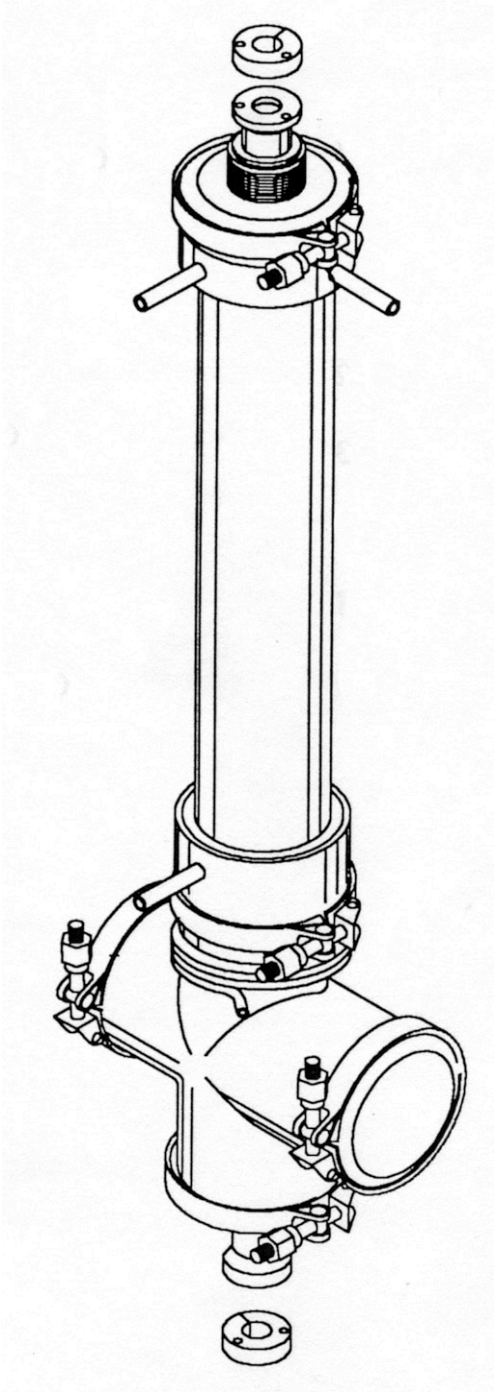

Figure 16 – Applied Test System Series 3910 retort chamber assembly design for controlled gas contained atmospheric conditions [67].

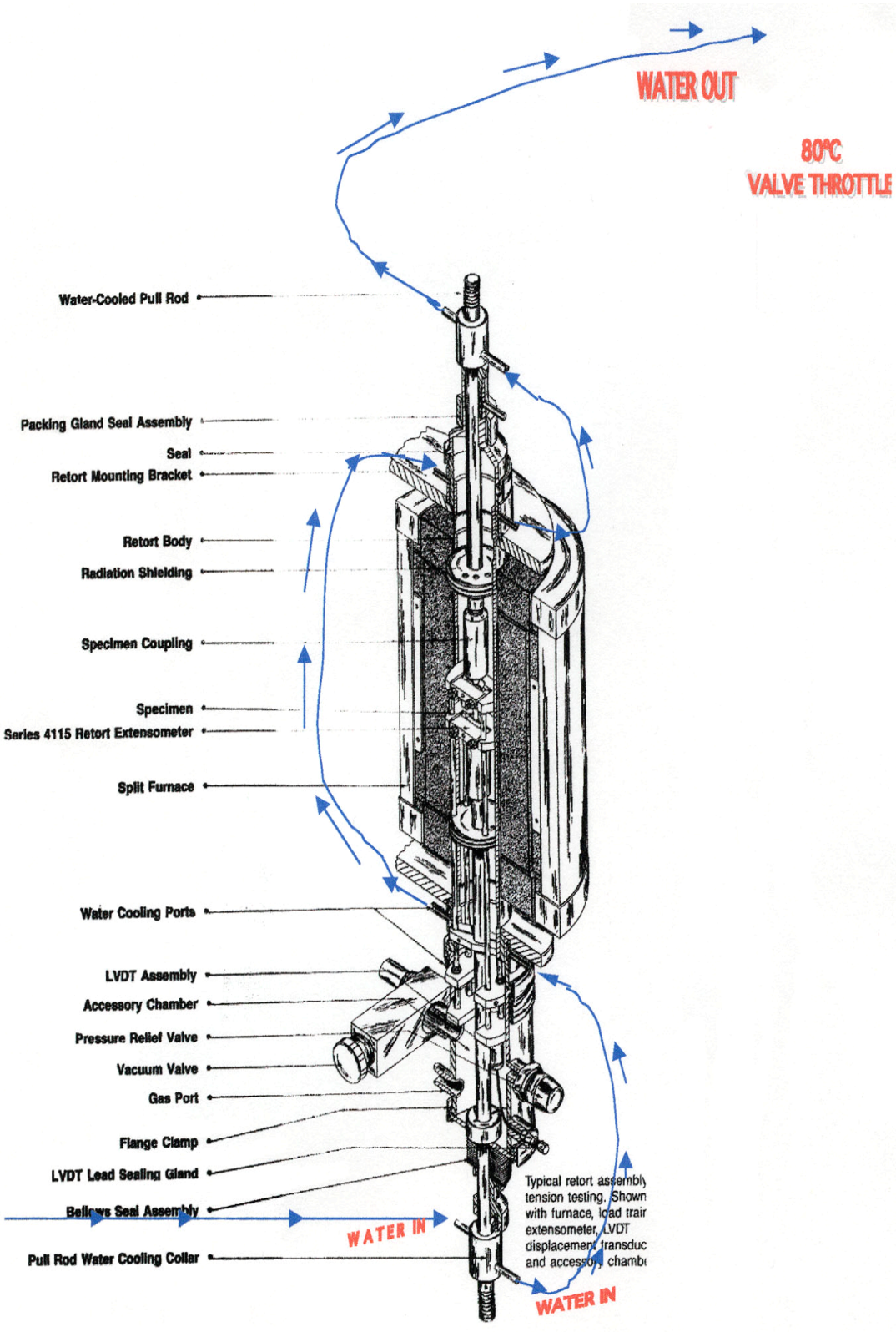

Figure 17 – Creep Furnace Assembly [67]

1. Retort tube subassembly
2. Extensometer chamber
3. Upper bellows assembly
4. Lower bellows assembly
5. Upper water cooled pull rod
6. Lower water cooled pull rod
7. Cap
8. Upper radiation shield
9. Lower radiation shield
10. Inconel clip
11. Water coupling
12. Retort clamp
13. Gasket (Viton)
14. Extensometer Assy.
15. Split collar
16. Thermocouple gland
17. Sealant
18. LVDT wiring connection
19. Coupling
20. Collar
21. Retort mounting bracket
22. Vacuum valve
23. Tube

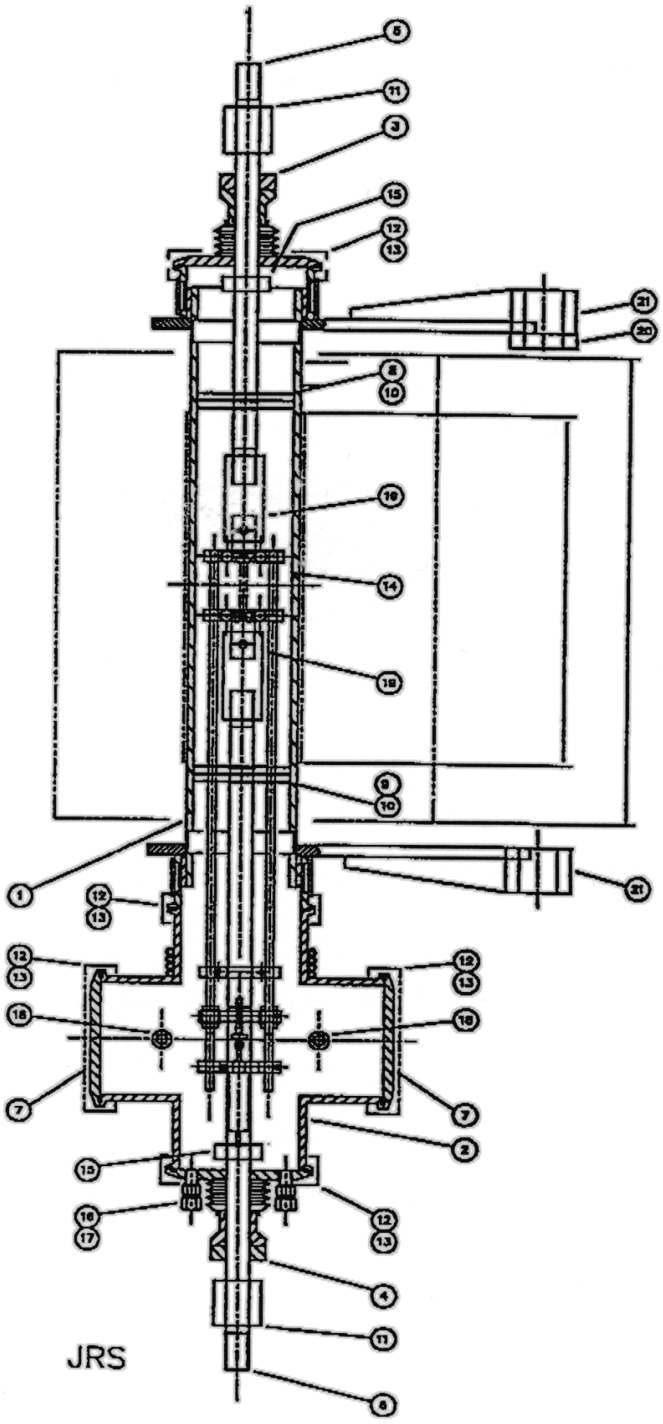

Figure 18 – Schematic of retort assembly, creep furnace and specimen with attached extensometer positioned inside furnace heat zone [67]

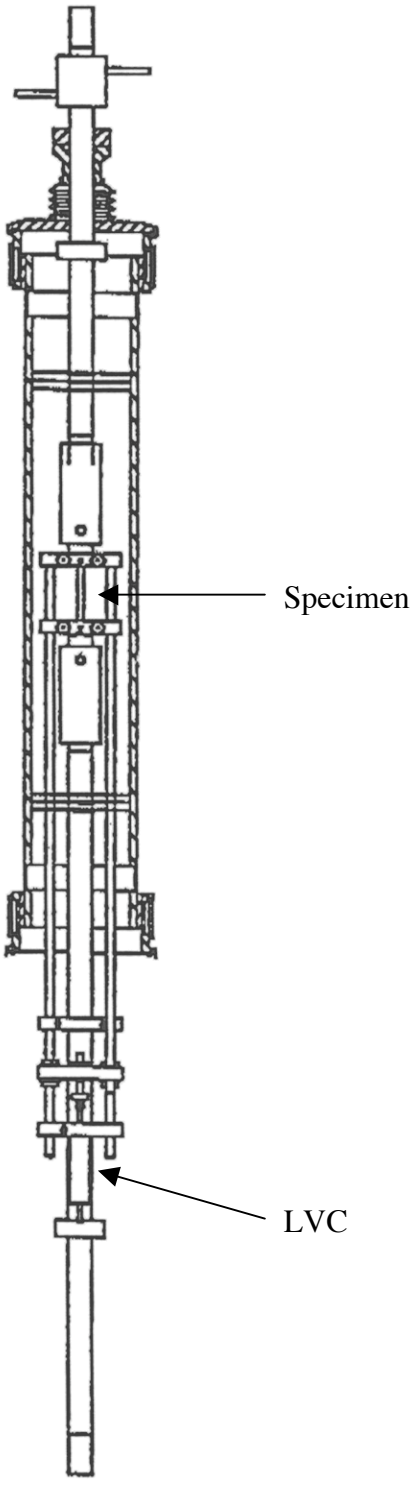

Figure 19 – Schematic of extensometer and water cool pull rod assembly for specimen positioning [67].

Prior to actual experimental operation, the creep furnace must be calibrated to ensure that it is actually operating at the temperature set on the temperature control panel. Calibration of the creep furnace is performed through a procedure termed as "autotuning." This procedure involves operation of the creep furnace in "auto" mode, setting the desired operation temperature in the home menu and then selecting "tune on" from the "Atun List" menu. At this juncture, the control unit will cycle through a series of calibrations above and below the set operation temperature until the furnace is calibrated to operate efficiently at the specified set temperature. The autotuning process may last for a period of 5 to 7 hours or more depending on the desired testing temperature. It is imperative that the furnace is autotuned (calibrated) for each testing temperature, so as to ensure accuracy in the heating of the furnace. Therefore for 4 test operating temperatures the autotune procedure can last any where from 20 to 28 hours.

One challenge experienced during the autotuning process was that the furnace temperature increased rapidly to a temperature of 200 degrees higher than the desired operating temperature. The Pid settings were adjusted which alleviated the overshoot of temperature issue; see table 8 for ideal furnace Pid settings. Another challenge that can also be faced during autotuning of furnace test temperatures is when adjustment of Pid settings does not stop the temperature overshoot issue. When this occurs an amp meter/volt meter must be used to determine if or where there is a current leak; i.e. the bias is set too high for the control panel. The volt-meter is clipped onto the back of the control panel unit and the current is decreased until the output voltage reads 5 volts on the meter.

Table 8 – Ideal Furnace PiD Settings

Pb	36	**t_1**	10.7
td	OFF	**rE5**	0.0
Hcb	Auto	**Lcb**	Auto

Pb – Proportional Band, this is the bandwidth in display units over which the output power is proportioned between minimum and maximum power output.

td – Derivative time in seconds, this determines how strongly the controller will react to the rate of change in the measured value (i.e. measured temperature).

t1 – Integral time in seconds, this determines the time taken by the controller to remove the steady-state error signals.

rE5 – Manual Reset (%), this the percentage value to which a manual reset is made.

Hcb – Cutback High, this is the number of display units, above the setpoint (set temperature value), at which the controller will increase the output power, in order to prevent overshoot on cool down of furnace (if a temperature program is set).

Lcb – Cutback Low, this is the of display units, below the setpoint (set temperature value), at which the controller will cutback the output power, in order to prevent overshoot on heat up.

rEL – this parameter is only present if a temperature heating and cooling program has been programmed/configured in the control unit. This parameter sets the cooling proportional band, which equals the Pb value divided by the rEL value.

Although the split tube creep furnace operates at the temperature set on the control unit, there is however, a significant temperature difference between the furnace operating temperature and the actual creep specimen's temperature. This large temperature difference between the temperature displayed on the control panel unit for the furnace and the actual sample temperature is primarily due to the distance between the retort, which sits inside of the ceramic heating elements of the furnace (see figures 18 and 20 for retort positioning and furnace heat zone) and the specimen. Therefore, it is necessary to measure the actual temperature of the creep sample through the use of a thermocouple to ensure that the specimen is actually tested at the desired temperature. A 'K' type thermocouple was affixed to a "dummy" test creep sample for determination of actual respective creep test temperatures. The thermocouple is attached to the dummy test specimen and the leads are draw through the holes of the optional ports of the bellow water cool pull rod assembly, which holds the test specimen and is connected to the thermocouple temperature meter (see figure 21 for diagram of optional ports used for thermocouple placement). The difference between the furnace operating temperature and specimen temperature is outlined in table 9. As one can observe in table 9, there is a 40 degree temperature difference between the temperature set on the control panel unit and the actual specimen temperature. Although the specimen is placed within the heat zone of the furnace, this large temperature difference between the actual furnace operating temperature and specimen temperature is due to the distance between specimen inside the retort and the ceramic heating elements of the furnace. Note, the specimen must be heated for a period of at least 5-8 hours

before actual creep testing, to ensure that the test is performed at the actual desired testing temperature.

Table 9 – Sample Test Temperatures

Furnace Temperature	Specimen Temperature
105ºC	65ºC
145ºC	105ºC
205ºC	145ºC
245ºC	185ºC

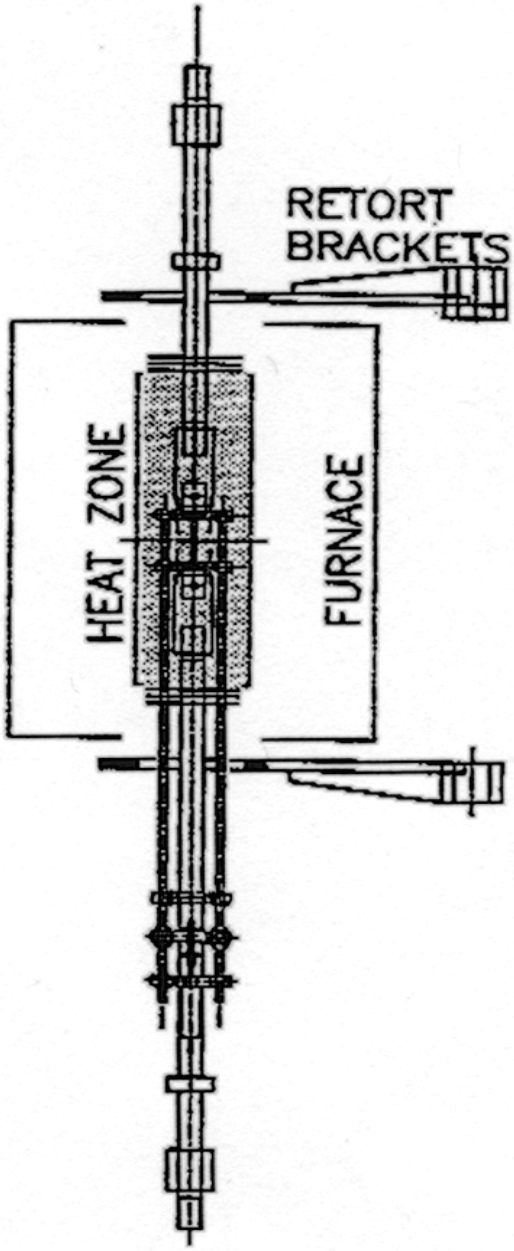

Figure 20 – Schematic of Furnace Heat Zone [67]

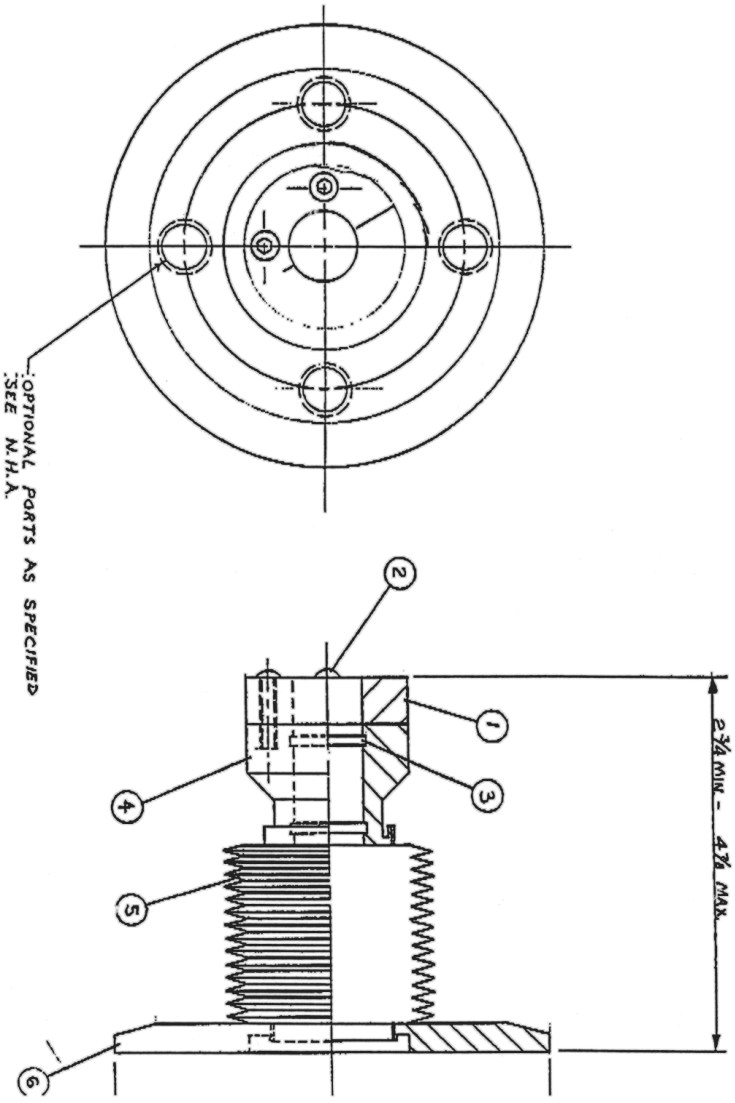

Figure 21 – Schematic of optional port openings [67]. The ports are used for drawing of thermocouple lines for measurement of sample temperature. These ports are later plugged for controlled gas environment testing.

Data Acquisition Calibration and Continuous Creep Tests

Transducer Calibration

Data acquisition was conducted with the assistance of an Analog/Digital (A/D) board and data acquisition software; both of which were supplied by Strawberry Tree, Incorporated. Strain is measured with the use of an extensometer consisting of a linear voltage capacitor (LVC) transducer, which was supplied by ATS (see figures 17 -19 for position of LVC on the extensometer containing test specimen). The LVC is connected to modules that supply a voltage between 0 and 10 volts to the A/D board corresponding the strain incurred during testing. This voltage serves as the input to the corresponding Quicklog PC data acquisition software, which is an interactive tool that operates on the computer. The data output is directly in the form of percent strain. A graphical plot is generated with the strain plotted against time.

Prior to loading the sample for creep testing, it is necessary to calibrate the LVC transducer. A digital calibrator supplied by Epsilon Technologies was used for calibration. Calibration essentially involves applying a known strain to the transducer with the assistance of the calibrator and adjusting the constants a, b, and c in the equation of the following form:

$$\varepsilon = aX + bY + c \tag{22}$$

where: X = input from the A/D board

Y = invalid input and is equal to 0 (there is only displacement in one direction)

c = a constant to be adjusted depending on the error in the reading of the strain by the transducer

ε = strain which equals the reading shown by the calibrator in %

The value of 'c' is adjusted when there is no strain on the transducer and the module reading is set to zero. In this case, if the computer shows a non-zero value, the value of 'c' is adjusted to bring the displayed value to zero. Strain is imparted in steps and a value of 'a' is obtained. It is advisable to stay within the range of expected deformation for accurate calibration. The fit between the module value and strain is assumed to be a linear one, which holds true in actual testing. All calibration is performed on a gauge length of 1 inch.

As mentioned previously the extensometer is attached to flats (both the top and bottom) of the test specimen with a LVC transducer positioned within it for strain measurement. The LVC transducer is attached within the extensometer for measurement of strain displacement. See figures 17-19 and for positioning of extensometer and sample within the creep furnace and water cooled pull rods.

Creep tests were performed at various temperatures in an Ar atmosphere for 200 hours at 95% yield stress which was obtained from tensile tests conducted for the following temperatures: 298 K (25°C), 338 K (65°C), 378K (105°C), 418 K (145°C), and 458 K (185°C). As mentioned previously, an ATS series 2330 20:1 lever arm ratio creep tester consisting of an ATS series 3210 split tube furnace and series 3910 Inconel retort attachments were used for this investigation. Prior to actual creep testing, the retort chamber is purged with Argon gas for 3 hours. Immediately following the gas purge the creep furnace is heated for a period of 5-8 hours (depending on temperature) to ensure that the test specimen is heated to actual test temperature. The goal of performing creep testing at various temperatures in an Ar atmosphere is to determine the activation energy responsible for creep deformation, as well as observation of deformation modes responsible for creep behavior in a beta phase titanium alloy, Ti-14.8V. After the

first 8 - 11 hours of initial sample preparation, the load is applied to the weight pan. The first 72 hours of the creep test are critical as various parameters must be closely monitored to ensure continuous testing conditions. The weight pan must be closely monitored to ensure that the loading is directly applied to the specimen and does not touch the weight elevator, also to ensure that the lever arm is straight. The temperature control panel should be monitored every hour during the first 36 hours of testing to ensure that it does not overshoot and then every 8 hours. The Ar gas cylinder must be changed after every 96 hours. In addition, the data acquisition rate is changed after the first ten minutes, then thirty minutes, followed by two hours and five hours later during the first 7 hours of actual creep testing (to be detailed in the subsequent paragraph). Each creep test last for 200 hours, not including the initial preparation time (i.e. initial heating and gas purging) and the cooling recovery time.

Constant stress conditions were assumed, as the strain magnitude is expected to be small based on previous ambient temperature creep investigations performed on Ti-14.8V [8,10,37]; therefore, there should be negligible reduction in the specimen's cross sectional area. Based on the YS value obtained from tensile tests, the weight (in pounds, lb) to be placed on the creep instrument (i.e., the pan of the lever arm tester) is calculated from the following equation:

$$W = \frac{S \times A}{R} \tag{23}$$

where W – is the weight to be applied in lb

S – is 95% of the yield stress value

A – the measured cross sectional area of the specimen

R – is the lever arm ratio

Data was logged at different intervals depending on the stage of the creep test. Data was acquired according to the following intervals:

i. Loading/Unloading: 1 point per 100 ms for a duration of 10 minutes

ii. From Loading point until half hour later: 1 point per 1 second

iii. Two hours later: 1 point every 10 seconds

iv. Five hours later: 1 point every 1 minute

v. Remainder of test: 1 point every 20 minutes

vi. Recovery of sample after unloading: 1 point every 100 ms

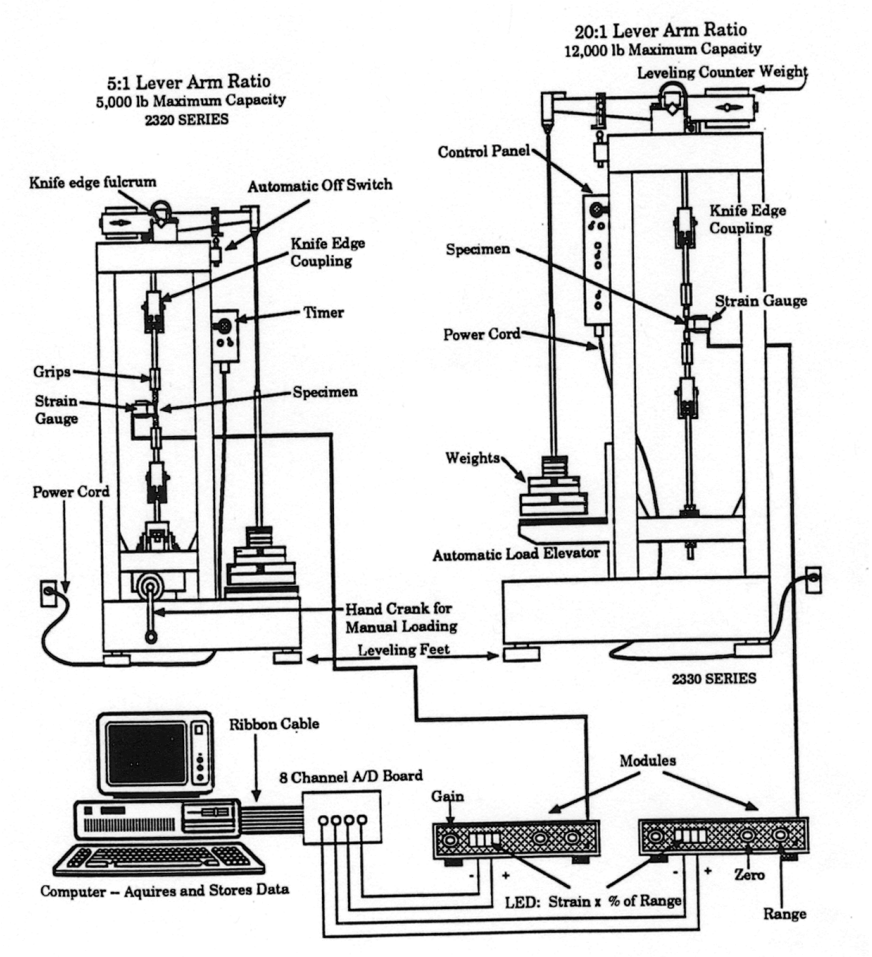

Figure 22 - Set up of Creep Instrument and Data Acquisition [61]

Characterization

Optical Microscopy

Samples were imaged before and after deformation by optical microscopy. Images were taken before deformation (i.e. prior to creep testing) for recording of initial grain boundary locations, as well as after deformation (298K, 338K, 378K, 418K, 458K) for observation of creep deformation mechanisms such as slip lines. As mentioned previously, samples were optically inspected during photolithography for set up of line drawing conditions and to ensure successful grid patterning. Specimens were best observed at a magnification of 10X for large area observations and at 100X for close range (specific grain) visual inspection. Optical imaging was performed with the assistance of a Nikon Opto Megapics Digital Camera attached to a standard laboratory microscope. Images were recorded on a memory stick as JPEG files, which were later transferred to a standard PC computer and saved. Effective optical imaging of specific areas before and after deformation is quite time consuming and can take up to a minimum of 25 hours to image one side of a specimen. Optical imaging of 5 samples can take approximately 125 hours or more.

Scanning Electron Microscopy (SEM)

Samples were imaged by environmental scanning electron microscopy (E3 ESEM) before and after deformation for observation of low temperature creep deformation mechanisms. Samples were imaged by ESEM after etching (prior to grid application), as well as after grid attachment. As stated earlier, the goal of the attached fiducial grid is to reference specific grain boundaries, surface areas prior to deformation, thus, various grid areas were photographed before creep

testing. Accordingly, images were taken of the same area after creep testing (after deformation) therefore, the grid pattern is quite useful in locating the specific areas where images were initially taken. Some grid patterns disappeared after testing on some samples which made imaging quite challenging. Consequently, images were taken of the entire sample area and later matched according to grain structure shape (grain boundary shape).

ESEM imaging conditions consisted of accelerating voltages of 25 kV and 30 kV and magnifications of 500X and 1000X. ESEM was utilized because of its simplistic operation and picture quality were better than on the SEM, particularly since the humidity in the ESEM neutralizes the net charge surrounding the specimen's surface, therefore reducing contamination with carbon particles. Furthermore, images obtained through the use of the ESEM are not fuzzy or grainy due to vacuum fluctuations or carbon particle contamination like the SEM. An additional advantage to the use of the ESEM is the ability to focus rather easily unlike the SEM. Also with the recent image data acquisition program attached to the ESEM, digital images were obtained and saved as JPEG files on a PC computer (refer to reference D for specific ESEM operation instructions).

The specimen's features are revealed by ESEM by scattering of electrons; stronger features scatter more electrons and therefore appear brighter than less pronounced features. Pit features accumulate electrons and therefore appear brighter than the rest of the substrate surface; slip lines and grain boundaries are elevated higher than the rest of the material and also appear lighter in the image. Contrast is achieved as a result of the height differences in the respective grains on the sample's surface, as well as differences in the orientation of the

neighboring grains, both of these conditions affect the electron scattering intensity. Given these parameters it is quite a challenge to achieve a high image quality by ESEM (as well as SEM). Moreover, like optical imaging, imaging by ESEM is quite time consuming and takes at least 25 hours to effectively image one specimen's side; thus, imaging of 5 samples takes a minimum of 125 hours.

Transmission Electron Microscopy (TEM)

To effectively study the low temperature deformation mechanisms in the nanometer range, thin foil specimens were made from deformed 350 μm grain sized Ti-14.8V samples according to the method outlined by Spurling for observation by transmission electron microscopy (TEM) [68]. Deformed specimens were made from the gauge cross-sections of the sample, perpendicular to the applied longitudinal loading direction. Undeformed specimens were made from the threaded regions of the test samples, as these areas were held static in the instrument grips and were not subjected to direct loading, the gauge sections were subjected to loading. Initial thin slices, ~1.57 x 10^{-4} mm (0.004 inches) thick were cut using a Buehler low speed wafering diamond blade saw (Buehler Isocutting Fluid oil was used for lubrication during cutting). Cutting a specimen takes a considerable amount of time, as titanium is an extremely hard metal, therefore a speed of approximately 100 rpm is best so as to not damage the diamond blade or induced additional residual stresses to the foil specimen. This process takes about 4-6 hours (8+ when making initial cut of specimen), noting that cutting the first piece takes twice as long as the specimen must be cut in half first. 3 mm diameter discs were punched from slices using a punch seal and then dimpled grinded to a thickness of ~$3.15x10^{-5}$

mm (0.0008 inches) using a South Bay Technologies 515 Dimple Grinder. Diamond paste (also supplied by South Bay Technologies) suspended in water consisting of grit sizes of 15, 6, and 3 μm was used for thinning the cross section. The specimen was then cryogenically jet polished at ~ 223K (-50°C) in a solution consisting of 5% sulfuric acid (H_2SO_4) and 95% methanol at a current of 30 mA with a corresponding voltage range of 50-60A for 10-30 seconds. Cryogenic temperatures were also maintained like the electropolishing conditions using methanol and dry ice in the surrounding bath. Continuous visual inspections were made of the sample by reflecting light on the surface; jet polishing was continued until a pin size hole was observed (respective thickness is approximately 10-50 μm). Jet polishing alone was not sufficient enough to yield a sample thin enough to observe by TEM, therefore, ion milling was utilized to thin the sample down. The optimum gun voltage and current ion mill conditions were 3.5 kV and 1.5 mA respectively and an angle of 30° yielded best results. Depending on the sample's initial thickness ion milling of one sample can take as short as 2 hours to as long as 8 hours (or more) to have a large cross sectional area sufficiently thin enough for TEM observation.

Both a Hitachi 600AB 100kV and JEOL 4000FX 300kV transmission electron microscopes were used for examining resulting foils; bright field, dark field images, and selected area diffraction (SAD) patterns were taken of significant features (discrete ω phase particles, β phase matrix and deformation products). Diffraction patterns were indexed through the use of Wulff net stereographic projections, methods outlined by Williams and Carter [69], as well as various papers on the nature of deformation products observed in β Ti alloys.

<110> patterns were taken of the undeformed matrix. Both {110} and {113} type diffraction patterns were taken of the deformed matrix. Obtained experimental results are given in the following chapter 4.

CHAPTER 4

EXPERIMENTAL RESULTS

Tensile Testing Results

One sample each of 350 μm grain sized beta phase Ti-14.8Wt%V alloy was tensile tested in vacuum at five test temperatures. As detailed in chapter 3, since there is no necking or extreme deformation to the naked eye, one sample was subjected to tensile testing at five test temperatures, strained at a constant strain rate of three percent and then unloaded; necking was not observed in any of the samples. One sample was tested at 298K (25ºC) at a constant strain rate of 3.28 x 10^{-5}/sec, one sample was tested at 338K (65ºC) at a constant strain rate of 2.36x10^{-5}/sec, and one sample each was tested at a constant strain rate of 2.58x10^{-5}/sec at temperatures 378K (105ºC), 418K (145ºC) and 458K (185ºC) respectively. Since the resulting engineering stress versus strain curves did not display a sharp yield point, the yield stress (YS) values for each test were determined at 0.2% of the proof stress value from the resulting plot.

It can be observed in the engineering stress versus engineering strain curve in figure 23 and in the true stress versus true strain curve displayed in figure 24, that stress decreases with the increase in temperature. This decrease can be attributed to the ductility in the heated sample material. The sample tested at 458K fractured before reaching three percent strain, however, the resulting curve was sufficient enough to obtain the YS value at 0.2 percent of the curve. The YS values were determined as the following: 733.21 MPa for 298K, 690.675 MPa for 338K, 676.68 MPa for 378K, 627.51 MPa for 418K and 673.85 MPa

for 458K. Accordingly with the increase in temperature, the material is more ductile and the YS values decrease with the increase in temperature. With the exception of the curve for test temperature 458K, it can be observed that the resulting stress versus strain curves decrease with increasing temperatures for both engineering and true plots.

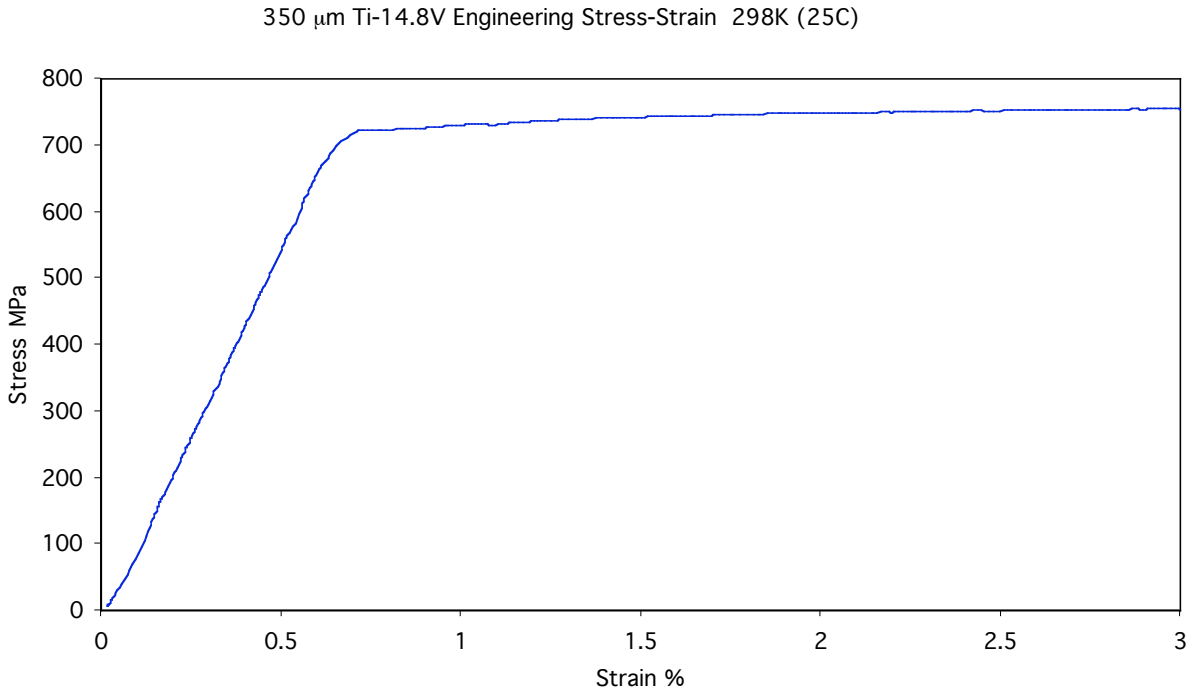

Figure 23 – Engineering Stress vs Strain Curve for 350 μm grain size Ti-14.8V alloy at 298K (25°C). Sample was strained to 3.0% at a strain rate of 3.128 x 10^{-5}/s, the 0.2% YS value is 733.21 MPa.

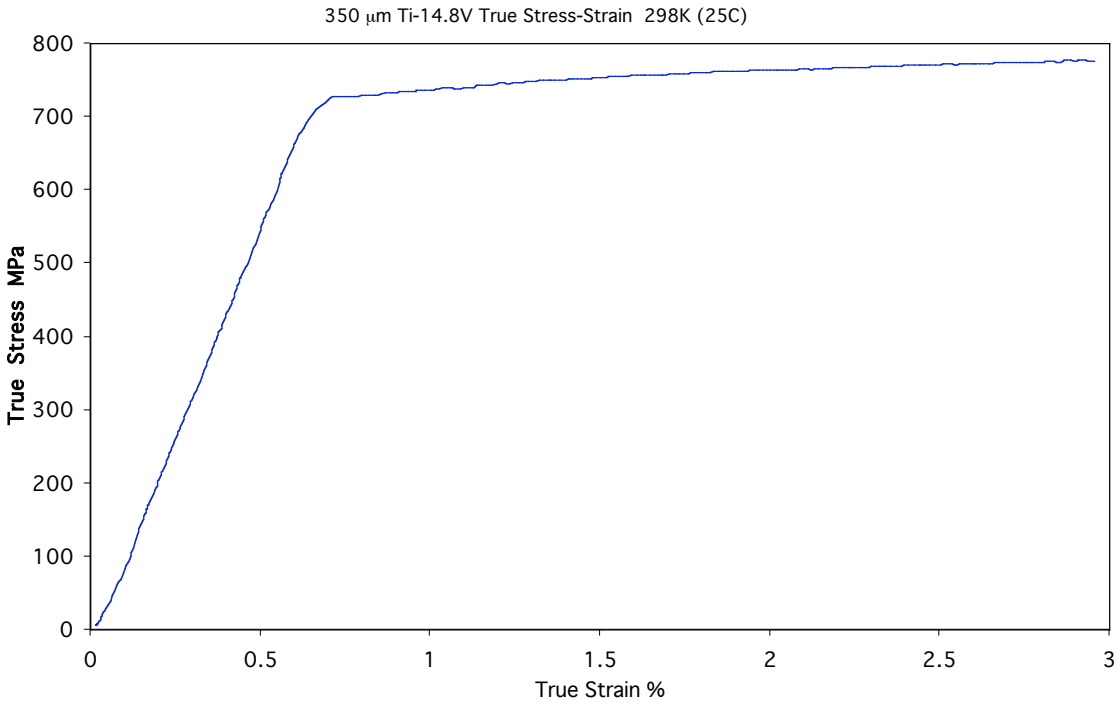

Figure 24 – True Stress vs. True Strain Curve for 350 μm Ti-14.8V at 298K

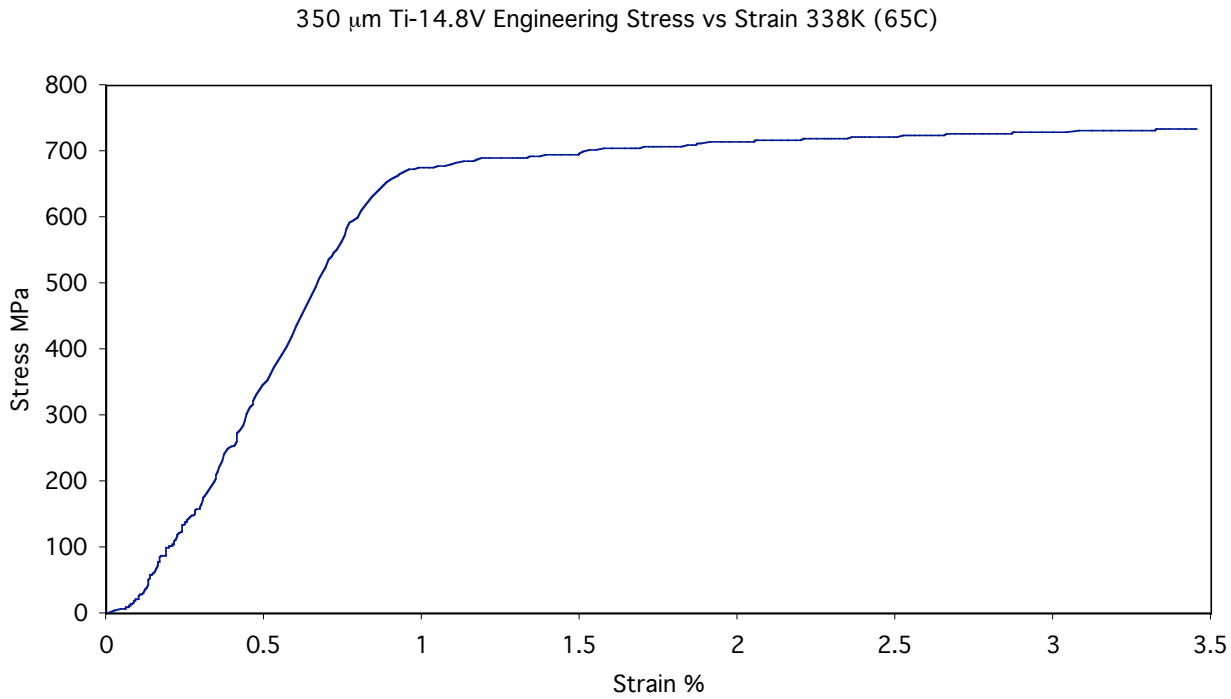

Figure 25 – Engineering Stress vs. Strain Curve for 350 μm grain size Ti-14.8V alloy at 338K (65°C). Sample was strained to 3.45% at a strain rate of 2.58 x 10^{-5}/s, the 0.2% YS value was 690.675 MPa

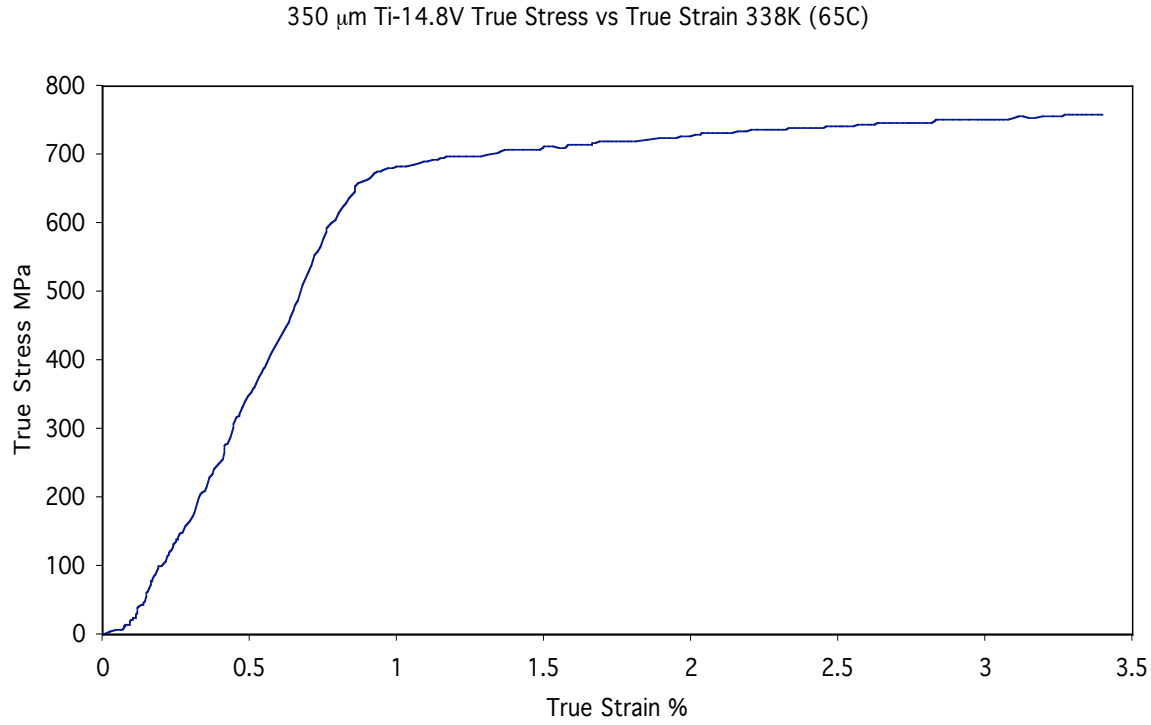

Figure 26 – True Stress vs. True Strain Curve for 350 μm Grain Size Ti-14.8V at 338K

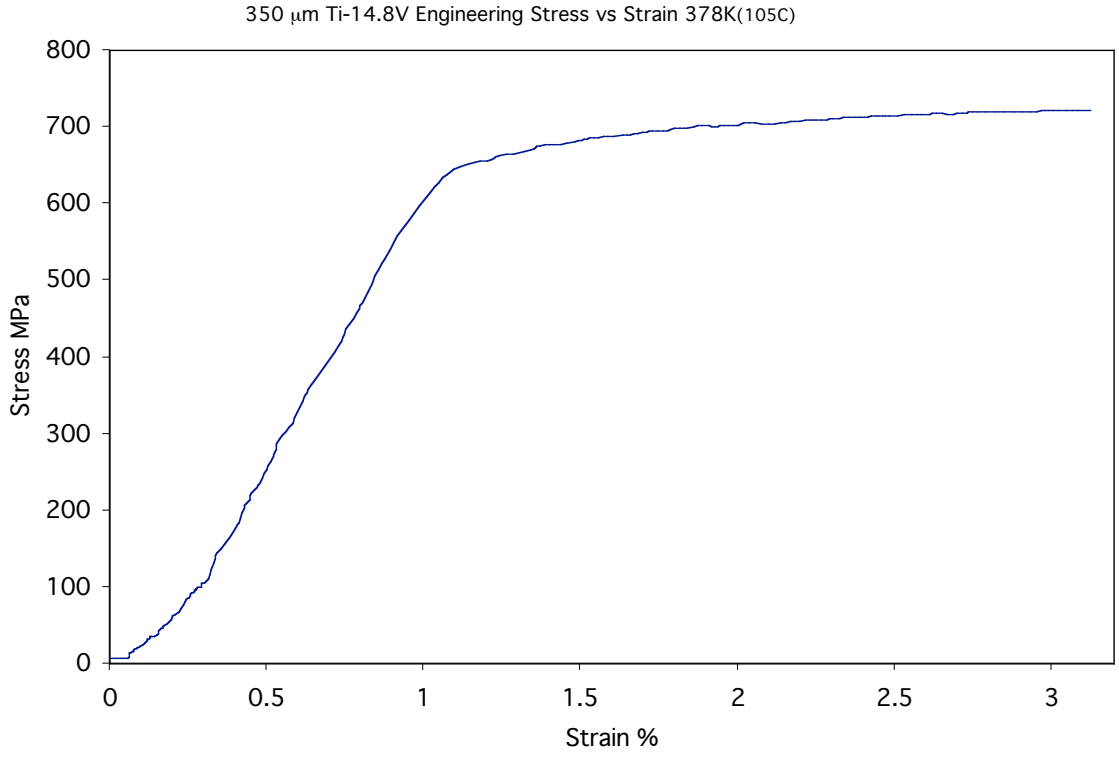

Figure 27 – Engineering Stress vs. Strain Curve for 350 μm Ti-14.8V at 378K (105°C). Sample was strained to 3.12% at a strain rate of 2.36×10^{-5}/s, the 0.2% YS value was 688.875 MPa.

Figure 28 – True Stress vs. True Strain curve for 350 μm Ti-14.8V 378K (105°C)

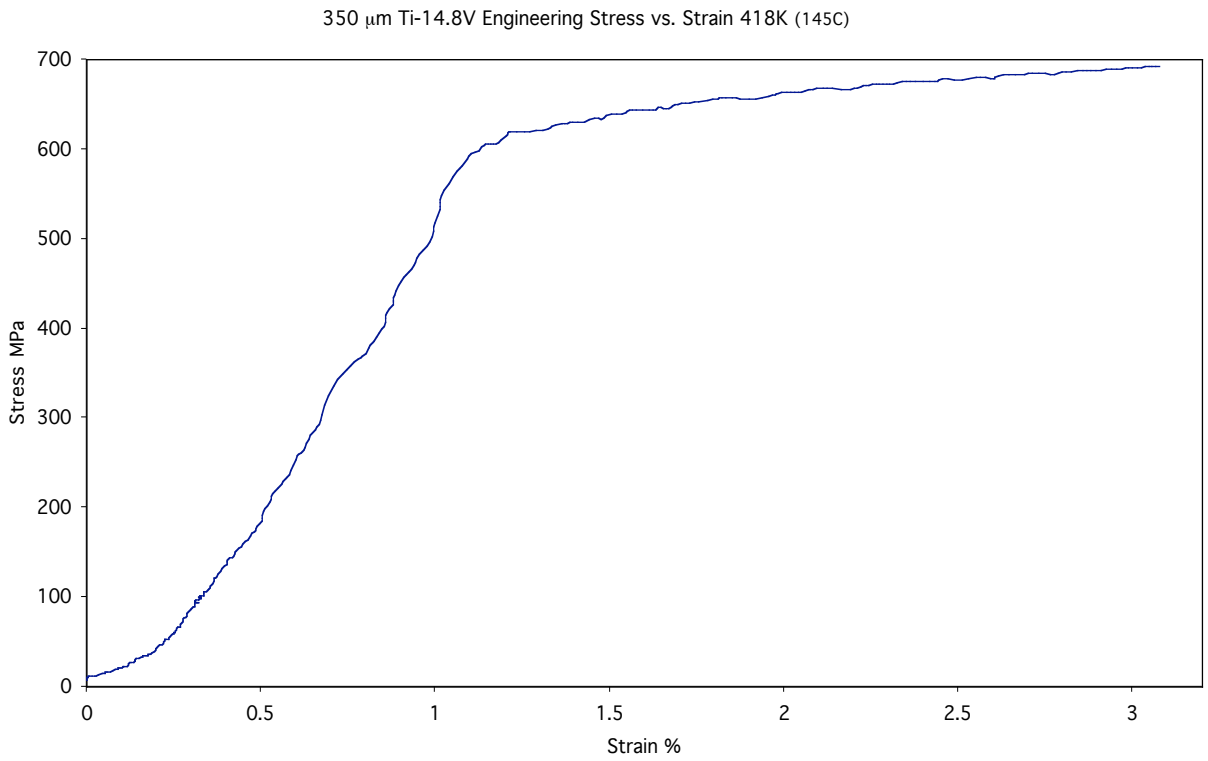

Figure 29 - Engineering Stress vs. Strain Curve 350 μm Ti-14.8V alloy at 418K (145°C). Sample was strained to 3.07% at a strain rate of 2.36×10^{-5}/s. The 0.2%YS value was 627.51 MPa.

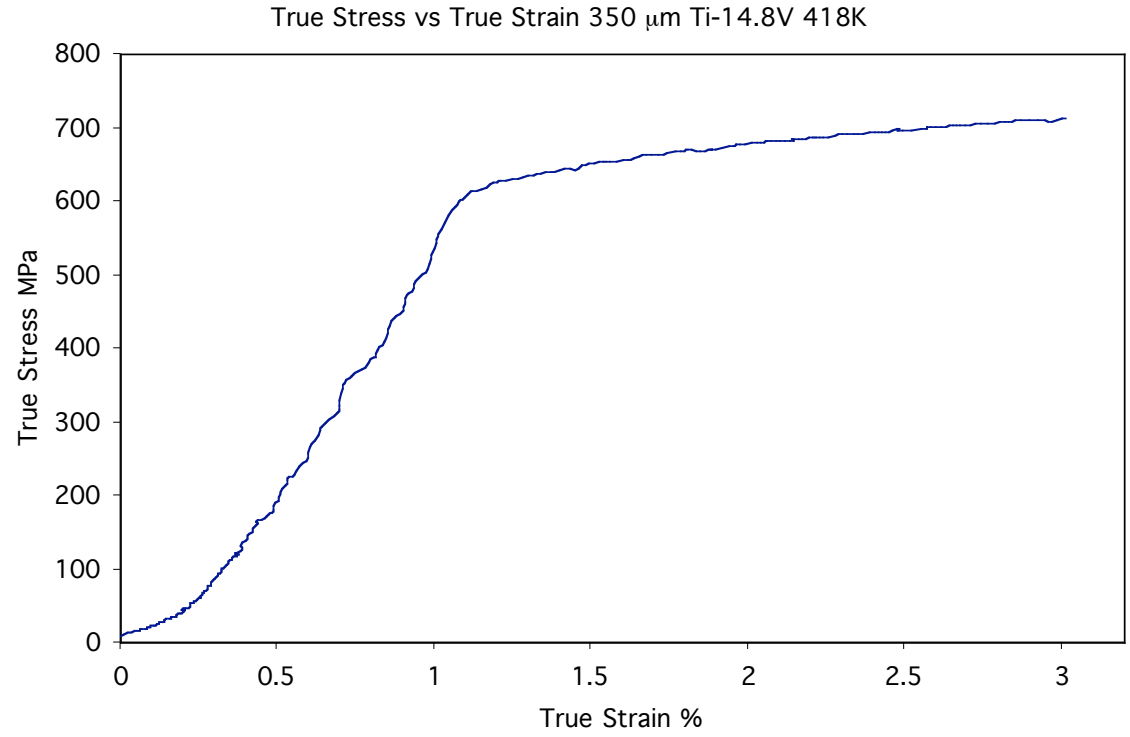

Figure 30 – True Stress vs. True Strain for 350 μm Ti-14.8V alloy at 418K

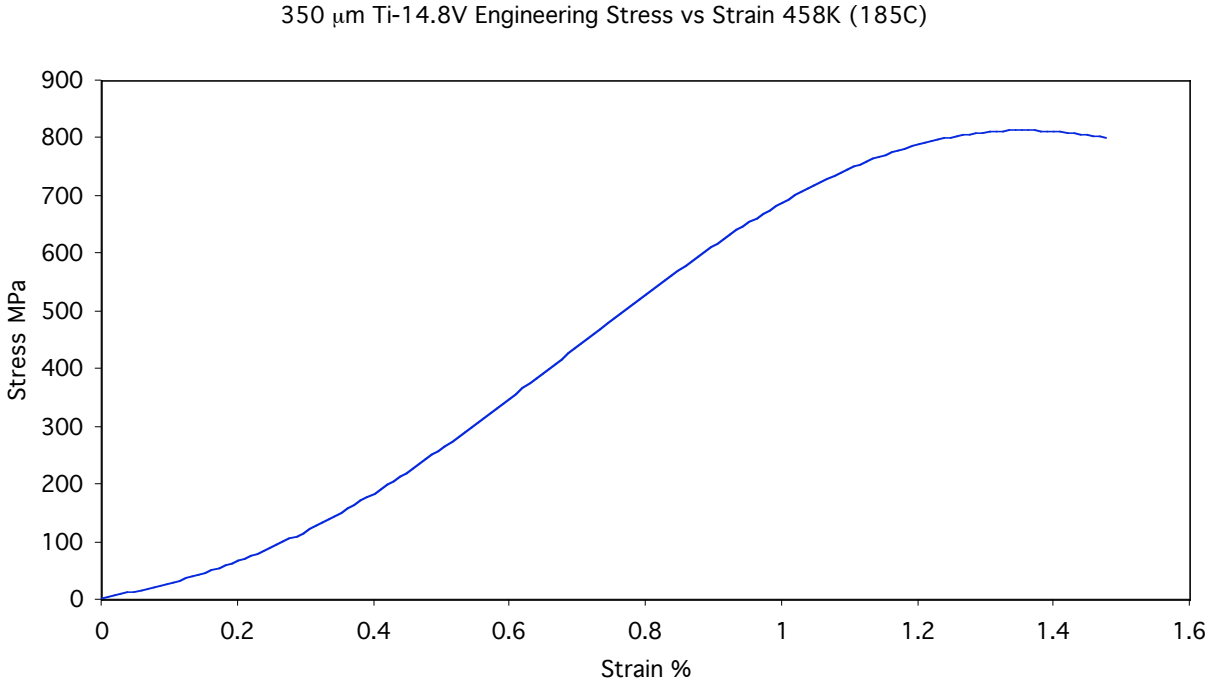

Figure 31 - Engineering Stress vs. Strain Curve 350 μm Ti-14.8V alloy at 458K (185°C). Sample was strained to 1.3% at a strain rate of 2.17×10^{-5}/s before fracture. The 0.2% YS Value was 673.85 MPa.

Creep Testing Results

Continuous creep testing was performed in an argon atmosphere at 298, 338, 378, 418, and 458 K respectively at 95% YS values for each temperature. The applied loading for each creep test was determined using the specific cross sectional area of each sample as detailed in chapter 3. The applied stress value for ambient temperature, 298 K was calculated to be 733.21 MPa for 298K, 690.675 MPa for 338K, 676.68 MPa for 378K, 627.51 MPa for 418K and 673.85 MPa for 458K as mentioned in the tensile section of this chapter. The instantaneous plastic and creep strain is determined as the total strain minus the elastic strain. Where elastic strain is the measured recovered strain of the sample when the applied load is removed. The resulting creep curve is plotted as instantaneous plastic strain plus creep strain versus time. The total observed strain for 298K was 0.125%, 0.15% for 338K, 0.172% for 378K, 0.177% for 418K and 0.251% for 458K. As can be observed in figure 32, all creep curves are relatively smooth and begin with a slight parabolic curve at the beginning of the test and then plateau for the remaining time. It may also be observed in figure 25, there is an increase in creep strain with the increase in test temperature (nonlinear temperature behavior).

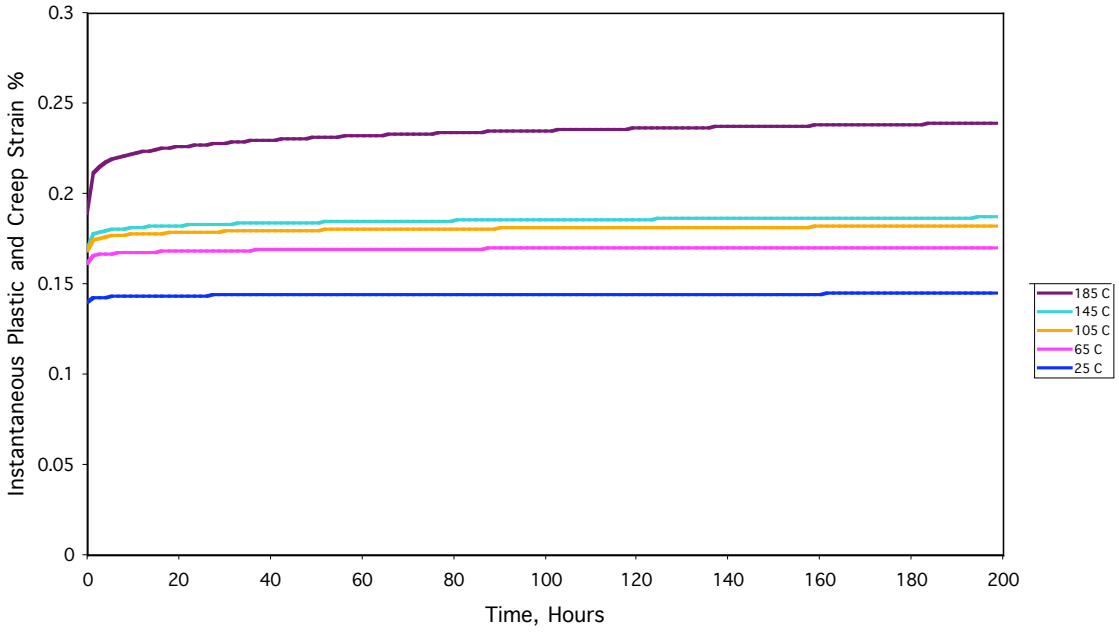

Figure 32 – Plot of all creep curves for 350 μm grain size Ti-14.8V

Microstructure Characterization
Optical and Scanning Electron Microscopy (SEM)

Images were taken of samples before and after deformation. Resulting images of significant features are given in the following images. Significant features, thick lines can be observed in the optical and SEM figures 33 – 46 of deformed specimens. The present lines in the resulting images appear to be slip and stress induced plates (SIP).

338K

Loading Direction

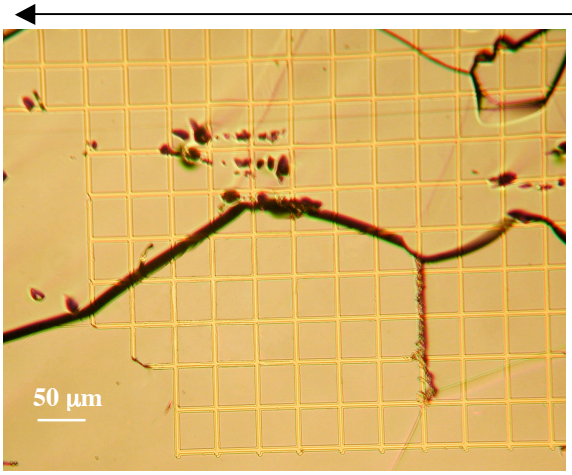

Figure 33 – Optical image of undeformed 350 μm grain size Ti-14.8V sample. Magnification 100X

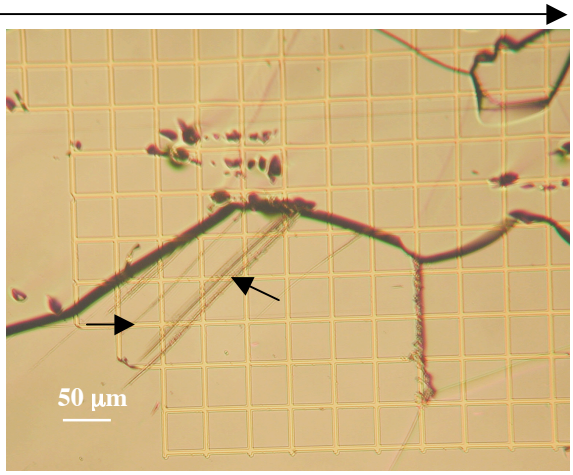

Figure 34 – Optical image of deformed 350 μm grain size Ti-14.8V sample crept at 338K Magnification 100X, notice the lines marked by arrows the thin lines are slip, thick lines appears to be SIP (twins).

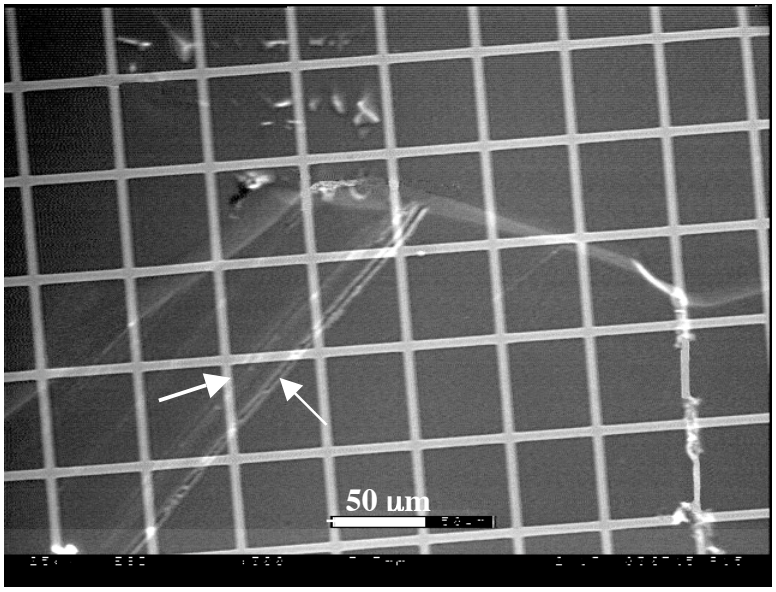

Figure 35 – SEM image of deformed 350 µm grain size Ti-14.8V Sample crept at 338K. Notice the thick SIP (twins) lines indicated by arrows

Loading Direction

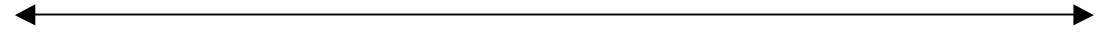

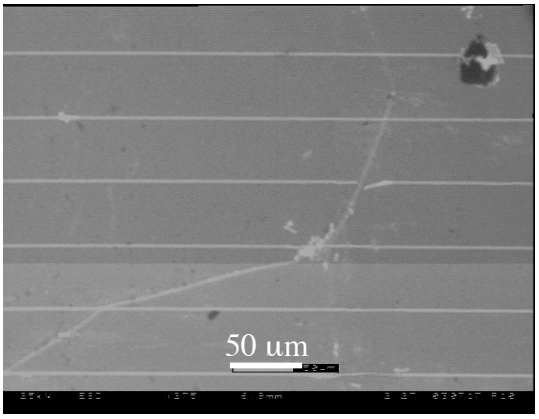

Figure 36 – SEM image of undeformed 350 µm grain size Ti-14.8V

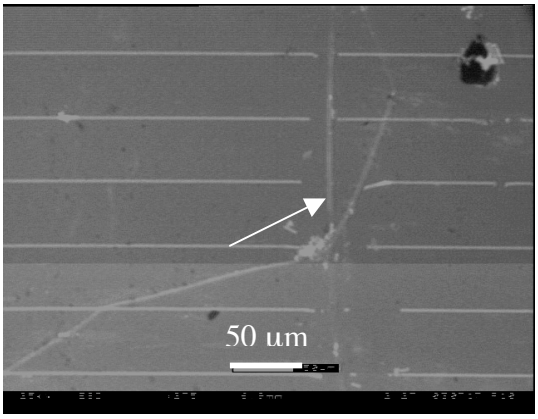

Figure 37 – SEM image of deformed 350 µm grain size Ti-14.8V crept at 338K. Notice the slip line indicated by arrow.

378K

Loading Direction

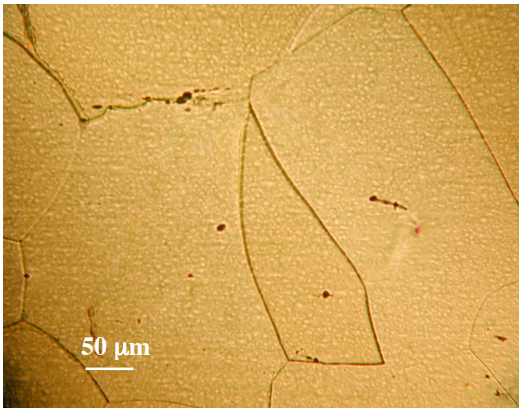

Figure 38 – Optical image of unde-formed 350 µm grain size Ti-14.8V. Magnification 100X.

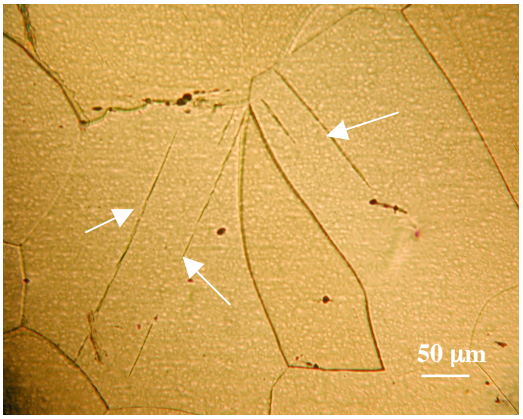

Figure 39 – Optical image of deformed 350 µm grain size Ti-14.8V. Crept at 378K magnification 100X. Notice the slip lines.

Loading Direction

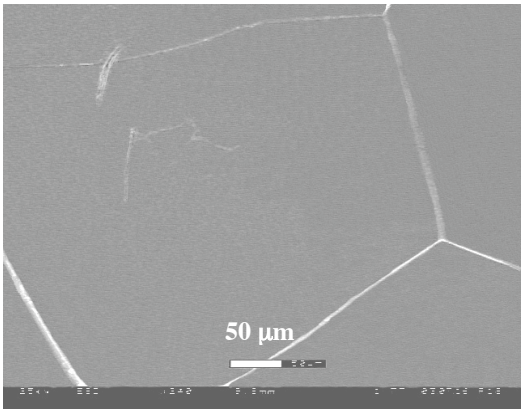

Figure 40 – SEM image of unde-formed 350 µm grain size Ti-14.8V.

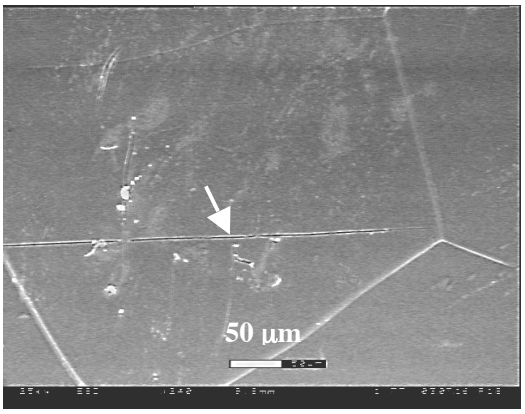

Figure 41 – SEM image of deformed formed 350 µm grain size Ti-14.8V. Crept at 378K. Notice the SIP indicated by arrow.

418K

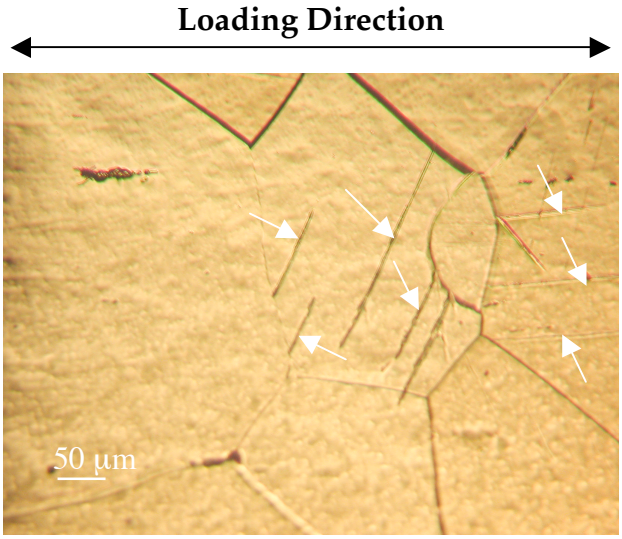

Figure 42– Optical Image of Deformed 418K (145°C) 350 μm Ti-14.8V Creep Specimen. 100X Magnification. Note the slip and SIP (twins, thicker lines) as indicated by arrows.

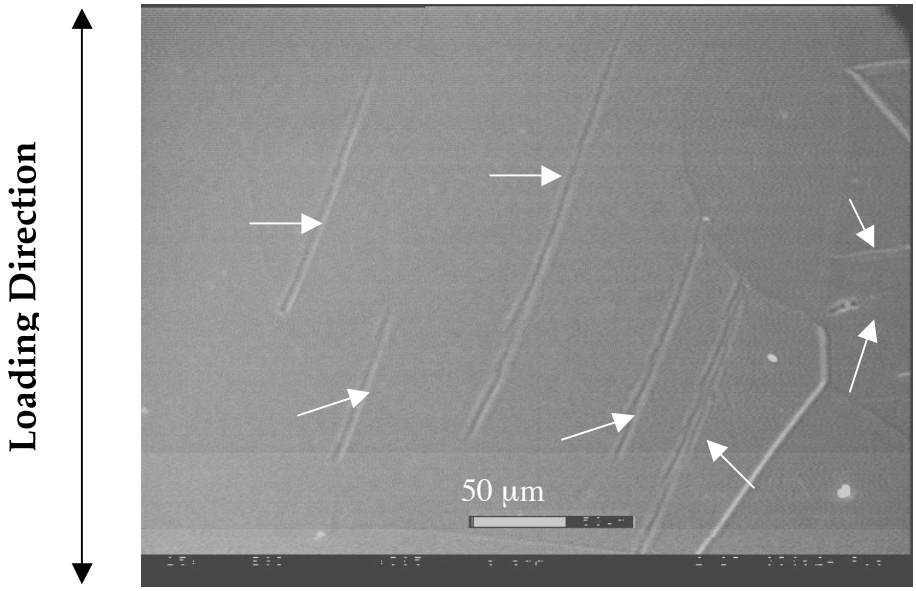

Figure 43 - SEM of Deformed Image of 418K (145°C) 350 μm Ti-14.8V Creep Specimen. Note the SIP (twins) as indicated by arrows.

458K

Loading Direction

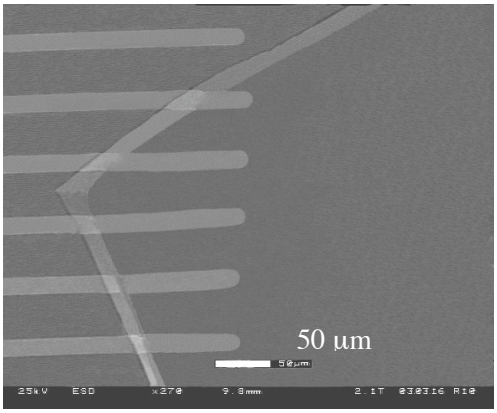

Figure 44 - SEM Image of Undeformed 350 μm Ti-14.8V Specimen

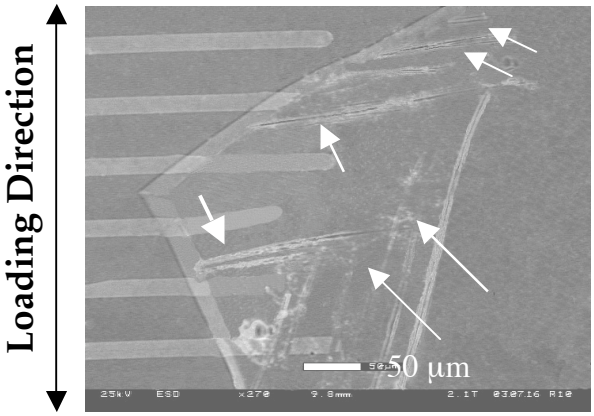

Figure 45 - SEM Image of Deformed 350 μm Ti-14.8V Creep Specimen at 458K. Note the SIP-twins as indicated by arrows.

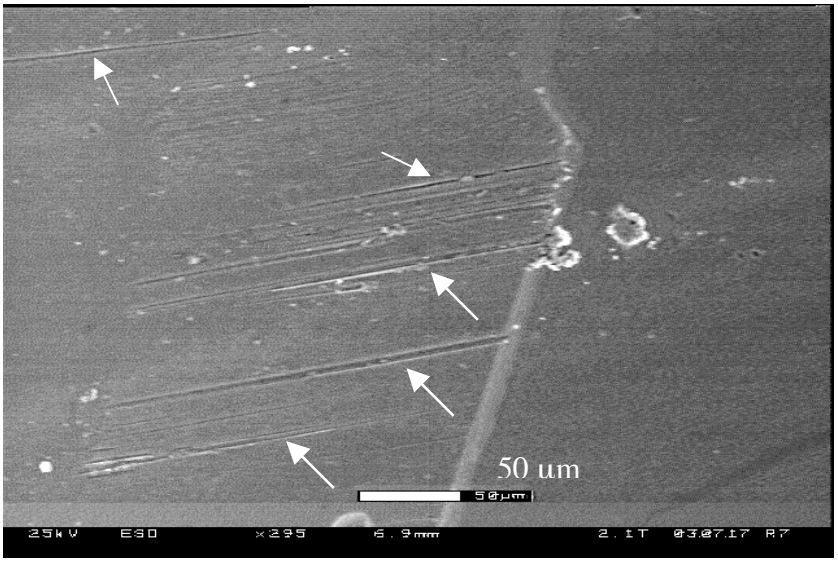

Figure 46 - SEM Image of 458K (185°C) Deformed 350 μm Ti-14.8V creep specimen. Note the SIP twins as indicated by arrows.

As can be observed in both the optical and SEM micrograph images for all investigated temperatures, Ti-14.8V alloy deforms by both slip and stress induced plate (SIP) formation in the form of twinning. Thick slip and twin lines are clearly visible in all images and become more pronounced with the increase in test temperature. Furthermore, there is an increase in the number of slip and SIP (twin lines) with the increase in test temperature.

TEM Images

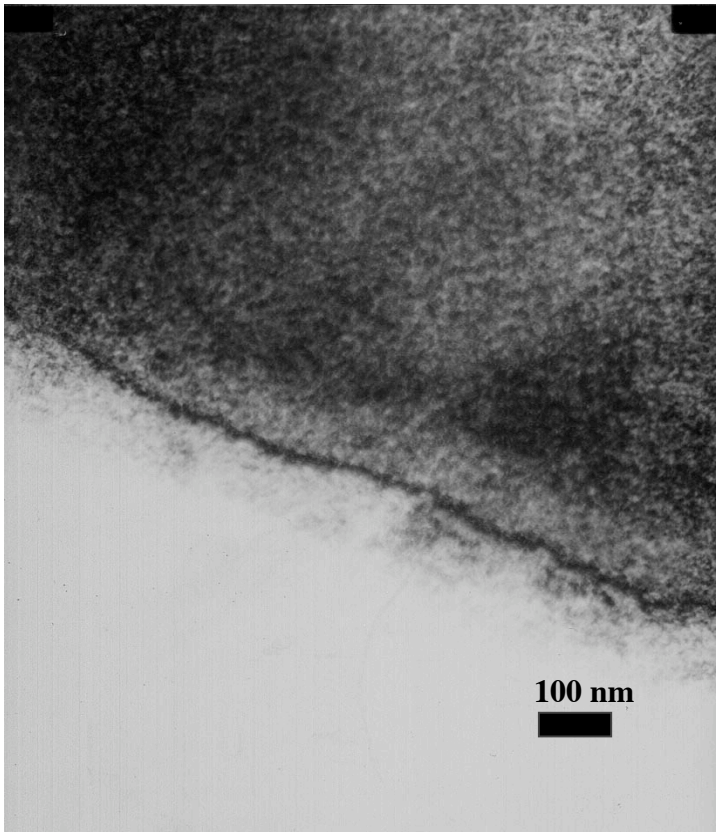

Figure 47 - TEM Bright field image of undeformed 298K Ti-14.8V 350 μm matrix. Magnification 25,000X

As can be viewed in figure 47, a TEM bright field image of ambient temperature, 298K of the undeformed matrix of Ti-14.8V. Figures 48 and 49 are diffraction patterns of the undeformed matrix taken from the matrix region of the

specimen along the <110>$_\beta$ zone axis and the BCC β phase is indexed which are outlined in red circles; the ω phase is visible in the diffraction pattern as they are patterned as four spots (HCP) within the BCC diffraction pattern, circles indicate the ω phase. Double diffraction of the ω phase can also be observed in figure 48 and are indicated by the arrows.

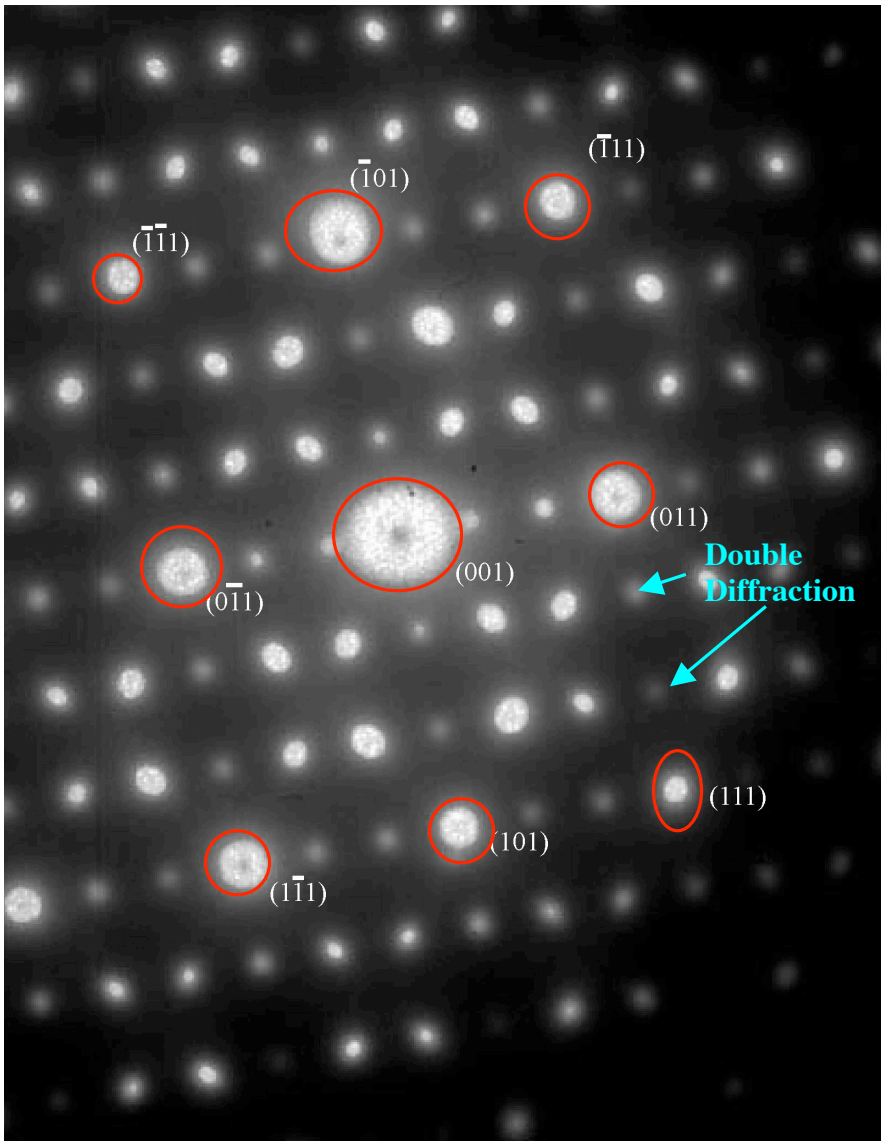

Figure 48 – Diffraction pattern for undeformed 350 μm Ti-14.8V
Pattern BCC β phase is indexed on the <110>$_\beta$ zone axis.

Arrows indicate the double diffraction of the ω phase HCP structure. The ω phase is indexed in the following figure 49, as can be viewed, the ω phase is present as clearly discrete spots within the diffraction pattern as outlined by indicated outlined circles. The intermediate spots of the ω phase are double reflection.

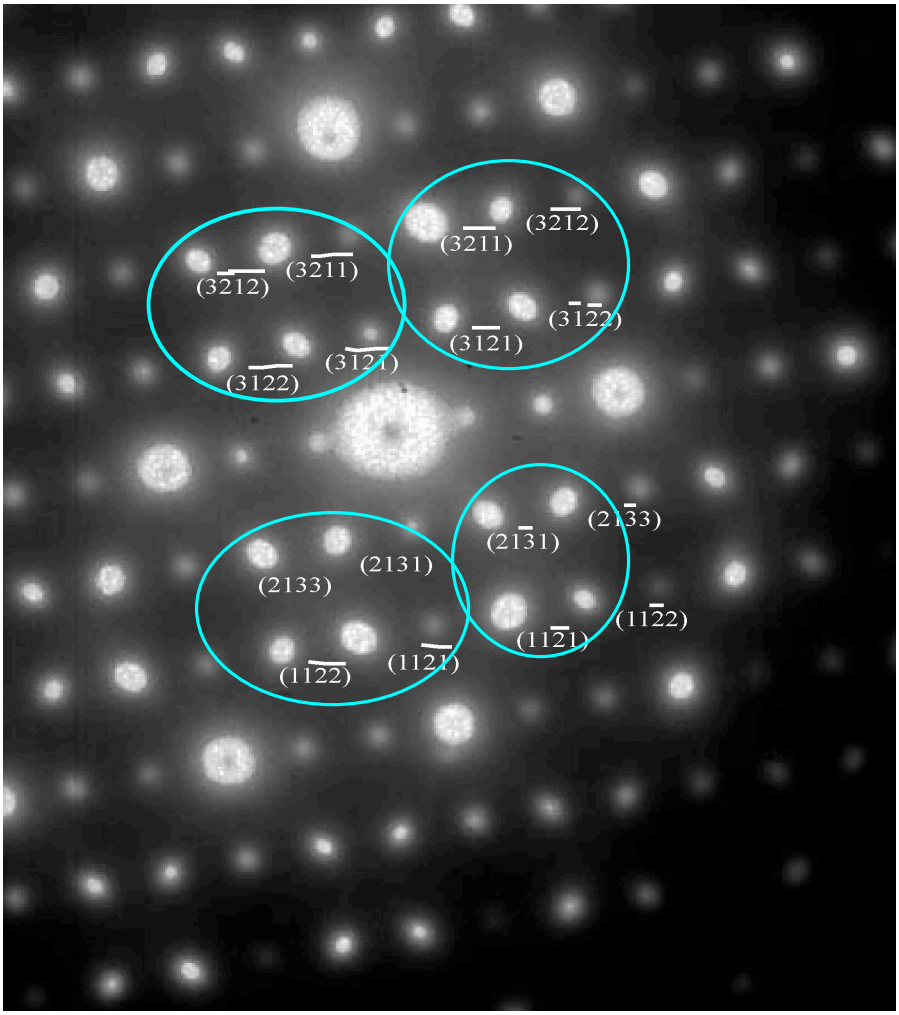

Figure 49 - Diffraction pattern for undeformed 350 μm Ti-14.8V Pattern BCC ω phase is indexed.

Figures 50 – 52 are TEM bright field and dark field images of stress induced plates-twins in the form of {332}<113> taken at magnifications of 50,000 and 53,000X. Diffraction patterns were taken of the matrix and the interface as

can be viewed in figures 52 and 53. Twins were not observed in the undeformed samples of the matrix as shown in figure 47 a bright field image of the matrix.

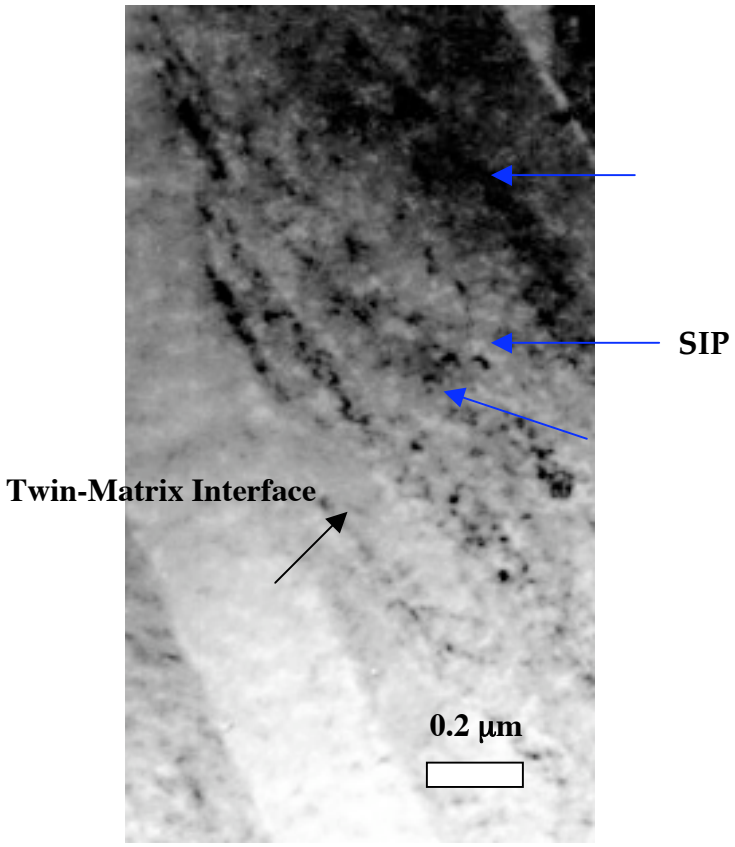

Figure 50 - TEM Bright field image of deformed Ti-14.8V 350 μm at 418K at 53000X. Notice the presence of SIP in the form of twins as indicated by arrows.

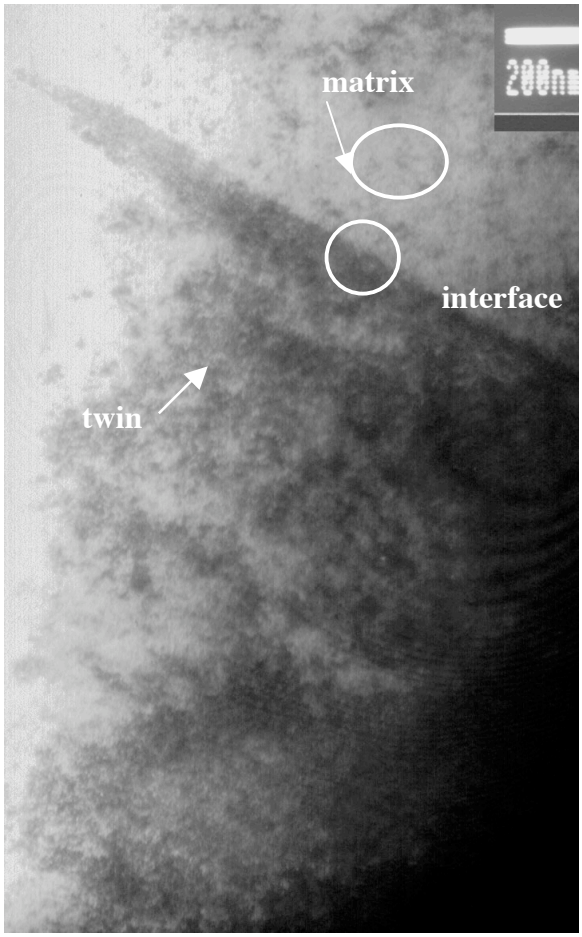

Figure 51 – TEM Bright field image of 418K deformed creep 50,000X
Notice the SIP indicated by arrows.

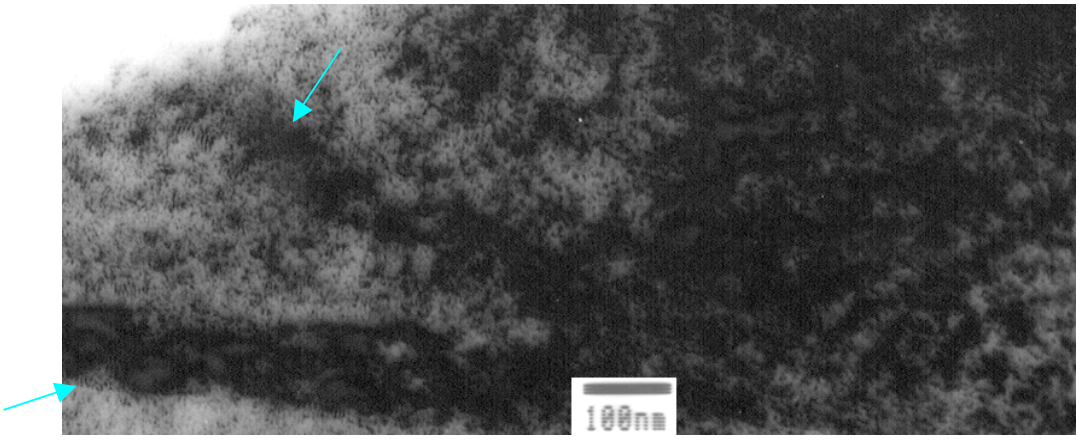

Figure 52 – TEM Dark Field image of 418K creep deformed. Notice the SIP indicated by arrow . Magnification 106,000X

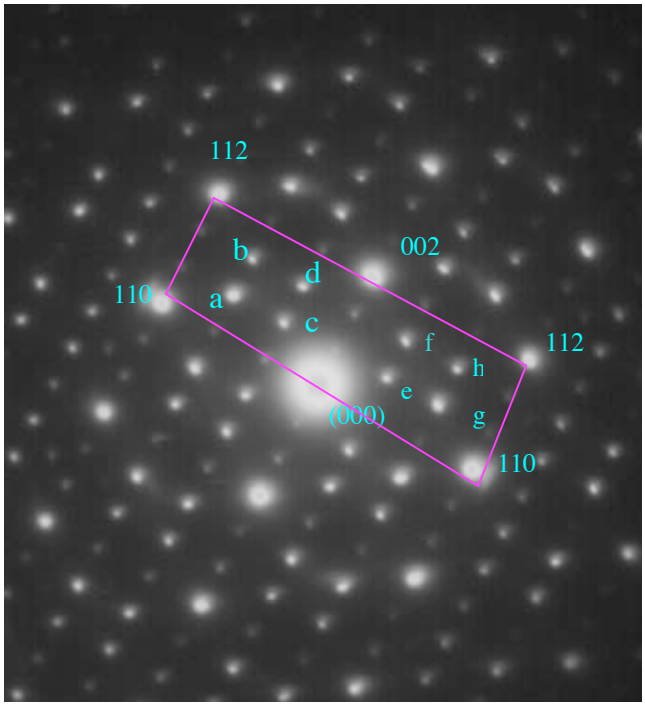

Figure 53 – Diffraction Pattern of Matrix

Indexed as follows:

a: 0001	b: $\overline{2}020$	c: $\overline{1}010$
d: $\overline{1}011$	e: $\overline{1}010$	f: 1011
g: 0001	h: 2020	

The diffraction pattern twin is given in figure 54 the subscript t denotes the twin with the same indices as the given letter.

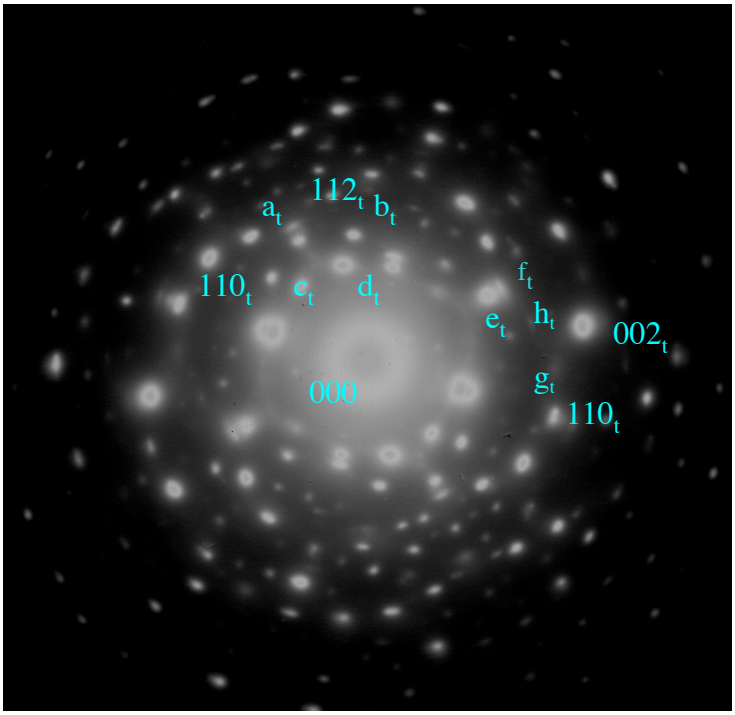

Figure 54 – Diffraction Pattern of Twin-Matrix Interface

As mentioned in the previous paragraphs, observations were made of the undeformed matrix, defects of any type were not observed. Other types of deformation mechanisms were observed by TEM analysis; these were of the type of dislocations, which can be seen in the following figures 55 and 56. Dislocations were identified as the type of 1/2<111> as indicated on the following figure 55, with the g vector as (110).

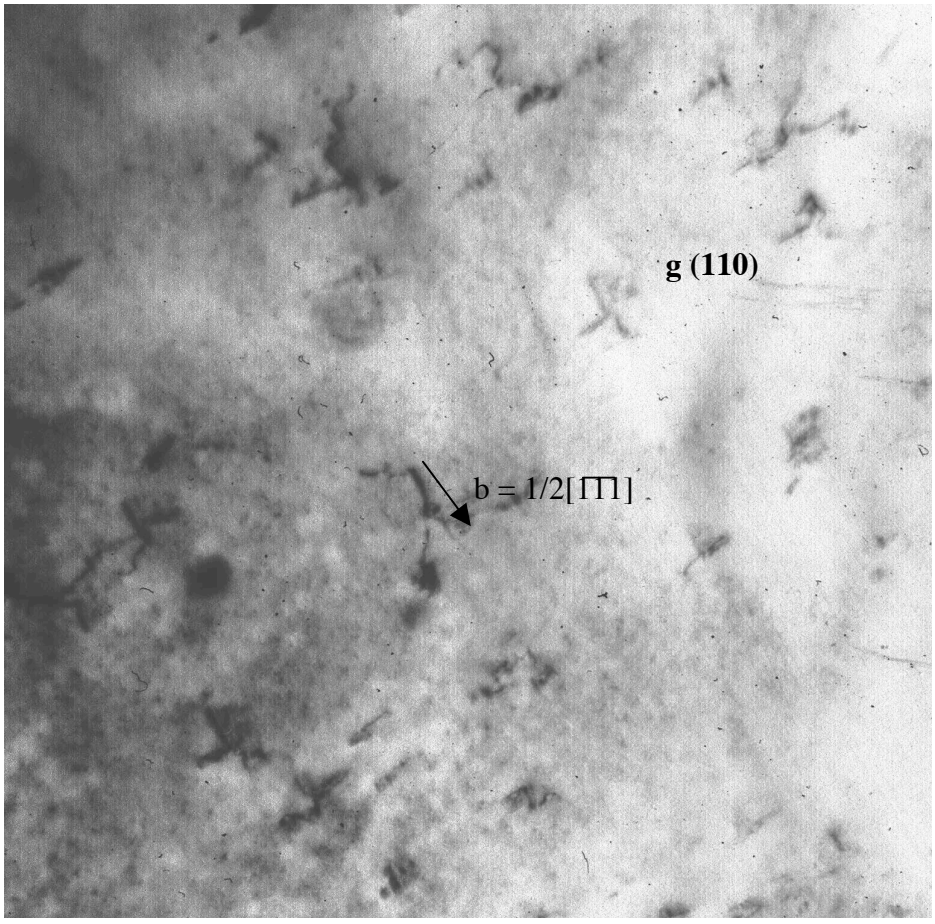

Figure 55 – TEM Bright Field Image of dislocations Magnification 200,000X

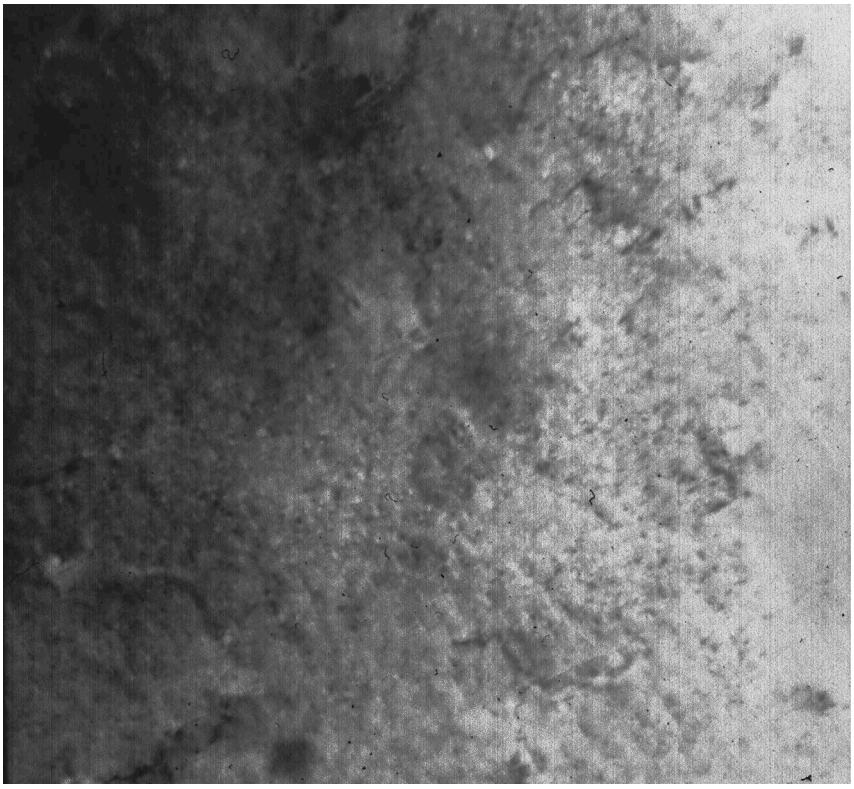

Figure 56 – TEM Dark Field Image of dislocations. Magnification 400,000X.

ANALYTICAL RESULTS

Activation Energy Values

As detailed in chapter one, activation energies for deformation behavior for 350 μm grain size Ti-14.8V alloy were determined as a function of power law creep behavior. The resulting plots are shown in the following figures 57 and 58. As can be seen in figure an Arrhenius plot was generated in which the activation energy values were determined based on the slopes from the resulting straight line curves and according to equations 2-5 a discussed in chapter one; further discussion is given in the subsequent chapter 5. It is interesting to note that the activation energy increases with the increase in strain. Also it is also interesting that the resulting activation energy plots are quite linear with respect to the strain.

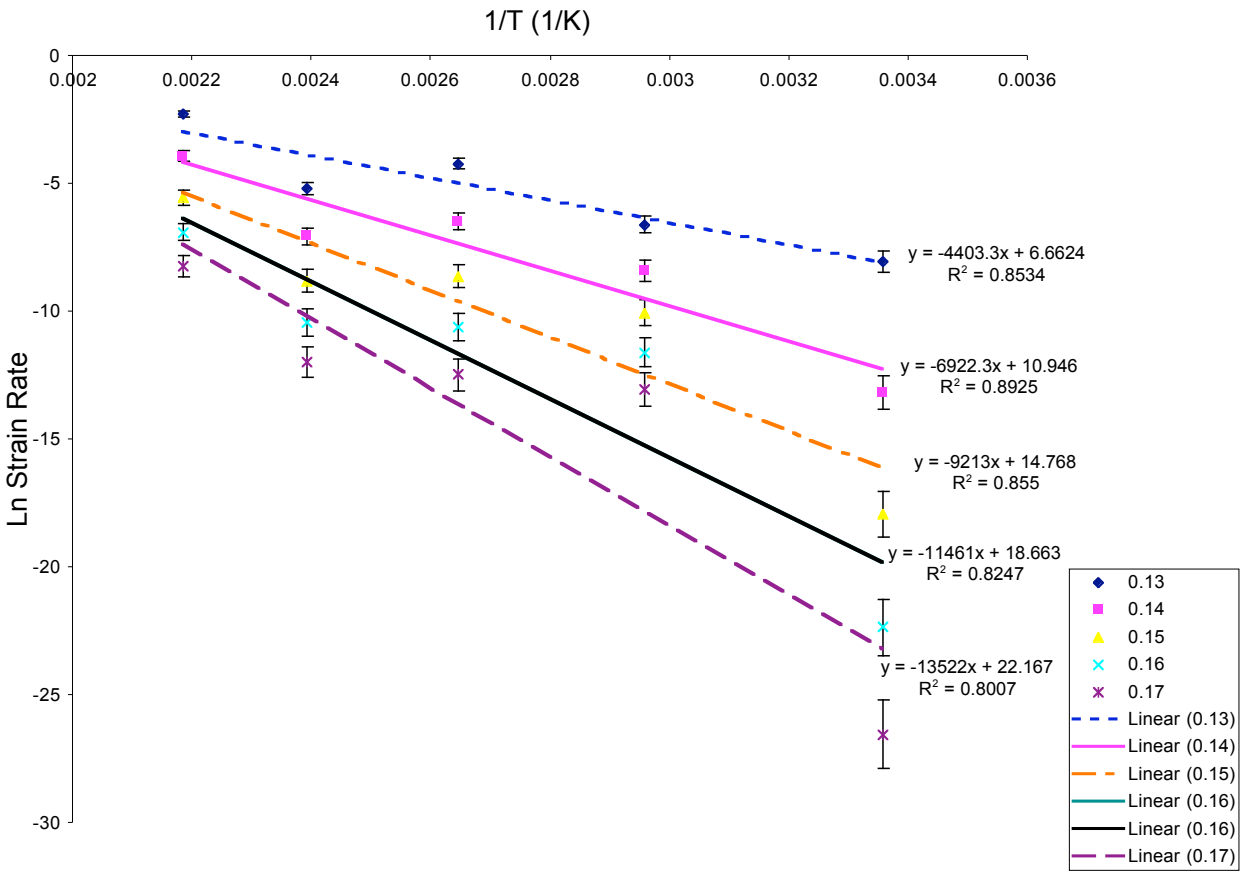

Figure 57 – Arrhenius Plot of 1/Temperature vs. Ln Strain Rate

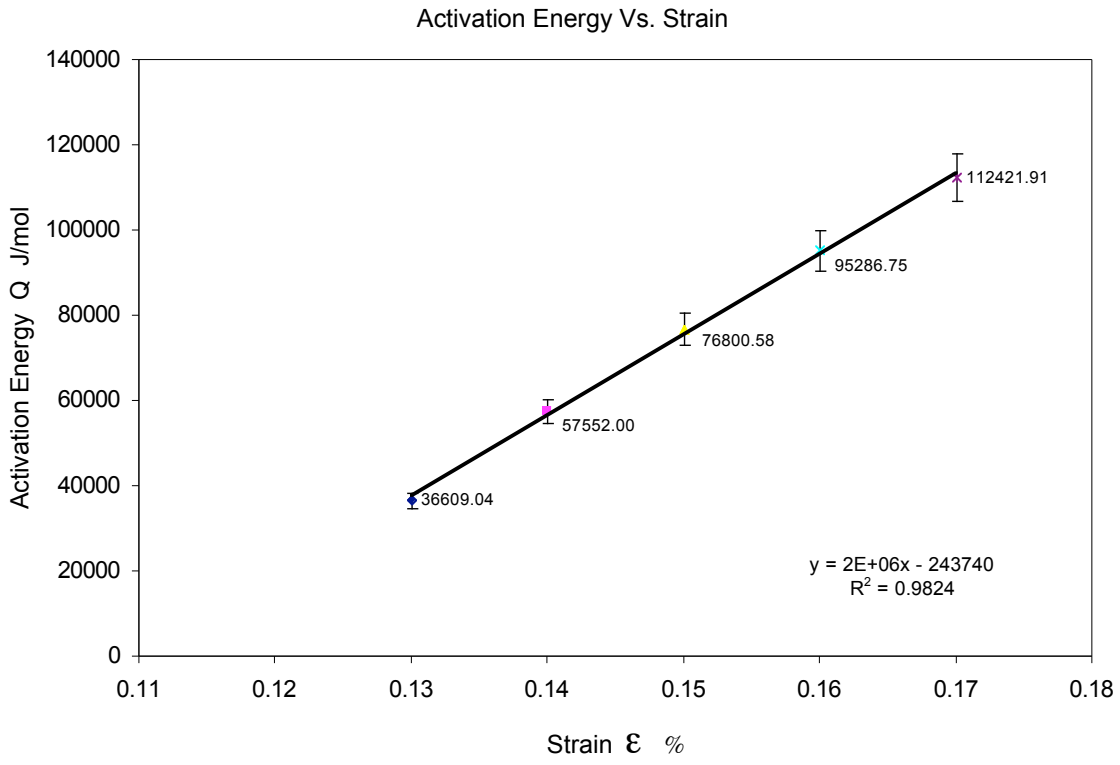

Figure 58 – Activation Energy vs. Strain

Hollomon Constants Determination

Hollomon constants were determined in this study for two different grain sizes of two metastable beta phase titanium alloys, 35 and 350 μm Ti-14.8V alloy and 100 and 500 μm Ti-9.4Mn alloy. Ti-9.4Mn is a more stable alloy with a MoE value of 13, whereas Ti-14.8V has a MoE value of 9. Hollomon constants were calculated according to equations 1, 7, 9, and 10 given in chapter one. Further discussion about the determined Hollomon constant parameters is detailed in chapter five. As can be observed in figure 59 for the Ti-9.4Mn alloy, the stress versus strain curve for the 100 μm grain size is slightly less than the 500 μm grain size.

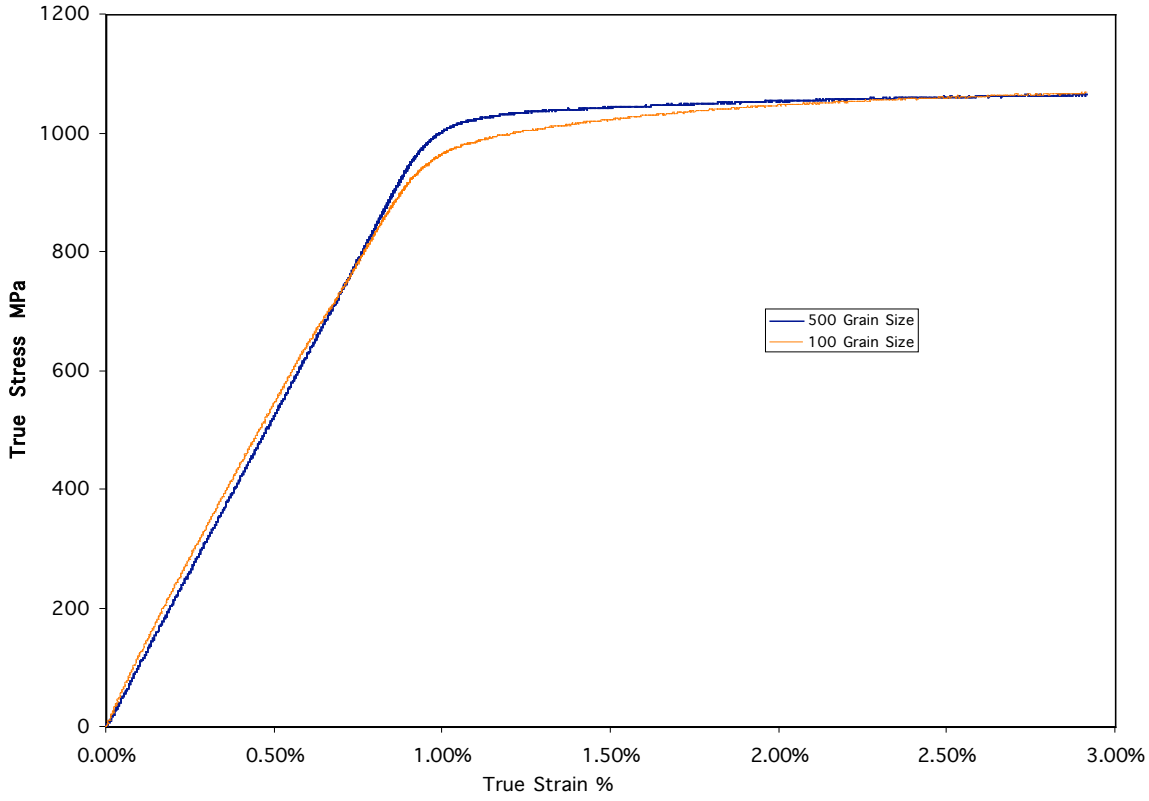

Figure 59 – True Stress vs True Strain Curve for 500 and 100 μm Ti-9.4Mn Alloy [7]

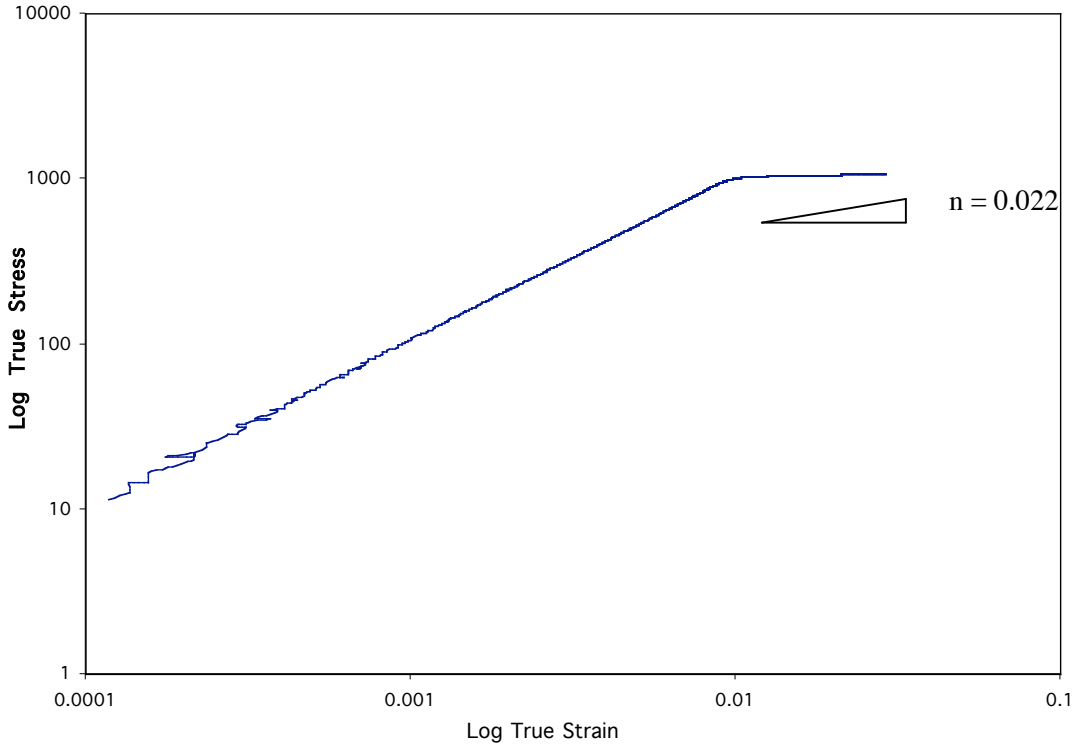

Figure 60 – Log True Stress vs. Log True Strain Curve for 500 μm Grain Size Ti-9.4Mn Alloy [7]

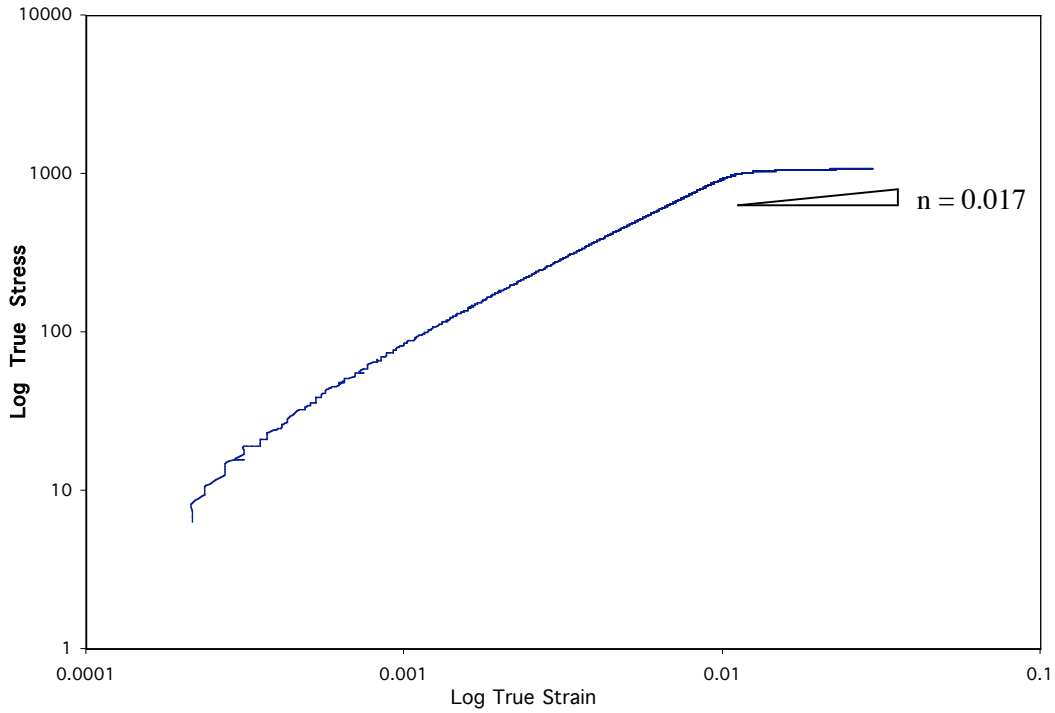

Figure 61 – Log True Stress vs. Log True Strain Curve for 100 μm Ti-9.4Wt%Mn [7]

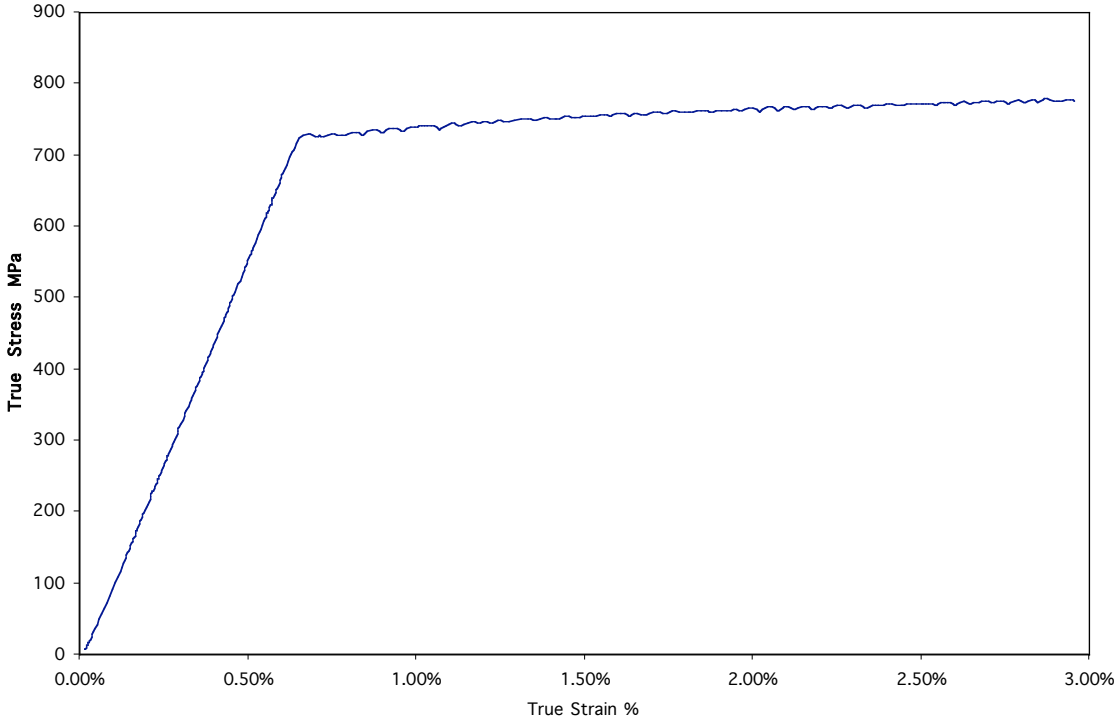

Figure 62 – True Stress vs. True Strain Curve for Ti-14.8V 350 μm Grain Size

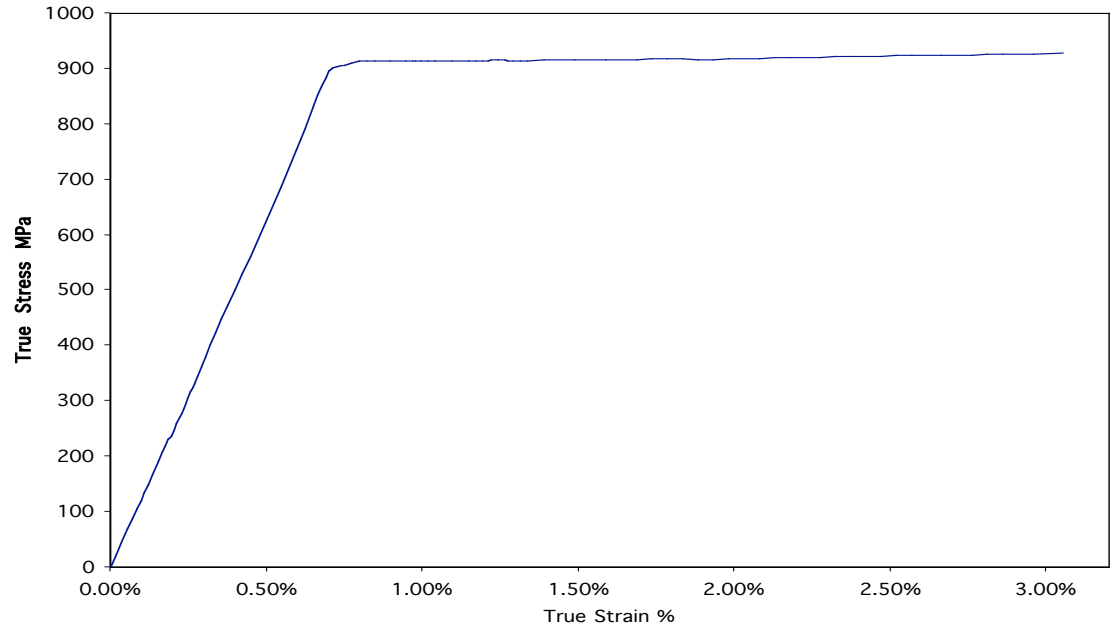

Figure 63 – True Stress vs. True Strain Curve for Ti-14.8V alloy 35 μm Grain Size

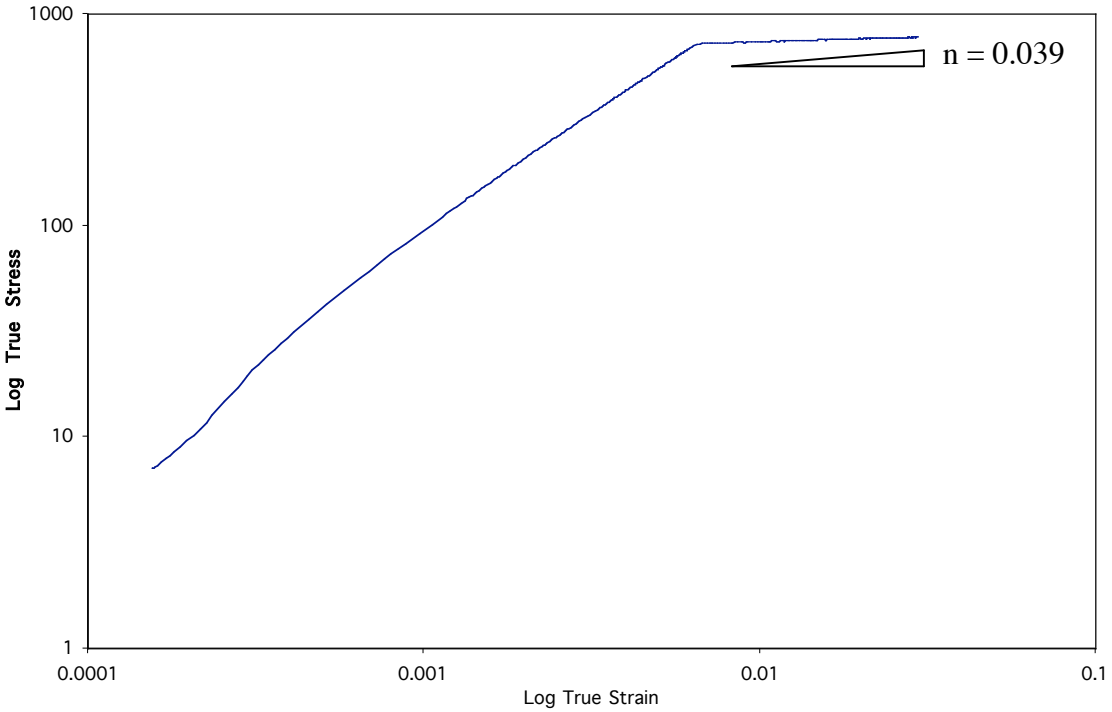

Figure 64 – Log True Stress Vs. Log True Strain Curve for a 350 μm Grain Size Ti-14.8V Alloy

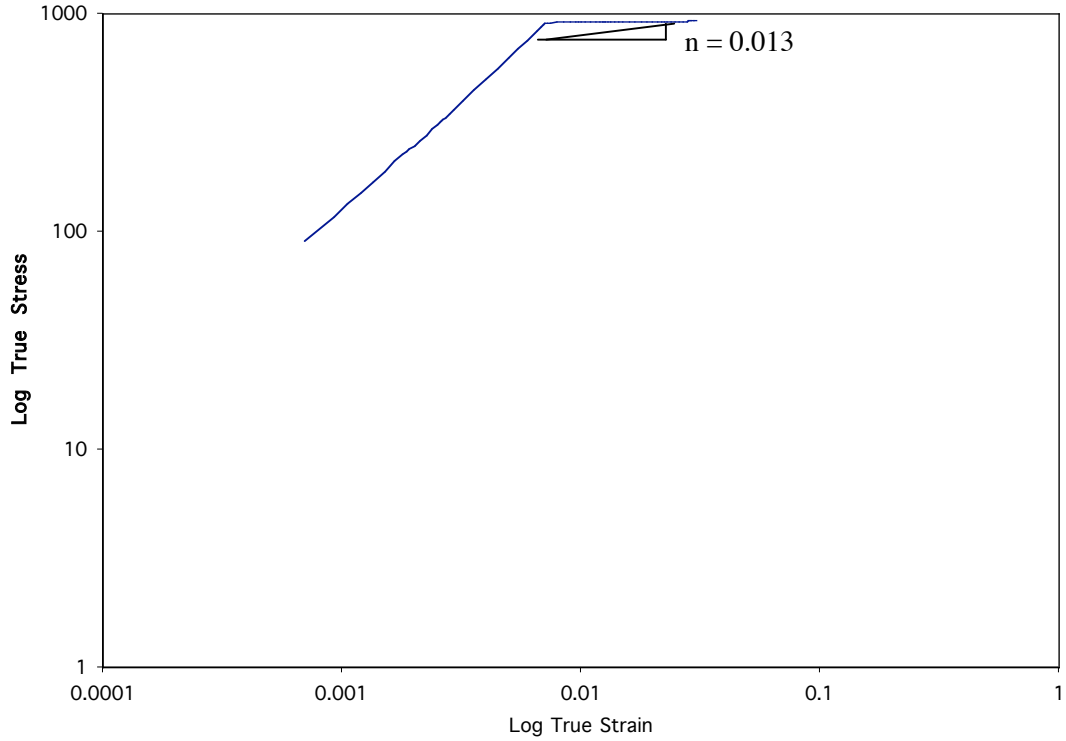

Figure 65 – Log True Stress vs. Log True Strain Curve for 35 μm Ti-14.8V alloy

As can also be observed for the Ti-14.8V alloy, the log true stress vs log true strain curves is a steep slope and then plateaus slightly horizontally. The Hollomon constants were determined from the end slope as indicated on the respective curves; detailed discussions follow in the subsequent chapter 5.

Effect of Phase Stability on Hollomon Constants

The effect of phase stability has an effect on the resulting Hollomon Constant parameter values. The more stability the alloy, the lower the Hollomon Constant parameter values and subsequently, the lower the predicted creep strain value with respect to alloy phase stability. As can be observed in the following figures , the Hollomon constants for strain rate sensitivity and strain hardening exponent value decrease with the decrease in alloy phase stability and with respect to the decrease in grain size for the given alloy (this is also viewed in table 12). Conversely, the magnitude of these constants are much larger for a less stable alloy than for a more stable alloy. This can be best viewed in the following figures and in table 12 (chapter 5) where it can be seen that for example, the value for n for 350 μm Ti-14.8V is 0.039, but for a 500 μm Ti-19.4Mn a more stable alloy, the value for n is 0.022, which is much less.

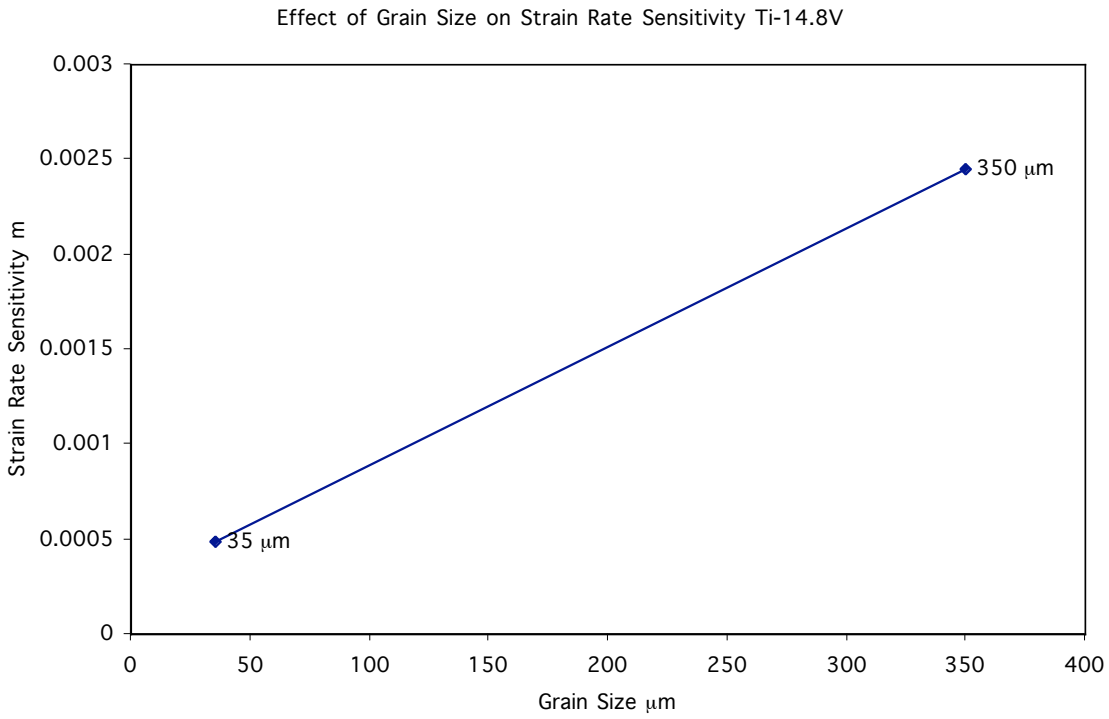

Figure 66 – Effect of Grain Size on Strain Rate Sensitivity m for Ti-14.8V

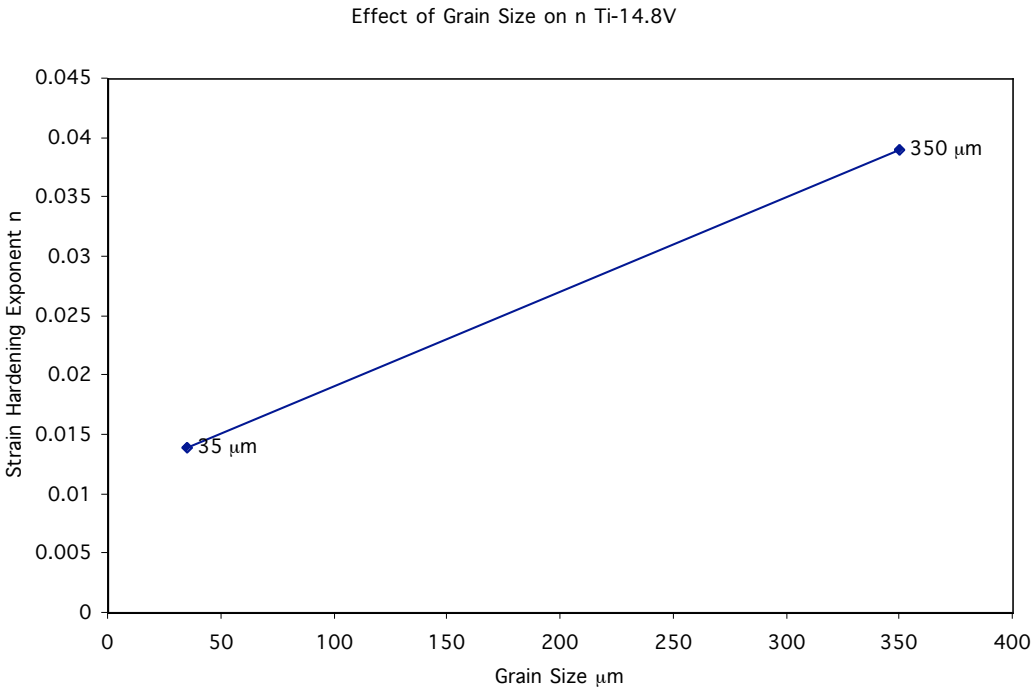

Figure 67 – Effect of Grain Size on Strain Hardening Exponent n for Ti-14.8V

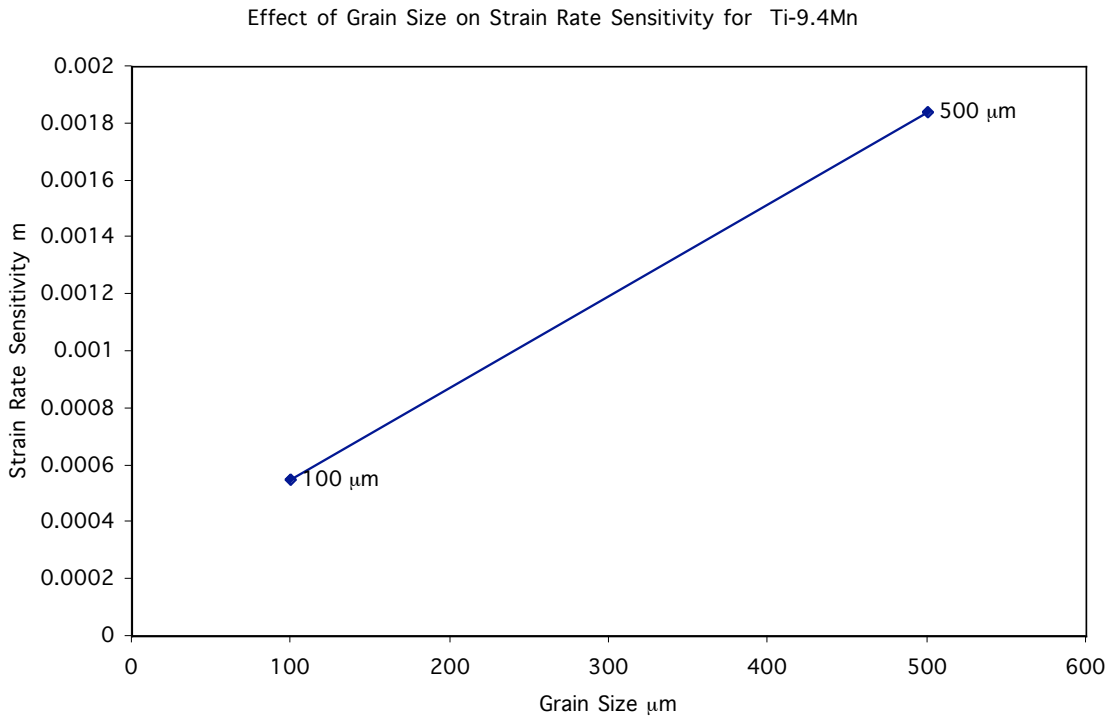

Figure 68 – Effect of Grain Size on Strain Rate Sensitivity m for Ti-9.4Mn

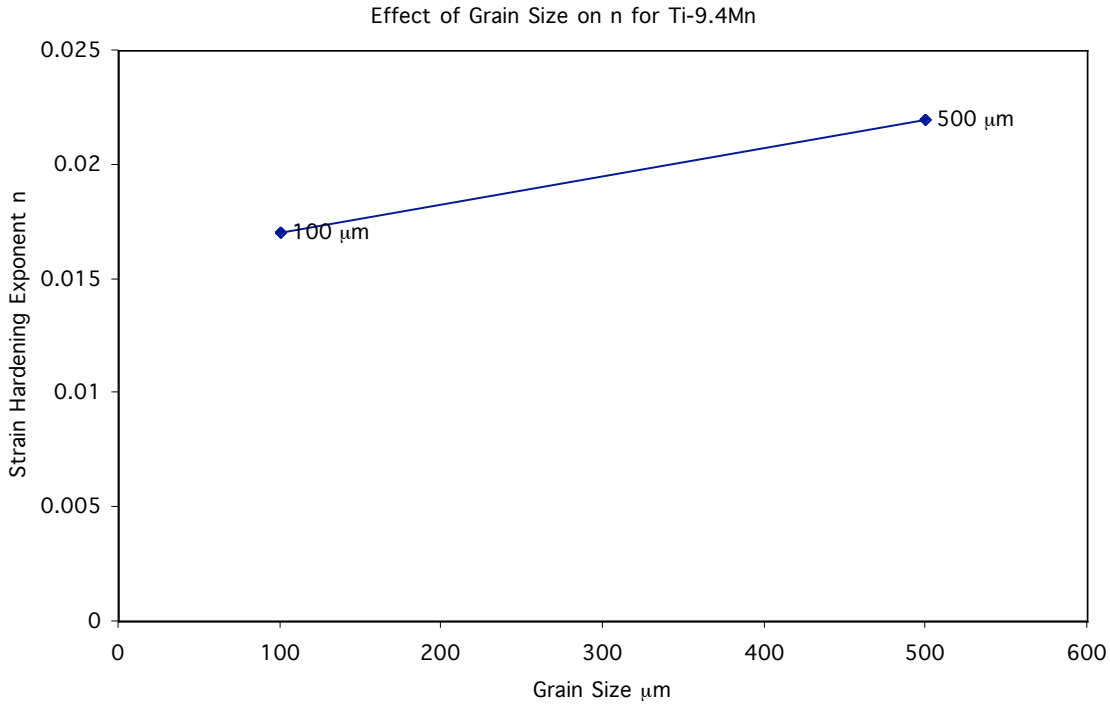

Figure 69 – Effect of Grain Size on Strain Hardening Exponent n for Ti-9.4Mn

Hollomon constants can reasonably predict the flow stress creep behavior for beta titanium alloys. The creep strain was predicted for 95% stress level for 500 μm Ti-9.4Mn and 350 μm Ti-14.8V using the Hollomon Constant parameters based on creep power law behavior. A predicted value of 0.014 for creep strain was determined for 500 μm Ti-9.4Mn and a predicted value of 0.13 for 350 μm Ti-14.8V creep strain. The predicted creep strains using the Hollomon constants were within twenty percent of the actual creep strain (see table 12 in chapter 5 for actual creep strain values).

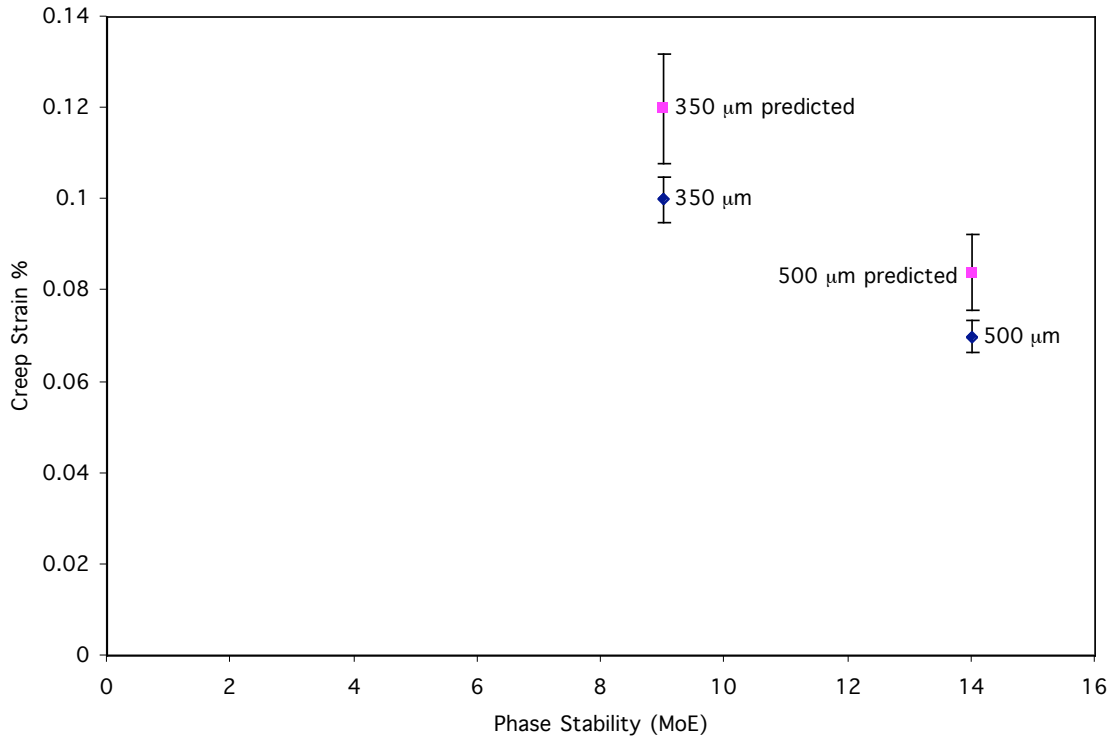

Figure 70 – Comparison of Predicted Creep Strain Values by Hollomon Constants with Actual Creep Strain Values

CHAPTER 5

DISCUSSION

Creep Constants Determination

Creep constants were determined according to equation 1 as outlined in chapter one. As can be observed in table 10, the creep coefficient A values increased with the increase in both temperature and strain, with the exception of the lower value for 418K. The creep coefficient A has a minimum value of 0.07 for a temperature of 298K and a maximum value of 0.1474 for 458K; with the exception for test temperature 418K where the coefficient A value s 0.1306 which is less than the value of 0.1354 for test temperature 378K. This same increasing value pattern is also followed by the creep exponent n, in which the values increase with the increase in temperature and creep strain from a value of 0.06 for test temperature 298K to a value of 0.043 for test temperature 458K. There is also an exception with a lower value for 378K, where n is 0.035, which is less than the value of 0.04 for 338K. For visualization plots are given in figure 71 and 72.

Table 10 - Creep Constant Values

Temperature	A	n	R^2
298K (25ºC)	0.07	0.06	0.27
338K (65ºC)	0.1232	0.04	0.1514
378K (105ºC)	0.1354	0.035	0.0984
418K (145ºC)	0.1306	0.038	0.1057
458K (185ºC)	0.1474	0.043	0.1423

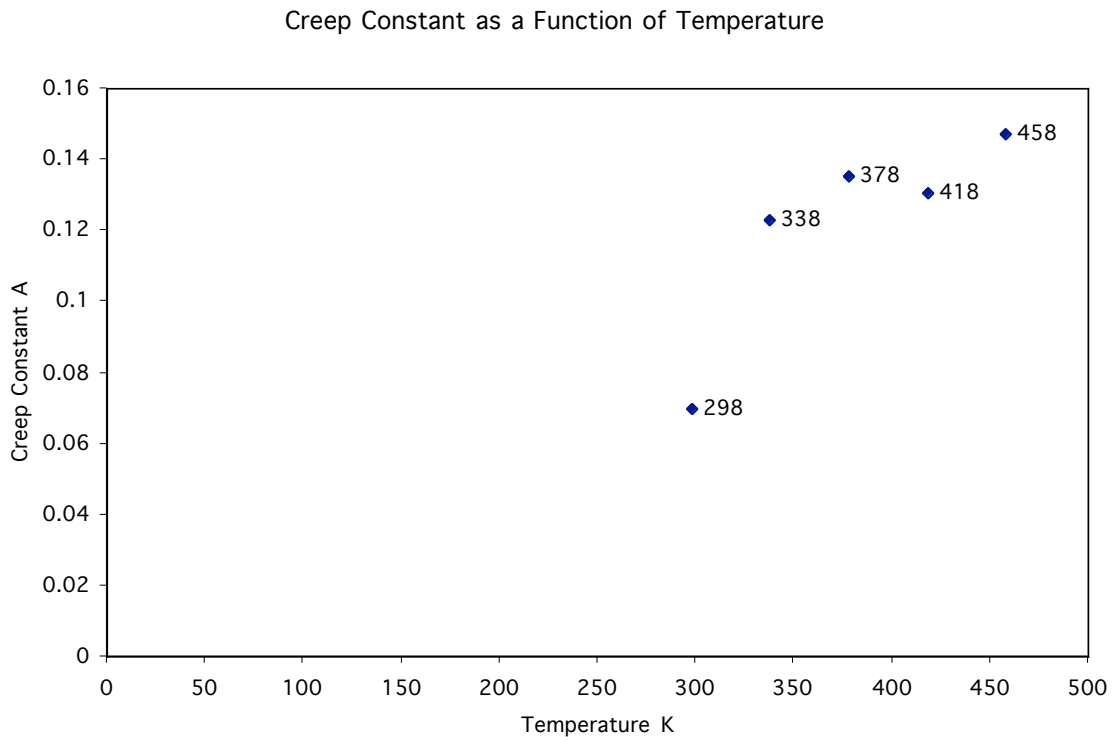

Figure 71 – Creep constants as a function of temperature

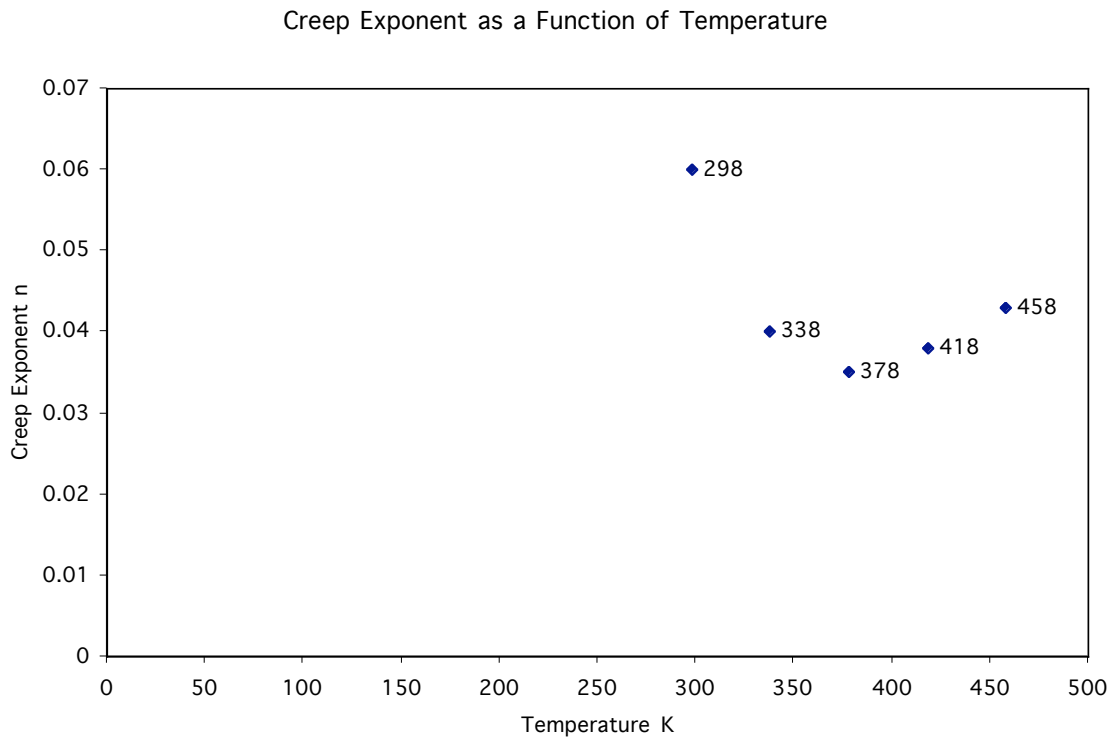

Figure 72 – Creep Exponent n as a function of temperature K

Mechanical Testing
Tensile & Creep Testing

In figures 23 - 31, the magnitude of the stress and yield stress decrease with the increase in test temperature. This can be attributed to the increased ductility of the alloy with the increase in temperature. The 95% yield stress values were determined as the following: 733.21 MPa for 298K, 690.675 MPa for 338K, 688.875 MPa for 378K, 627.51 MPa for 418K, and 673.85 MPa for 458K. As can be observed in figure 31 for tensile test temperature 458K the sample fractured before reaching a full strain of 3%. This was mostly due to the rapid strain rate, however, there was a sufficient amount of curve to obtain the 0.2% offset value for the yield strength.

As can be observed in figure 25, like the tensile plots, the amount of creep strain increases with the increase in temperature. This increase in magnitude can also be attributed to the increased ductility of the alloy with the increase in test temperature. The amount of creep strain were for 0.125% for 298K, 0.15% for 338K, 0.172% for 378K, 0.177% for 418K and 0.251% for 458K.

Microstructure Characterization
Optical and SEM

Multiple slip lines and thicker lines, which appears to be twins can be clearly viewed in figure 27, an optical image take after creep deformation at 338K. Accordingly, multiple slip and twin lines are also viewed at higher test temperatures (see figures 32 and 35, optical images taken after creep deformation at 378K and 418K), the amount of slip lines increase with the increase in test temperature, as well as the thickness of the induced lines. This can be visibly seen in figures 39, 42, 43, 45, and 46 where at the higher test temperatures of 378, 418, and 458K multiple slip and twin lines increase with the increase in test temperature. Accordingly, it can be observed that the line thickness is quite heavy at the higher test temperature of 458K, but not so pronounced at the lower test temperature of 378K.

TEM

TEM micrographs were taken of undeformed and deformed specimens to ascertain the nature of the deformation mechanisms responsible for low temperature creep behavior. As can be observed in the figure 48, the diffraction pattern of the undeformed matrix, the alloy studied is beta phase matrix this is

evidenced by the diffraction of the BCC structure for the beta phase and the diffraction of the HCP for the ω phase.

Stress induced plates (SIP) in the form of twinning were the identified low temperature deformation mechanisms for a 350 μm Ti-14.8V alloy, which can be observed in the bright field images taken of a sample deformed at 418K in figures 49, 51, and 52 and corresponding diffraction patterns. Twins were identified as the {332}<113> type. Twins were identified as the {332}<113> type. Dislocations were also observed and identified as edge with Burgers vector of the 1/2<111> type.

Analytical Results

Activation Energy Values Determination

As detailed in chapter one, activation energies for deformation behavior for 350 μm grain size Ti-14.8V alloy were determined as a function of power law creep behavior. These values were determined based upon the strain rate based on the creep parameter values, which were determined using equations 2, 3 and 5.

$$\dot{\varepsilon}(\varepsilon) = aA^{\frac{1}{a}}(\varepsilon)^{-\frac{1}{a}} \tag{2}$$

$$Q(\varepsilon) = -R\left[\frac{\Delta \ln \dot{\varepsilon}(\varepsilon)}{\Delta(1/T)}\right]_{const.\sigma,\varepsilon} \tag{3}$$

$$\dot{\varepsilon}(\varepsilon) = \left[A\sigma^{n} \exp\left(\frac{-Q(\varepsilon)}{RT}\right)\right] \tag{5}$$

As can be viewed in figures 57 and 58, which are plots of the natural log of the strain rate (strain rate%/seconds) verse the inverse temperature versus and

activation energy Q and versus strain rate respectively, a linear trend was fit for figure 58 according to the least squares method. The R^2 values are reasonably well; and are all above 0.80 and are listed in the table 11. Accordingly as can be viewed in table 11, the activation energy values increase with the increase in strain; these values increased from a value of 36,609 J/mole for a strain of 0.13% to 112,422 J/mole for a strain of 0.17%; where the median strain of 0.15% has a median activation energy value of 76,801 J/mole. Therefore, the activation energy Q is a function of strain and changes with respect to the most responsible (dominant) deformation mechanism. In this respect, the initial dominant mechanism are dislocations and slip, which drag oxygen solutes, once the dislocations accumulate and pile up, consisting of trapped oxygen solutes, the deformation behavior changes from dislocation slip to time dependent twinning (a deformation that has been previously observed for 350 μm Ti-14.8V by Ankem et. al. [8]) as evidenced in TEM observations of {332}<113> type twins.

Table 11 – Activation Energy Values

Strain (%)	Q (kJ/ mole)	R^2
0.13	36.6	0.8534
0.14	57.55	0.8925
0.15	76.8	0.8567
0.16	95.29	0.8247
0.17	112.42	0.8007

Comparison With Other Activation Energy Studies

As mentioned in the previous section (activation energy value determination), the activation energy values increase with the increase in strain, the values increased from 36,609 J/mole for a strain of 0.13% to 112,422 J/mole for a strain of 0.17% in the temperature range of 273 to 458K. Therefore, the

activation energy Q is a function of strain and changes with respect to the mechanism most responsible for deformation. Activation energies for tracer oxygen diffusion are not the same for deformation behavior such as slip, dislocation motion, and twinning. The activation energies determined for this study which have not been previously found for this alloy at the studied temperature range, are based on creep deformation behavior, i.e. the dominant deformation mechanisms. Since the determined activation values are a function of strain, both observed deformation modes, slip and twinning contribute to the activation energy values for this alloy. Since these processes are in parallel, therefore both processes contribute to the deformation behavior with twinning being the dominant mechanisms at higher temperature. An activation energy value of 95,287 J/mol was determined for a strain of 0.16%, this value is within the activation energy value of 93,000 J/mol for oxygen diffusion determined by Flower [72]. This therefore suggests that oxygen solutes are entrapped therefore making it difficult for the alloy to deform by slip and therefore must deform by twinning as a result of the oxygen solutes.

Diffusion

Numerous research studies have been performed on understanding the diffusive behavior of various elements in beta titanium alloys, most of these studies have been conducted in the high temperature regime > 1000K. In a research study conducted by Maeda et. al. on the inter-diffusion of Cr in Ti-15at%Cr, and Fe in Ti-15at%Fe in the temperature range of 1123-1273K [32]. The activation energies for inter-diffusion were determined to be the following: 160,000 J/mol for diffusion of Cr in Ti-Cr, values in the range of 180,000-195,000

for Fe in Ti-Fe. The values obtained by Maeda for inter-diffusion of Cr and Fe in Ti-Cr and Ti-Fe are higher than for impurity diffusion, these high values are due to the fact the same size element was studied for diffusion behavior as opposed to larger impurity solutes [32].

In studies performed by Dyment et. al. on the self-diffusion of Ti in the beta phase of Ti, the resulting activation energy value was determined to be 152,818 J/mol [34]. This value is slightly less than the value of 160,000 J/mol for the diffusion of Cr in a Ti-Cr alloy and significantly less than the values of 180,000-195,000 J/mol for diffusion of Fe in a Ti-Fe alloy which is as expected since this value of 152,818 J/mol corresponds to the self diffusion of the same element. Accordingly, the activation energy value for self-diffusion of Ti in beta titanium is much larger than the activation energy for creep deformation

In diffusion studies conducted by Claisse et. al. and Wasilwewski and Kehl, they determined that the activation energy for the diffusion of oxygen in beta titanium to be 124.6 and 193 kJ/mol respectively. Which therefore corresponds to the higher activation energy values for the diffusion of large oxygen solutes within the BCC matrix for beta titanium as obtained in this study [75].

Dislocation

Minimal studies have been conducted on the low temperature creep deformation behavior of beta titanium alloys and determination of resulting activation energies corresponding to creep deformation mechanisms. Most of the studies involving determination of activation energies responsible for tensile creep deformation behavior have been in the intermediate to high temperature

regime, i.e. > 600K. Of the few studies that have been conducted, these include low temperature studies performed by deMeester et. al. on a near beta titanium alloy [74]. DeMeester et. al. determined the activation energy in the temperature range of 4.2-760K to be 125 kJ/mole and that presence of oxygen interstitial solutes act as obstacles controlling the dislocation motion for deformation behavior. Therefore, the presence of oxygen solutes causes dislocation pile-ups in which the alloy must overcome to continue to deform.

In another study conducted on a Ti-6Al-2Nb-1Ta-0.8Mo alloy (an $\alpha + \beta$, near β alloy) by Miller, Chen and Starke [74] in the temperature range of 298 to 873K, activation energy values were determined to be 53 kJ/mole and 143 kJ/mole. Miller et. al. observed significant amounts of dislocations at the lower strains which was followed by cross slip at higher strains as the dominant deformation mechanisms for this alloy. The value of 143 kJ/mole was for the diffusion of oxygen in the alloy. Miller concluded that the deformation mechanism changing from dislocation motion to cross slip can be attributed to the presence of oxygen solutes and the alloy overcoming their presence.

Although studies on creep deformation behavior performed on beta Ti-Mo alloys consisting of Mo alloying additions ranging from 17.8Wt% to 25.5Wt% and grain sizes ranging from 45 to 135 μm by Clauer and Wilcox [31] were conducted at higher temperatures in the t range of 933-1373K revealed activation energy values ranging from 110,000 J/mol to 255,000 J/mol; it should be noted since Clauer observed the effect of alloy phase stability. Clauer observed that the predominant deformation mechanisms observed for the investigated alloys were slip and dislocation behavior, which were confirmed by TEM micrograph

images. Clauer observed that the activation energy values increased with the increase in Mo alloying additions (i.e. the activation energy increase with the increase in phase stability) [31]. Accordingly, Clauer also observed that the amount of creep strain increased with the increase in creep strain. Clauer concluded that the dominant deformation behavior for this alloy was slip and dislocation, in which dislocation was the rate controlling mechanism [31]. Clauer also concluded that dislocation densities that dragged atmosphere solute (oxygen) atoms were the dominant deformation behavior at higher temperatures, which corresponded to the large activation energy values. Although this study was performed at lower temperatures, comparatively, the presence of oxygen solutes entrapped in the observed dislocations and dragged; which therefore the alloy subsequently deformed by the observed twinning behavior.

Flow Stress Behavior – Hollomon Constants Determination

The flow stress, long term creep behavior of titanium alloys can be reasonably predicted based on determined Hollomon constants. Hollomon constants were determined in this study for two different grain sizes for two metastable alloys; 35 and 350 μm Ti-14.8V alloy and 100 and 500 μm Ti-9.4Mn alloy. Ti-9.4Mn is a more stable alloy with a MoE value of 13, whereas Ti-14.8V has a MoE value of 9. Hollomon constants were calculated according to equations 1, 7, 9, and 10 as detailed in chapter one.

Ti-9.4Mn Alloy

Log true stress versus true strain plots were generated for both grain sizes for determination of the strain hardening exponent, n for 500 and 100 μm grain sized Ti-9.4Mn alloy [7]. As can be observed in figure 58, for the 500 μm grain size, the plot increases linearly and then plateaus to a nearly horizontal line. The end of this line was used to determine the strain hardening value. As for the 100 μm grain size, which can be viewed in figure 59, its the log true stress versus log true strain plot also displays the similar pattern of increasing linearly and then plateaus to a nearly horizontal line.

A decreasing trend in the strain hardening exponent n values can be observed for Ti-9.4Mn, for 500 μm n is 0.022 and is a smaller value of 0.017 for 100 μm (see Table 12). Additionally, a similar pattern can also be observed for the strain rate sensitivity, where m is 0.001842 for 500 μm grain size and is lower at a value of 0.000553 for the 100 μm grain size. Accordingly, the observed tensile deformation behavior for both grain sizes was slip. This decreasing trend in the Hollomon constant parameters, both m and n values, with respect to the decrease in grain size, therefore affirms that the Hollomon constants depend on the grain size for the Ti-9.4Mn alloy.

Table 12 – Determined Hollomon Constants for Ti-9.4Mn and Ti-14.8V

Alloy	Grain Size (μm)	K (MPa)	Strain Rate (1/s)	m	n	Creep Strain%
Ti-9.4Mn	500	1029.5	1.6×10^{-5}	.001842	0.022	.07
Ti-9.4Mn	100	1027.6	1.6×10^{-5}	.000553	0.017	.042
Ti-14.8V	350	774	3.128×10^{-5}	.002453	0.039	.1
Ti-14.8V	35	899.5	3.128×10^{-5}	.000490	0.014	.04

Ti-14.8V Alloy

Log true stress-log true strain plots were generated for 350 and 35 μm grain sizes, which can be viewed in figures 62 and 63 respectively. It can be seen from closely examining table 12, that there is also a decrease in both the strain hardening exponent n and strain rate sensitivity m values with the decrease in grain size for the Ti-14.8V alloy. The 350 μm grain size has an n value of 0.039, whereas for 35 μm its n value is smaller at 0.014. Although the m values are significantly less in magnitude, it is apparent that they, the m values, decrease with respect to the decrease in grain size, i.e., m is 0.002453 for the 350 μm grain size and has a value of 0.000490 for the 35 μm grain size. It is therefore clear that there is also a similar relationship between the grain size and the Hollomon constant parameters for the Ti-14.8V alloy, as there is also a relationship with the various grain sizes for the creep parameters.

Comparing the Hollomon constant parameter values (see table 12), it can be seen that there is a decreasing trend in both the m and n values for both alloys Ti-9.4Mn and Ti-14.8V with the decrease in grain size. In addition, it can also be observed that this decreasing trend is also the same for the alloy phase stability; i.e., the magnitude of the Hollomon constant parameters decreases with alloy phase stability.

Hollomon Constants
Comparison with Ti-6Al, Ti-6242 Alloys

Comparing the average Hollomon constant parameter values determined in this study for beta titanium alloys Ti-9.4Mn and Ti-14.8V (Table 12), with the values determined for Ti-6Wt%Al (Ti-6Al) and Ti-6Al—2Sn-4Zr-2Mo (Ti-6242) (alpha phase alloys, see Table 13) by Neeraj et. al., it can be observed by direct comparison of tables 12 and 13 there is a significant difference in the magnitude for the strain rate sensitivity m. The average m value for Ti-6242 and Ti-6Al are 0.01 and 0.0185 respectively, however, for Ti-9.4Mn, its m values are 0.001842 (500 μm) and 0.000553 (100 μm); and for Ti-14.8V its m values are 0.002453 (350 μm) and 0.000490 (35 μm) respectively. Both sets of values for both alloys (Ti-14.8V and Ti-9.4Mn) are significantly less than the average values for the alloys investigated by Neeraj.

Table 13 – Average Hollomon Parameters for Ti-6Al and Ti-6242 at Room Temperature [22]

Alloy	K (MPa)	n	m
Ti-6Al	1143	0.04	0.0185
Ti-6242	1430	0.05	0.01

Neeraj observed a significant amount of dislocation arrays (screw dislocation) and planar slip were the observed deformation behavior for the near alpha phase alloys. Whereas in the beta phase titanium alloys investigated in this study and by Ankem et. al., the dominant observed deformation mechanisms were either only planar slip in a more stable β phase alloy (Ti-9.4Mn) and or slip accompanied by SIP in the form of twinning consisting of ω phase deformation products in a lesser stable β phase alloy (Ti-14.8V).

Accordingly, the presence of the observed deformation products decreased with respect to the decrease in grain size and phase stability, just as the magnitude of the Hollomon parameter values decreases with the grain size for the different beta phase alloys.

CHAPTER 6

CONCLUSIONS

1. Tensile deformation properties were as expected, the yield strength decreased with the increase in testing temperature; which is indicative of flow stress behavior at elevated temperatures.

2. The amount of creep strain was found to increase with the increase in test temperature at 95% yield stress; the net creep strain increased from 0.13% at 273K to 0.17% at 458K.

3. The creep deformation mechanisms observed at room temperature are also true for low temperature creep deformation behavior in the range of 273-458K, with slip and twinning as the dominant deformation mechanisms for a 350 μm grain size Ti-14.8V alloy. The dominant deformation mechanisms observed for this grain sized alloy in the studied temperature regime were slip accompanied by dislocations and stress induced plates (SIP) in the form of twinning. The twins were identified as the type of {332}<113>. The extent, the magnitude of the creep deformation behavior increased with the increase in strain and test temperature.

4. Activation energies were determined for this alloy in the test temperature range of 273 – 458 K for establishment of corresponding values with creep deformation mechanisms in this temperature regime for a 350 μm grain sized beta phase Ti-14.8V alloy. The calculated values based on the Arrhenius relationship equation for power law creep deformation behavior were found to increase from 36.6 kJ/mol to 112.42 kJ/mol with the increase in test temperature. Correspondingly, it was found that the activation energy values increased with the increase in creep strain. The determined activation energies for the temperature range of 273-458K for

a 350 μm metastable beta phase Ti-14.8V alloy were found to vary with the amount of creep strain; this is consistent with the supposition that the creep deformation mechanism is initially slip and changes to twinning behavior. The determined activation energy value of 95,287 J/mol is within the range of activation energy for oxygen diffusion, therefore indicative that oxygen solutes are responsible for the time dependent twinning at higher strains as observed by Ankem et. al. for deformation behavior of a 350 μm Ti-14.8V alloy at ambient temperature.

5. Hollomon constant parameters can be used as a predictive measure for creep flow stress deformation behavior. The flow stress behavior for 35 and 350 μm grain size metastable Ti-14.8V and 100 and 500 μm grain size Ti-9.4Mn alloys were examined in which Hollomon Constant Parameters were determined for ambient temperature creep deformation behavior. The determined constant parameters for both grain sizes in both alloys obeyed the creep power law behavior. It was established that both the strain hardening exponent n, and the strain rate sensitivity m, increased with the increase in grain size for both alloys; however, the values decreased with the increase in alloy phase stability. Such a decrease in the parameter values is indicative that the more stable the alloy, the smaller the amount of creep deformation. Therefore, the alloying content affects the amount of exhibited creep strain. Accordingly, the increase in Hollomon Constant Parameter values with the increase in grain size corresponds to the increase in exhibited creep strain for larger grain sizes.

CHAPTER 7

FUTURE RECOMMENDATIONS

The research conveyed in this dissertation has exposed a broad realm of areas in which future studies can be pursued. Activation energies were effectively determined for large grained 350 μm metastable, low stability beta phase Ti-14.8V alloy and resulting dominant deformation low temperature creep deformation mechanisms were determined by optical, SEM, and TEM imaging to be slip and twinning. Determined activation energy values in the low temperature range of 298 – 458 K increased from 36.6 kJ/mol to 112.2 kJ/mol with the increase in creep strain from 0.13% to 0.17%, indicating that both slip and twinning mechanisms are responsible for creep deformation behavior. Low temperature creep studies in the range of 298 – 458 K could be conducted on small in the range of 5 – 30 μm, intermediate 35 – 100 μm, and large grain sizes, i.e., 200, and 500 μm to examine the effect of grain size on low temperature creep behavior, as well as establish the dominant deformation mechanisms and respective activation energy values for intermediate and small grain sizes in this temperature regime.

Lower and higher stability Ti-V alloys can be explored for low temperature creep deformation behavior of 350 μm grain sizes and determination of respective activation energies to ascertain dominant deformation mechanisms. Additionally, low temperature creep studies could be performed on other beta phase titanium alloy systems, i.e., Ti-Mn, Ti-Mo of

different phase stabilities and determination of activation energies responsible for dominant deformation mechanisms.

Another study could also be conducted to determine the exact nature of the resulting linear straight curve for the resulting activation energies determined for deformation in this study.

APPENDIX

ω PHASE

Since its initial discovery in 1954 by Frost et. al., from their observations of diffuse ω phase streaking in x-ray diffraction (XRD) photographs, it has been established that the ω phase is a HCP metastable decomposition product of BCC β-phase titanium alloys [1,51-54]. The intensity of the ω phase diffuse streaking in diffraction patterns has been observed to relate to the stability of an alloy, i.e. the amount of stabilizing elements added to the alloy [1, 51-54]. The intensity of the diffuse ω phase streaking increases as the solute content decreases (amount of alloying elements). Furthermore, as the alloy phase stability (as the MoE value) decreases the ω phase can be seen as clear distinct spots (this has been observed in transmission electron microscopy (TEM) diffraction patterns for non-deformed Ti-14.8V investigated in this study). Frost's initial discovery perpetuated further studies by J.M. Silcock and Bagariatskii to establish the exact crystallographic structure of the ω phase and its orientation of the ω phase with respect to the parent β phase [55]. 1959 Bagariatskii and Nosova confirmed Silcock's findings that the ω phase structure is a hexagonal with 3 atoms in the unit cell, with the ω phase crystal structure related to the β phase as the following $a_{hex} = \sqrt{2}a_{cub}$, $c_{hex} = \sqrt{3/4}a_{cub}$, where c/a ≅ 0.612 [52]. There has been some slight differences in the value for the c/a ratio, some scientists' findings varied from c/a = 0.612 to c/a = 0.613 [51-54]. Additionally, Bagariatskii and Nosova determined the ω phase atom positions to be the following: (0,0,0), ± (1/3, 2/3, z) where z = 0.48 ± 0.01 [52]. Bagariatskii stated that the variation in the z value is based upon the different structure the ω phase can possess, i.e., trigonal or

hexagonal (focus of this paper will be devoted to the "ideal" ω phase hexagonal structure) [52]. Figures A1 a and b are schematic diagrams proposed by Bagariatskii and Nosova on the crystallographic relationship between the parent BCC β phase and the decomposition HCP ω phase structure, and the resulting HCP ω phase crystal structure consisting of 3 atoms per until cell [36]. From observation of figures 14a and b it can be rationalized how diffuse ω phase streaking and discrete ω phase spots can be seen in resulting diffraction pattern images.

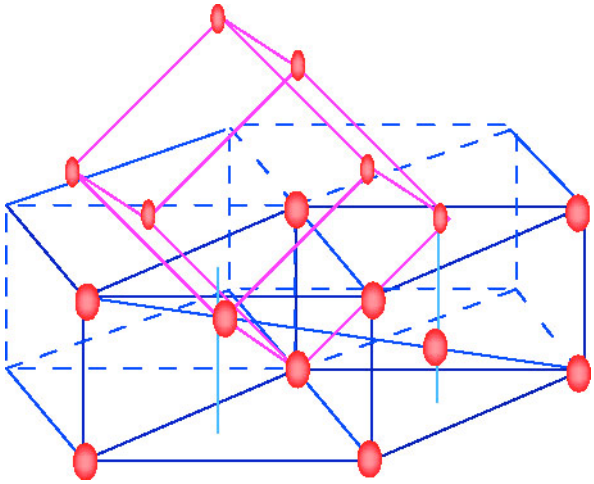

Figure A1a – Relationship between the β phase BCC and the ω phase HCP [52].

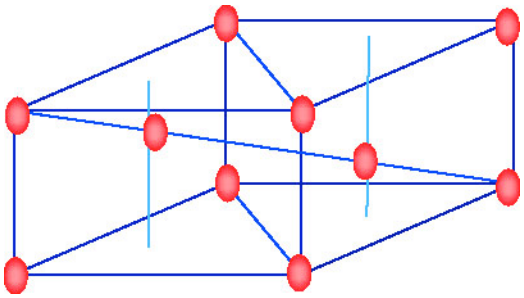

Figure A1b – Resulting 3 atom per unit cell ω phase HCP unit cell [52].

Based on the diligent initial work of Frost, Silcock, Bagariatskii, and Nosova from XRD photographs, as well as, the many confirmed selected area

diffraction (SAD) transmission electron microscopy (TEM) patterns obtained by several other scientists, there are several established orientation relationships between the ω phase HCP structure and the parent β-phase BCC structure. Some of these established orientation relationships are the following [1, 51-54]:

1) $(0001)_{\omega} \| (111)_{\beta}$

2) $(11\bar{2}0)_{\omega} \| (1\bar{1}0)_{\beta}$

3) $(11\bar{2}0)_{\omega} \| (110)_{\beta}$

4) $(0001)_{\omega} \| (001)_{\beta}$

5) $(1\bar{2}10)_{\omega} \| (110)_{\beta}$

6) $(2\bar{1}\,\bar{1}0)_{\omega} \| (1\bar{1}0)_{\beta}$

Therefore it is evident, based on the above listed relationships, that there is an existence of four variants of the ω phase with respect to the β phase BCC parent lattice.

ω Phase Formation

The mechanism for the formation of athermal ω phase resulting quenching has been the subject of many discussions, as well as speculation for several decades. The β phase to athermal ω phase transformation in titanium alloys occurs rather quickly and cannot be suppressed by rapid quenching [1]. Therefore, it is widely believed that the athermal ω phase transformation is a diffusionless martensitic transformation rather than a diffusion controlled one [1]. It has been concluded by several scientists that athermal ω phase forms as a result of very small atomic displacements and cannot be suppressed during quenching in the composition range where it can form (as discussed previously

see figures a, d and e for composition ranges of α, β, β′ and ω phases) [11,30,36,40,41,65].

W.G. Burgers first proposed a transformation mechanism for the BCC to HCP from direct observations of orientations of parent and deformed material in large grained zirconium (which has the same crystal structure as Ti, see figures 18a-c for BCC to HCP transformation relationship) [21,25]. The exact mechanism of this transformation for titanium may not necessarily follow the same transformation as outlined in figures A2 a-c, however, it is evident that the ω phase transformation can occur as a result of a diffusionless process. In order for this transformation to occur, there must be a shear on the (110) plane in the <111> direction of the BCC structure [21,25,54]. Further expansion and contraction of the unit cell edges and displacement of the center atom will result in the HCP structure. This transformation is possible because {110} is an established slip plane for BCC materials; in addition, slip has been observed in β-Ti alloys on the (110) plane in the <111> direction, i.e., (110)<111> [21,25,37,41,65]. During this allotropic transformation, as a result of the shearing in the <111> direction on the (110) plane among the atoms, a stacking fault can possibly occur.

Elaborating on Burgers' mechanism, the ω phase can form within a BCC lattice by applying shears of equal and opposite in the $<111>_{\beta}$ direction on the $(110)_{\beta}$ planes at distances equivalent to 1/6 of the separation of the (111) planes [35,36]. A "linear fault model" proposed by Bagariatskii et. al. is displayed in figure A3 for the ω phase transformation mechanism, the arrows indicate the involved plane of atoms (A and B) and required shear directions [36]. The

important feature in this model is the coherent β/ω interface at the $(110)_\beta$ boundary plane. Proposing that z is the separation distance of the $(111)_\beta$ planes (separation distance = $a\sqrt{3/2}$, where a is the BCC lattice parameter), displacement of A and B atoms by an amount of 1/6z would result in the formation of the "ideal" HCP ω phase structure [36]. Transformation of this type (β to ω phase) on the (110) planes of the β phase could lead to stacking faults in addition to the previous mentioned transformation. This is feasible because slip has been observed on the {110} planes in many BCC metals and is an established slip plane for BCC materials [25]. Furthermore, formation of the ω phase clearly suggests that applied stress would result in slip deformation mechanisms/products, and twins in the <111> direction consisting of ω phase particles. It is evident, based on this model that the presence of such stacking faults would enable the ω phase to dissolve and reform.

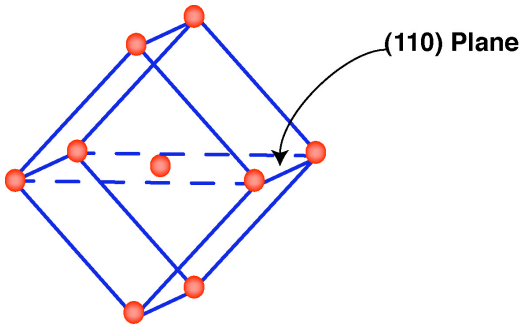

Figure A2a - Diffusionless transformation of β phase into ω phase, BCC unit cell of β phase [21].

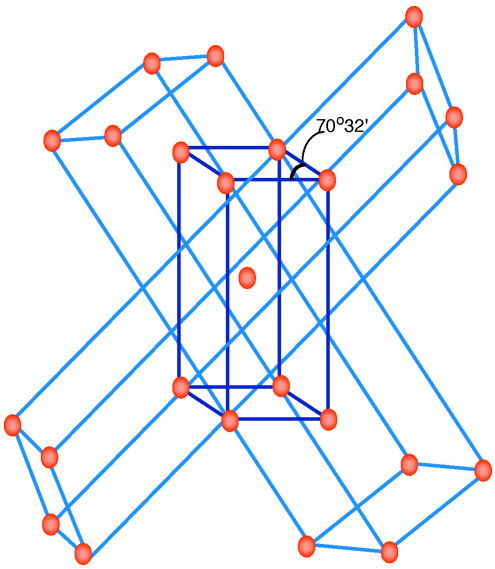

Figure A2b – An array of cells shown in (a) with potential HCP cell outlined [21].

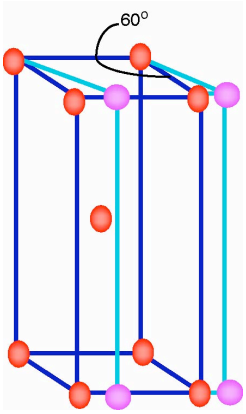

Figure A2c – Resultant shear of cell in (b) into ω HCP titanium cell [21].

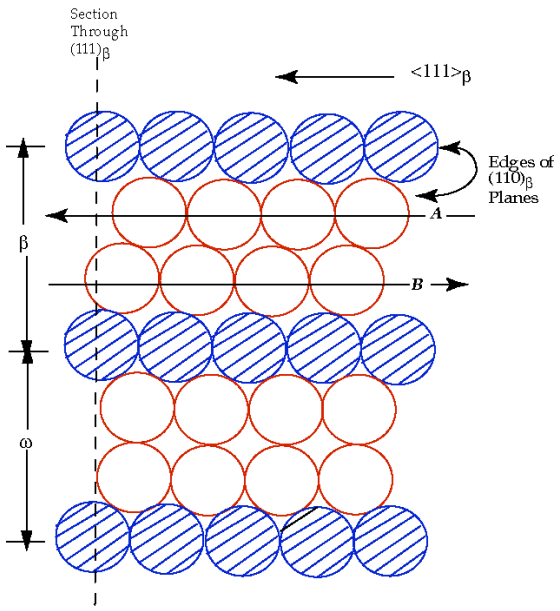

Figure A3 – Linear Fault Model for ω Phase Transformation [21]

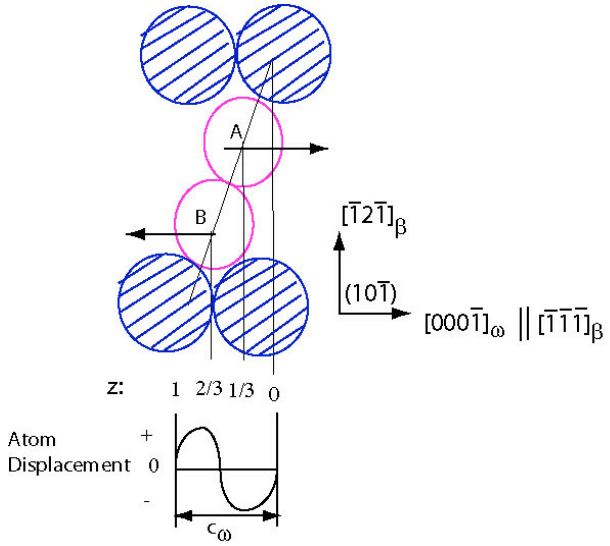

Figure A4a – Schematic of linear dynamic β to ω phase transformation [17].

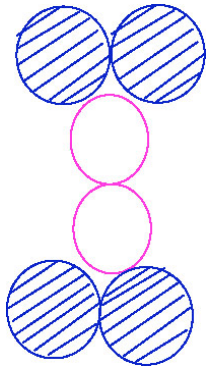

Figure A3b – Resulting ω phase unit cell [40]

ω Phase Formation Resulting From Deformation Mechanisms

In addition to forming from shearing along the {110} planes, the ω phase can also form as a result of slip on the {112} planes [26,41]. Hatt and Roberts demonstrated that the ω phase could form from the β phase by "gliding" (i.e. by slip) on the $\{112\}_\beta$ planes where the glide (referred to slip hereon) component is 0, +g, -g, on alternating planes [23]. "g" is the slip component, which slips on the $\{112\}_b$ plane by $\frac{1}{6}\sqrt{\frac{3}{2}}a_\beta$ in the <111> direction [41]. This motion suggests the reciprocal lattice diffuse streaking effects observed in diffraction patterns, which are the result of stacking faults due to the transformation mechanism as suggested by Hatt and Roberts [41].

Hatt and Roberts' ω phase formation mechanism should be seriously considered and is one that is quite feasible. Considering their model, the stacking sequence for the $\{112\}_\beta$ planes of a BCC structure is: 1, 2, 3, 4, 5, 6, 1, 2, 3, 4,… [41]. The ω phase can form by slipping on the $\{112\}_\beta$ planes in the <111> direction according to table b.

Hatt and Roberts proposed that "faulting" (stacking faults) can occur between generated ω phase "disks," if there is simultaneous nucleation of ω phase on dissimilar $\{112\}_\beta$ planes in the $[111]_\beta$ direction, as a result of slipping during the β to ω phase transformation [41]. It should be noted that twinning of the (112)<111> type has been observed in many BCC lattice materials, and in particular as a deformation product in β phase titanium alloys [1,37,38,47-49,54,55,60,63,66,67].

Another general explanation (which has been described as an equivalent dynamic linear fault crystallographic model) for the β to athermal ω phase formation mechanism is that the ω phase can form by coordinated shifts of the $\{111\}_\beta$ planes of the BCC structure by a 2/3[111] displacement wave [40,41,46,68]. This can be accomplished by collapsing a pair of neighboring {111} planes to the intermediate position leaving the next plane untouched, collapsing the next pair of planes and so forth [40,41,46,68]. As can be viewed in figures 20a and b, based on the supposition that the filled circles (atoms) do not move, while A and B are shifted in opposite directions, a longitudinal wave of a wavelength equal to the separation of the $<111>_\beta$ planes is needed, i.e., a longitudinal phonon with a wave vector of 2/3<111> [40]. This movement of A and B atoms due to the displacement wave of 2/3[111] will result in the HCP ω phase unit cell (figure 20b) [40,41,46,68]. The stacking sequence of the BCC structure on the {111} planes is ABCABCABC…, displacement movements of this form can more than likely create a stacking fault when transforming from the BCC structure to the HCP ω phase structure [40]. In addition, Williams et. al. observed the formation

of linear defects through cooling stage experimental TEM observations of β to ω transformation [68].

Wood proposed two different β phase structures that can result from atomic movements in the <111> direction [32]. Viewing figures 21a and b, it can be seen that only two types of distorted BCC cells are required to form the β - ω phase interface. Based on Woods' proposition, the atoms of the interface will not precisely occupy the β and ω lattice positions, however, they will possess some intermediate positions, as well as, some <100> directions which are common to any pair in the interface [32]. Woods' theory raises a significant question: how exactly does the ω phase alone have an influence on the deformation mode in β titanium alloys? Oka and Taniguchi observed in their studies on a Ti-15.5V alloy that the presence of ω phase cannot exist without the formation of twins as a result of deformation [74]. There has been however, reports of the absence of the ω phase in titanium alloys subjected to deformation by Hanada and Izumi in their examination of Ti-Nb and Ti-Mo alloys, which have stabilities comparable to Ti-V alloys, where the ω phase has been observed after deformation [75]. What is also interesting is that Ankem reported observations of athermal ω phase present in Ti-9.4Mn alloy before and after deformation. Therefore, the amount of deformation ω phase present in an alloy depends on the phase stability and subsequently may control the amount of deformation as a result of its presence.

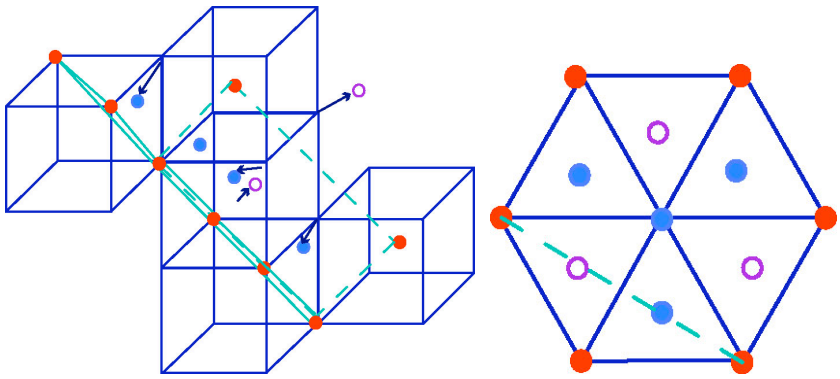

Figure A4a – Interface of β – ω transformation [32]

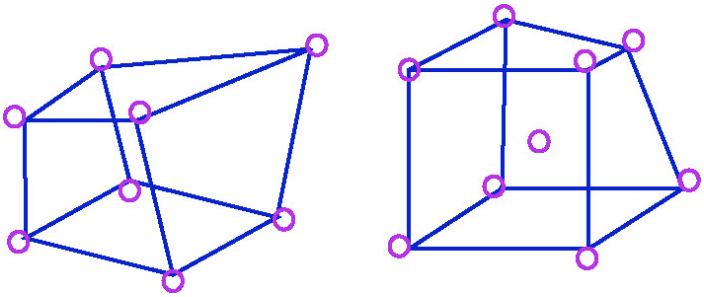

Figure A4b – Two types of b phase unit cell that complete the β – ω interface [32]

β′ Formation

β’ precipitate (is a solute lean BCC precipitate) results when processing temperatures are too high or the alloy is too concentrated to support ω phase precipitation [1]. The occurrence of β′ precipitate can best be viewed in the pseudo-binary phase diagram given in figure 2. As suggested by Williams et. al. β′ phase precipitate is precipitated as a result of chemical differences between the solute and solvent atoms, as opposed to the ω phase where it can be generated by a displacement wave within the crystal [76]. The formation of β′ phase has been studied in Ti-Cr and Ti-Mo alloys and has been considered to be a metastable phase; in addition, its formation is not a common occurrence.

REFERENCES

1. Collings, E.W. The Physical Metallurgy of Titanium Alloys. Materials Park: American Society for Metals, 1984.
2. "Titanium Alloys for Aerospace." *Advanced Materials & Processes* 155(3), March, 1999, 39-41.
3. Eylon, Daniel. 1994. "A Review of Beta Titanium Alloys." Les Alliages de Titane Beta (Beta Titanium Alloys). Cedex France, 75-81.
4. Boyer, R.R. "Applications of Beta Titanium Alloys in Airframes." Beta Titanium Alloys in the 1990's. Minerals Park: The Minerals, Metals and Materials Society, 1993.
5. Bania, Paul J. "Beta Titanium Alloys and Their Role in the Titanium Industry." in Beta Titanium Alloys in the 1990's. Minerals Park: The Minerals, Metals and Materials Society, 1993.
6. Thomas, Roger. "Titanium Market Developments: The Implications for Research and Development," in Titanium Alloys At Elevated Temperature: Structural Development and Service Behaviour. Cambridge: The University Press, 2001.
7. Doraiswamy, D. and S. Ankem. "Effect of Grain Size and Stability on Ambient Temperature Tensile and Creep Deformation in Metastable Beta Titanium Alloys." *Acta Materialia* 51(2003) 1607-1619.
8. Ramesh, Anand and S. Ankem. "The Effect of Grain Size on the Ambient Temperature Creep Deformation Behavior of a Beta Ti-14.8V Alloy." *Metallurgical and Materials Transactions* 33A(2002) 1137.
9. Neuberger, B.W. and S. Ankem. "The Role of interfaces on Mechanical Behavior of Titanium Alloys." in Science and Technology of Interfaces. Materials Park: TMS, 2002, pp.113-129.
10. Ramesh, A. and S. Ankem. "Stress Induced Products in a Ti-14.8V Alloy Deformed in Tension." *Metallurgical and Materials Transactions* 30A(1999) 2249-2251.
11. Hanada, S., Yoshio, T. and O. Izumi. "Deformation and fracture of metastable beta titanium alloys (Ti-15Mo-5Zr and Ti-15Mo-5Zr-3Al)." *Transactions of the Japanese Institute of Metals* 23(2) 85-94 (1982).
12. Hanada, S. Yoshio, T. and O. Izumi. "Effect of Plastic Deformation Modes on Tensile Properties of Beta Titanium Alloys." *Transactions of the Japan Institute of Metals* 27(7) 496-503 (1986).
13. Hanada, S. and O. Izumi. "Deformation behavior of retained beta phase in Beta eutectoid Ti-Cr alloys. "*Journal of Materials Science* 21(1986) 4131-4139.
14. Hanada, S. and O. Izumi. "Correlation of Tensile Properties, Deformation Modes, and Phase Stability in Commercial β-Phase Titanium Alloys." *Metallurgical Transactions* 18A(1987) 265-271.
15. Oka, M. and Taniguchi, Y. "{332} Deformation Twins in a Ti-15.5PctV Alloy." *Metallurgical Transactions A* 10(1979) 651-653.
16. Paris, H.G., B.G. LeFevre and E.A. Starke, Jr. "Deformation Behavior in Quenched and Aged Beta Ti-V Alloys." *Metallurgical Transactions* 7A(1976) 273-278.
17. Williams, J.C., de Fontaine, D. and N.E. Paton. "The ω Phase as an Example Of Unusual Shear Transformation." *Metallurgical Transactions* 4(1973) 2701-

2708.
18. Hida, Moritaka, Eiichi Sukedai, Yukio Yokohari and Akihiro Nagakawa. "Thermal Instability and Mechanical Properties of Beta Titanium-Molybdenum Alloys." in Titanium '80 Conference Proceedings, Tokyo Japan, 1980. p. 1327-1334.
19. Ling, Fu Wen, E.A. Starke, Jr. & B.G. LeFevre. "Deformation Behavior and Texture Development in Beta Ti-V Alloys." *Metallurgical Transactions* 5(1974) 179-187.
20. Sully, A.H. Metallic Creep. New York: Interscience Publishers, Inc., 1949.
21. Nabbaro, F.R.N. and deVilliers, H.L. The Physics of Creep. New York: Taylor and Francis, 1995.
22. Neeraj, T., D.-H. Hou, Daehn, G.S. and M.J. Mills. "Phenomenological and Microstructural Analysis of Room Temperature Creep in Titanium Alloys." *Acta Materialia* 48(2000) 1225-1238.
23. Thompson, A.W. and B.C. Odegard. "The Influence of Microstructure on Low Temperature Creep of Ti-5Al-2.5Sn." *Metallurgical Transactions* 4(1973) 899-908.
24. Suzuki, Hirowo G. and Hideki Fujii. "Deformation Characteristics of Ti15V-3Cr-3Sn-3Al at Elevated Temperature." *ISIJ International* 31(1991) 814-819.
25. Ponsonnet, L., C. Quesne, R. Penelle. "Microstructure and creep deformation of a near beta titanium alloy 'β-CEZ'." *Materials Science and Engineering* A262(1999) 50-63.
26. Cuddy, L.J. "Internal Stresses and Structures Developed During Creep." *Metallurgical Transactions* 1(1970) 395-401.
27. Hollomon, J.H. and J.D. Lubahn. "The Flow of Metals at Elevated Temperatures Part I." General Electric Review (1947) 28-32.
28. Lubahn, J.D. Proc. ASTM 52A(1952) 905.
29. Lubhan, J.D. and R.P. Felgar. Plasticity and Creep of Metals. New York: John Wiley and Sons, Inc., 1961.
30. Boehlert, C.J. "Microsturcture, creep, and tensile behavior of a Ti-12Al-38Nb (at%) beta + orthorhombic alloy." *Materials Science and Engineering* A267 (1999) 82-98.
31. Clauer, A.H. and B.A. Wilcox. "Creep of β Titanium Alloys." in International Conference on Titanium, Volume 4. New York: Plenum Press, 1973.
32. Maeda, Takashi, Hidehiro Onodera, Sirou Watakabe, Hideo Nakajima, Hideki Fujii, and Kazuhide Takahashi. "Interdiffusion in Binary Beta Titanium Alloys." in International Symposium on Metallurgy and Technology of Practical Titanium Alloys. Warrendale: The Minerals, Metals and Materials Society, 1993.
33. Peart, R.F. and D.H. Tomlin. "Diffusion of Solute Elements in Beta Titanium." *Acta Metallurgica* 11-(1962) 123-134.
34. Dyment, F. and C.M. Libanati. "Self-Diffusion of Ti, Zr, and Hf in their HCP Phases and Diffusion of Nb in HCP Zr." *Journal of Materials Science* 3(1968) 349-359.
35. Schuh, C. and D.C. Dunand. "An overview of power-law creep in polycrystalline β titanium." Scripta Materialia 45(2001) 1415-1421.

36. Liu, Z. and G. Welsch. "Literature Survey on Diffusivities of Oxygen, Aluminum, and Vanadium in Alpha Titanium, Beta Titanium, and in Rutile." *Metallurgical Transactions A* 19(1988) 1121-1125.
37. Ramesh, Anand. Effect of Stability and Grain Size on Ambient Temperature Tensile and Creep Behavior of Beta Titanium Alloys. Masters Thesis. University of Maryland-College Park, 1998.
38. Doraiswamy, Durgalakshmi. 2001. The Effect of Grain Size and Stability on Ambient Temperature Tensile and Creep Deformation Behavior of Metastable Beta Titanium Alloys. Masters Thesis. University of Maryland-College Park.
39. Froes, F.H. and H.B. Bomberger. "The Beta Titanium Alloys." *Journal of Metals* 37(1985) 28-37.
40. Donachie, Matthew, J. Titanium: A Technical Guide. Materials Park: ASM International, 2000.
41. Bowen, A.W. "Omega Phase Formation in Metastable β-titanium Alloys," in Beta Titanium Alloys in the 1980's. New York: TMs, 1984.
42. Lutjering, Gerd and James C. Williams. Titanium. New York: Springer Verlag, 2003.
43. Hickman, B.S. (1969) "The Formation of Omega Phase in Titanium and Zirconium Alloys: A Review, " *Journal of Materials Science* 4 (1969) 554-563.
44. Grewal, G. and S. Ankem. "Solubility of Vanadium in α and β Titanium." *Metallurgical Transactions* 20A (1989) 334-337.
45. Jepson, K.S., Brown, A.R.G. and Gray, J.A. "The Effect of Cooling Rate on the Beta Transformation in Titanium-Niobium and Titanium-Aluminum Alloys." in The Science Technology and Application of Titanium (Proceedings of the First International Conference on Titanium). London: Pergamon Press, 1970, p. 677-90.
46. Williams, J.C., "Kinetics and Phase Transformations: A Critical Review." in The Science Technology and Application of Titanium (Proceedings of the First International Conference on Titanium). London: Pergamon Press, 1970, p.1433-94.
47. Suzuki, T. and Wuttig, M. "Analogy Between Spinodal Decomposition and Martensitic Transformation." *Acta Metallurgica* 23 (1975) 1069-76.
48. Oka, M. and Taniguchi, Y. "Crystallography of Stress-Induced Products in Metastable Beta Ti-Mo Alloys." in Proceedings of the Fourth International Conference on Titanium, Kyoto, Japan. The Metallurgical Society of AIME, 1980 p. 709-715.
49. Duerig, T.W., R.M. Middleton, G.T. Terlinde and J.C. Williams. "Stress Assisted Transformation in Ti-10V-2F3-3Al." in Proceedings of the Fourth International Conference on Titanium, Kyoto, Japan. The Metallurgical Society of AIME, 1980 p. 1503-1512.
50. Oka, M. and Taniguchi, Y. "{332} Deformation Twins in a Ti-15.5%V Alloy." *Metallurgical Transactions A* 10(1979) 651-653.
51. Bagariatskii, Iu. A. and G.I. Nosova. "Exact Determination of the Atomic Coordinates in the Metastable w-Phase of Ti-Cr Alloys." *Soviet Physics Crystallography* 3(1959) 15-26.
52. Bagariatskii, Iu.A., Nosova, G.I. and Tanuova, T.V. "Factors in the Formation of Metastable Phases in Titanium-Base Alloys." *Soviet Physics Doklady* 3(1959) 1014-1018.

53. Frost, P.D., W.M. Parris, L.L. Hirsch, J.R. Doig and C.M. Schwarz. *Transactions of the American Society of Metals* 46 (1954) 231-56.
54. Silcock, J.M. "An X-ray Examination of the ω Phase in TiV, TiMo and TiCr Alloys." *Acta Metallurgica* 6(1958) 481.
55. Silcock, J.M.D., M.H. Davies and H. K. Hardy. "The structure of the ω precipitate in titanium-16% vanadium alloy." *Nature* 175(1955) 731.
56. Bursik, J. and G.C. Weatherly. "Transformation of the β-(Ti-V) Phase in Ti-V-C Alloys." *Scripta Metallurgica* 40(1999) 1381-1386.
57. Ankem, S. and S.R. Seagle. "Heat Treatment of Metastable Beta Titanium Alloys." Beta Titanium Alloys in the 1980's. New York: American Institute of Mining, Metallurgical, and Petroleum Engineers, Inc., 1984, 107-126.
58. Blackburn, M.J. and J.C. Williams. "Phase Transformations in Ti-Mo and Ti-V Alloys." *Transactions of the Metallurgical Society of AIME* 242 (1968) 2461-2469.
60. Paton, N.E., J.C. Williams. "The Influence of oxygen content on the athermal beta-omega transformation." *Scripta Metallurgica* 7(1973) 647-650.
61. Greene, Charles A. Fundamental Studies on Ambient Temperature Creep Deformation Behavior of Alpha and Alpha-Beta Titanium Alloys. Ph.D. Dissertation, University of Maryland-College Park, 1994.
62. Attwood, D.G. and P.M. Hazzeldine. "A Fiducial Grid for High-Resolution Metallography." *Metallography* 9 (1976) 483-501.
63. Karimi, A. "Plastic Flow Study Using the Microgrid Technique." *Materials Science and Engineering* 63(1984) 267-276.
64. Elliott, Stephen M. "Basic Positive Photolithography." *Karl Suss Seminar Series* Publication No 106, Waterbury Center: Karl Suss America, Inc, 1987.
65. SPIE Handbook of Microlithography Section 2.7 Resists-PMMA.
66. MicroChem Specification Sheet-Nano PMMA and Copolymer
67. Applied Test Systems Series 3210 Split Tube Furnace and Accessories Instruction Manual, 2002.
68. Spurling, R.A. "A Technique for Preparing Thin Foils of Ti and Ti Alloys for Transmission Electron Microscopy." *Metallurgical Transactions A* 6A(1975) 1660-1661.
69. Williams, J.C., de Fontaine, D. and N.E. Paton. "The ω Phase as an Example of Unusual Shear Transformation." *Metallurgical Transactions* 4(1973) 2701-2708.
70. Sokiryanskiy, L.F., Ignatov, D.V. and A. Ya. Shinyaev. "Influence of Polymorphic Transformation in Oxygen Diffusion in Titanium." *The Physics of Metals and Metallography* 28(1969) 103-108.
71. Rosa, Casimir. "Oxygen Diffusion in Alpha and Beta titanium in the temperature Range of 932 to 1142C." *Metallurgical Transactions A* 1(1970) 2517-2522.
72. Flower, H.M. "Room Temperature Age-Hardening in a Beta Titanium Alloy." *Journal of Materials Science* 19(1984) 2887-2893.
73. de Meester, M. Doner, and H. Conrad. "Deformation Kinetics of the Ti-6Al-4V Alloy at Low Temperatures." Metallurgical Transactions a 6(1975) 65-75.
74. Miller, W.H., R.T. Chen and E.A. Starke, Jr. "Microstructure, Creep, and Deformation in Ti-6Al-2Nb-1Ta-0.8Mo." *Metallurgical Transactions A* 18(1987) 14511468.

75. Claisse, F. and H.P. Koeing. "Thernal and Forced Diffusion of Oxygen in Beta Titanium." *Acta Metallurgica* 4(1956) 650-654.